UNIVERSIDADE FEDERAL DO CEARÁ
CENTRO DE CIÊNCIAS
DEPARTAMENTO DE FÍSICA
PROGRAMA DE PÓS-GRADUAÇÃO EM FÍSICA

JUAN SIMÓN RODRÍGUEZ HERNÁNDEZ

STRUCTURAL-PROPERTY RELATIONSHIPS IN METAL HALIDE LIKE-PEROVSKITES UNDER EXTREME CONDITIONS

FORTALEZA
2023

JUAN SIMÓN RODRÍGUEZ HERNÁNDEZ

STRUCTURAL-PROPERTY RELATIONSHIPS IN METAL HALIDE LIKE-PEROVSKITES UNDER EXTREME CONDITIONS

Tese de Doutorado apresentada ao Programa de Pós-Graduação em Física da Universidade Federal do Ceará, como requisito parcial à obtenção do título de Doutor em Física. Área de concentração: Física da Matéria Condensada.

Orientador: Prof. Dr. Carlos William de Araújo Paschoal.

FORTALEZA

2023

Dados Internacionais de Catalogação na Publicação
Universidade Federal do Ceará
Sistema de Bibliotecas
Gerada automaticamente pelo módulo Catalog, mediante os dados fornecidos pelo(a) autor(a)

R618s Rodríguez Hernández, Juan Simón.
Structural-property relationships in metal halide like-perovskites under extreme conditions / Juan Simón Rodríguez Hernández. – 2023.
117 f. : il. color.

Tese (doutorado) – Universidade Federal do Ceará, Centro de Ciências, Programa de Pós-Graduação em Física , Fortaleza, 2023.
Orientação: Prof. Dr. Carlos William de Araújo Paschoal.

1. Metal halide like-perovskites. 2. Structural phase transition. 3. X-ray diffraction. 4. Raman spectroscopy. 5. Extreme conditions. I. Título.

CDD 530

JUAN SIMÓN RODRÍGUEZ HERNÁNDEZ

STRUCTURAL-PROPERTY RELATIONSHIPS IN METAL HALIDE LIKE-PEROVSKITES UNDER EXTREME CONDITIONS

Tese de Doutorado apresentada ao Programa de Pós-Graduação em Física da Universidade Federal do Ceará, como requisito parcial à obtenção do título de Doutor em Física. Área de concentração: Física da Matéria Condensada.

Aprovada em: 26/04/2023.

BANCA EXAMINADORA

_____
Prof. Dr. Carlos William de Araújo Paschoal (Orientador)
Universidade Federal do Ceará (UFC)

_____
Prof. Dr. Alejandro Pedro Ayala
Universidade Federal do Ceará (UFC)

_____
Prof. Dr. Paulo de Tarso Cavalcante Freire
Universidade Federal do Ceará (UFC)

_____
Prof. Dr. Newton Martins Barbosa Neto
Universidade Federal do Pará (UFPA)

_____
Dr. Wellington Castro Ferreira
Harvard University

ACKNOWLEDGMENTS

I am sincerely grateful to my supervisor, Prof. Dr. Carlos William de Araújo Paschoal, for his invaluable guidance, unwavering support, constant encouragement, and patience, which helped me throughout the entire development of my doctoral projects and thesis.

I would like to thank Prof. Dr. Alejandro Pedro Ayala for his valuable advice and contributions during the development of this work and for allowing me to be a part of his research group.

I would like to extend my thanks to Mayra Padron for all her contributions to the experiments and her support. Thank you very much for always being my right hand. You have been the perfect partner. As we always said, we make the best team, and we will reach everything together. Muchas gracias de todo corazón, mi pecosa.

I would like to express my gratitude to my family for their continued support, even though countries separate us. They always provided me with comfort and strength. Muchas Gracias!

Additionally, I am grateful to my friends Wendell, Felipe, Dieric, Thiago, Pedro, Avelar, Otavio, and Daniel for their generous providing generous advice and for accompanying me during this journey. Muito obrigado!

I would like to extend my sincere thanks to UFC and the Pos-graduação em Física for allowing me to study here. I would also like to thank CNPq for their financial support.

Finally, I would like to express my special gratitude to the lab groups OPEMLab, LabCrEs, Laboratório de Altas Pressões of the UFC, Lab MaDe, and the EMA group for the Laboratório Nacional de Luz Síncroton (LNLS), for providing me with invaluable research experience and contributing to my academic growth.

ABSTRACT

Metal halide perovskites are versatile materials with numerous promising applications in solar cells, semiconductors, electronic devices, and optoelectronic performance. Studying reveals interesting and important physical properties that are strongly related to the pressure/temperature-induced modifications on their crystal lattice and structural phase transitions. For example, the Erythrosiderite-halides complexes, such as $A_2FeCl_5.H_2O$ with A = Cs, Rb, K or NH_4, exhibit at room temperature an orthorhombic structure *Pnma* or *Cmcm*. The $Cs_2FeCl_5.H_2O$ (*Cmcm*) at *Tt* = 156 K undergoes a structural phase transition (SPT) to a monoclinic (*C*2/*c*) structure that could be related to the ferroelastic *mmmF2/m* type. The strains in the sample were analyzed based on Landau theory and using Raman spectroscopy. The results define a new ferroic order in the sample. Other like-perovskites with the general formula ABX_3 can be described by the most common space group $P6_3/mcc$. The hybrids based on dimethylammonium $[(CH_3)_2NH_2]^+$, such as $DMAPbX_3$ with halide ions X = Br or I, undergo a structural phase transition at *Tt* = 250 K via an order-disorder mechanism. At low temperatures, the strong electron-phonon coupling permits self-trapped exciton states, modifying the photoluminescence (PL) profile and increasing new band contributions and an emission change of the PL from orange-red to bright red. A thermochromic effect is also observed in $DMAPbI_3$ after *Tt*. $CsCuCl_3$, with the same $P6_3/mcc$ crystal structure, was studied at low temperatures and high-pressure, and spin-phonon coupling (SPC) was verified with decreasing temperature. A paramagnetic to antiferromagnetic phase transition permits the SPC effect, but an anomalous phenomenon was identified at T^* = 15 K. At high pressure, a structural phase transition to *C*2 was found, and the bulk modulus sample for each phase was calculated, indicating potential applications for the compound. The investigation revealed that the SPT involves the reorganization of the internal $[CuCl_6]^{4-}$ octahedra, with Cl-Cu-Cl bending contributing more than Cl-Cu-Cl stretchings. In this context, the results of the structural-property relations in past metal halide like-perovskites pave the way for developing new and improved devices and technologies.

Keywords: metal halide like-perovskites; structural phase transition; x-ray diffraction; Raman spectroscopy, extreme conditions.

RESUMO

As perovskitas de haleto metálico são materiais versáteis com numerosas aplicações promissoras em células solares, semicondutores, dispositivos eletrônicos e optoeletrônicos. O estudo desses materiais revela propriedades físicas interessantes e importantes que estão fortemente relacionadas às modificações na rede cristalina e transições de fase estruturais induzidas por pressão/temperatura. Por exemplo, os complexos de eritrosiderita-halogeneto, como $A_2FeCl_5.H_2O$ com A = Cs, Rb, K or NH_4, exibem, a temperatura ambiente, uma estrutura ortorrômbica *Pnma* ou *Cmcm*. O $Cs_2FeCl_5.H_2O$ (*Cmcm*) em *Tt* = 156 K sofre uma TFE para uma estrutura monoclínica (*C*2/*c*) que pode estar relacionada ao tipo ferroelástico *mmmF2/m*. As deformações na amostra foram analisadas com base na teoria de Landau e com espectroscopia Raman, ambos resultados definem a nova ordem ferroica na amostra. Outras perovskitas do tipo ABX_3 são descritas pelo grupo espacial $P6_3/mcc$. Amostras híbridas baseadas em dimetilamônio $[(CH_3)_2NH_2]^+$, como $DMAPbX_3$ com íons de haleto X = Br ou I, sofrem uma transição de fase estrutural em *Tt* = 250 K por um mecanismo de ordem-desordem. Em baixas temperaturas, o forte acoplamento elétron-fônons permite estados de éxciton autoprisionados modificando o perfil da fotoluminescência (PL), resultando em um aumento nas contribuições de novas bandas e uma mudança na emissão da PL de laranja-vermelho para vermelho brilhante em $DMAPbI_3$. Um efeito termocromático também é observado em $DMAPbI_3$ após *Tt*. O $CsCuCl_3$, com a mesma estrutura cristalina $P6_3/mcc$, foi estudado em baixas temperaturas e altas pressões. Um acoplamento spin-fônon (ASF) foi verificado com a diminuição da temperatura. Além disso, um fenômeno anômalo foi identificado em *T** = 15 K, e foi interpretado em termos de uma frustração magnética via interação Dzyaloshinskii–Moriya (DM). Sob alta pressão, uma TFE para *C*2 foi encontrada, o módulo de bulk da amostra para cada fase foi calculado, indicando aplicações potenciais em eletrônica flexível para o composto. A investigação revelou que a TFE envolve a reorganização dos octaedros internos $[CuCl_6]^{4-}$, com a flexão Cl-Cu-Cl contribuindo mais do que as distensões Cl-Cu-Cl. Neste contexto, os resultados das relações estrutura-propriedade em perovskitas do tipo haleto metálico abrem caminho para o desenvolvimento de novos dispositivos e tecnologias.

Palavras-chave: perovskitas de haleto metálico, transições de fase estruturais; difração de raios-x, espectroscopia Raman, condições extremas.

FIGURES LIST

TABLES LIST

CONTENTS

1 INTRODUCTION

Materials based on perovskite crystal structures have emerged as promising and efficient low-cost solutions for various optoelectronics, multiferroics, and photonics device applications in recent years (Dong *et al.*, 2023; Lu *et al.*, 2023). The perovskite crystal structure consists of a corner-sharing BX_6 octahedron, with A elements occupying the cuboctahedral cavity in each unit cell (see **Figure 1**). These materials crystallize with the general chemical formula ABX_3, where A and B are cations, and X is the halide anion. Deviations from the ABX_3 stoichiometry can be achieved through total or partial substitution of chemical elements in their proper A, B, or X positions (Jin, 2021). Such substitutions can modify the crystal structure and lead to the development of new properties, facilitating the establishment of structure-property relationships in these compounds. Currently, this topic is of high interest in the research community, as it is driving the development of new and advanced materials for various technological applications (Zhu e Zhu, 2020).

Figure 1 – Standard cubic metal halide perovskite. Shown in display styles evidencing all atoms (left) and the BX_6 octahedral network (right). ($CsPbI_3$ ($Pm\bar{3}m$)- ICSD: 161481).

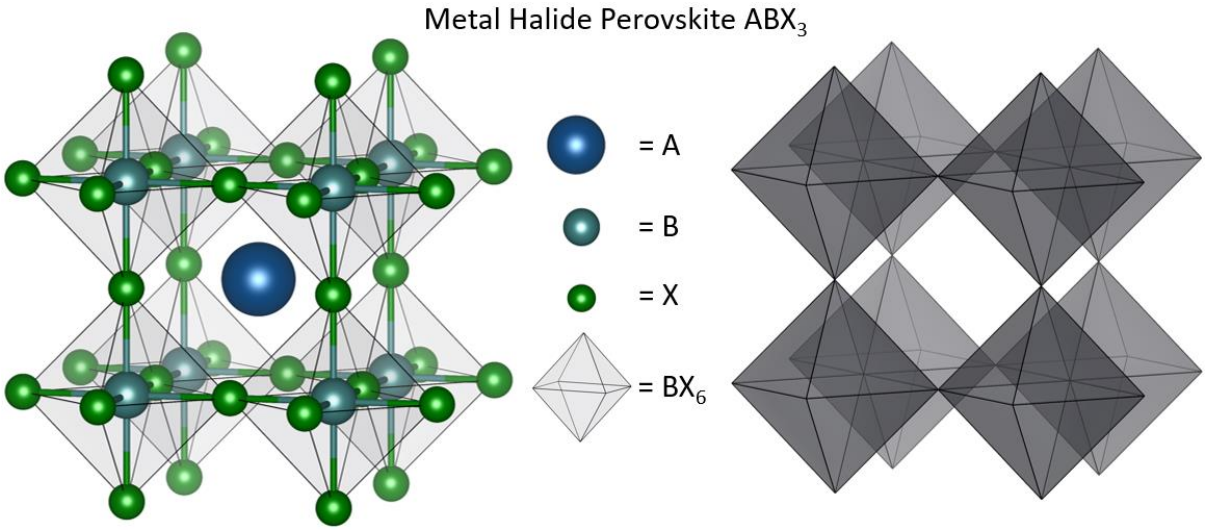

Source: Elaborated by the author.

The origin of the word perovskite dates to Gustav Rose discovery, the calcium titanate ($CaTiO_3$) in 1839, which he named in honor of the Russian mineralogist Count Lev Perovski. Nowadays, perovskite refers to a large group of compounds with a crystal structure resembling calcium titanate (Nam-Gyu Park, Michael Grätzel e Tsutomu Miyasaka, 2016). Perovskite materials are characterized by their archetypal system, with accessible cubic, tetragonal, orthorhombic, trigonal, and monoclinic polymorphs (Akkerman e Manna, 2020;

Alaei *et al.*, 2021), with their structural phase transitions (SPT) as a function of temperature and pressure. Briefly, metal halide perovskites are compounds formed from halide salts (chloride: Cl, bromide: Br, and iodide: I) that crystallize in the ABX_3 structure. These compounds can be formed with both the fully inorganic and hybrid organic-inorganic structures (Xiao, Song e Yan, 2019; Zhou *et al.*, 2019). The modification of the network of corner-sharing BX_6 octahedra defines the metal halide perovskites (MHPs) crystal lattice. Due to lattice distortions, the MHPs usually reduced their symmetry compared to the main form ABX_3, as described in **Figure 2**. While the number of natural perovskite minerals is limited, synthetic compounds can be created across all the periodic table, which derivatives in many complex formulas, and perovskite types such as metallics, metal-free, and oxides and like-perovskites, indicating an adaptable crystal lattice (see **Figure 3**).

Figure 2 – Overview of different halide perovskites. **a)** Standard ABX_3 cubic perovskites. **b)** Anti perovskites, with A being a monovalent metal, X a halide, and Y a chalcogenide. **c)** Common orthorhombic and tetragonal disordered perovskites arise from the tilting of the octahedra. **d)** Vacant BX_3 perovskites, like AlF_3. **e)** Ordered perovskites, where two M (II) metals are replaced by a M (I) and M (III) metal. **f)** Vacancy-ordered perovskites, where a part of the B-site cations is replaced with a M (III) or M (IV) and vacancies.

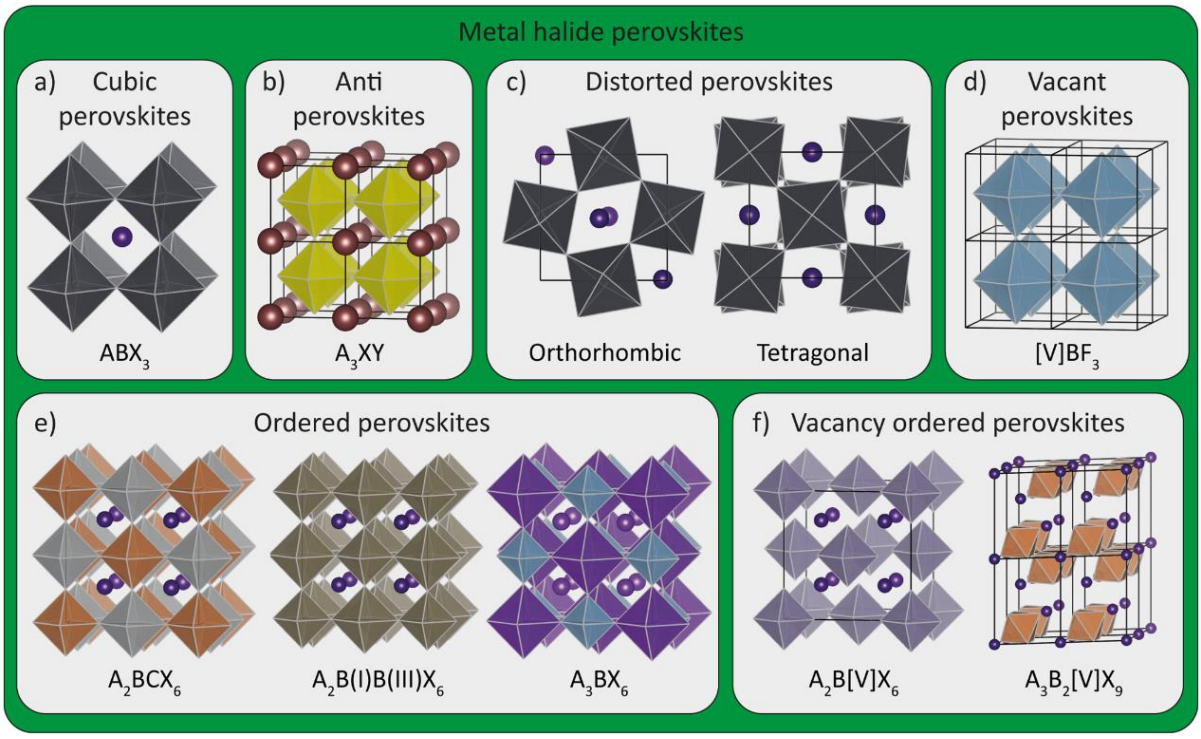

Source: (Akkerman e Manna, 2020) with adaptations.

An important characteristic of perovskite structures is their close packing, which is quantified by the Goldschmidt tolerance factor, t, given by the equation:

$$t = \frac{r_A + r_X}{\sqrt{2}(r_B + r_X)} \quad (1)$$

Equation (1) is a well-known description that has been extensively used to predict the stability of perovskite structures based on the chemical formula ABX_3, and the ionic radii r_A, r_B and r_X of each ion (A, B, X). However, this equation does not always correctly distinguish between perovskites and like-perovskite compounds. To address this issue, a better approximation of the tolerance factor (τ) has been proposed as follows (Bartel *et al.*, 2019):

$$\tau = \frac{r_X}{r_B} - n_A\left(n_A - \frac{r_A/r_B}{\ln(r_A/r_B)}\right) \quad (2)$$

where n_A is the oxidation state of A, and r_A, r_B and r_X are the ionic radius of the A, B and X ions. Perovskite structures are defined by $\tau < 4.18$, as shown in **Figure 4**. Structures with $\tau > 4.18$ are like-perovskites, post-perovskites or non-perovskites, as they have a similar general formula and are stable. However, their distortion modifies the corner-sharing BX_6 octahedra, resulting in different arrangements and dimensions of the connecting octahedra, as shown in **Figure 3**. Understanding the tolerance factor and the distinction between perovskite and perovskite-like structures is crucial for predicting the stability of perovskite materials and separating them.

Figure 3 – Overview of stables metal halides with non-perovskites bases formed by the ABX_3 formula.

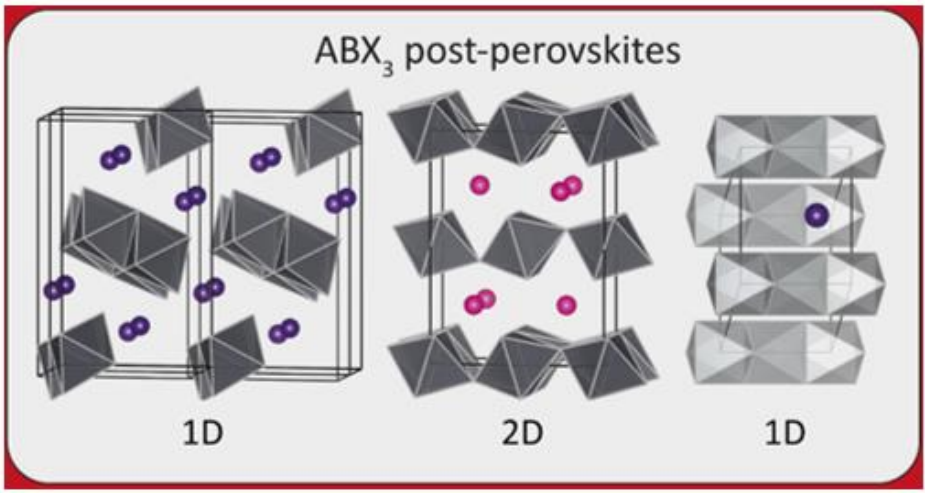

Source: (Akkerman e Manna, 2020) with adaptations.

Figure 4 – **A** Perovskite structure of the standard cubic single perovskite structure ABX_3 ($Pm\bar{3}m$), where a network of corner-sharing BX_6 octahedra surrounds the A cation. **B** The τ factor with achieves a classification with more than 92% accuracy. **C** Map of the elements that occupy the A, B and X sites within the compounds characterized as perovskite or like-perovskites at room conditions. **D** Comparison of perovskites and non-perovskites of Platt-scaled classification probabilities($P(\tau)$ versus t). The $LaAlO_3$ and $NaBeCl_3$ are labeled to highlight the modification of $P(\tau)$ at nearly constant t.

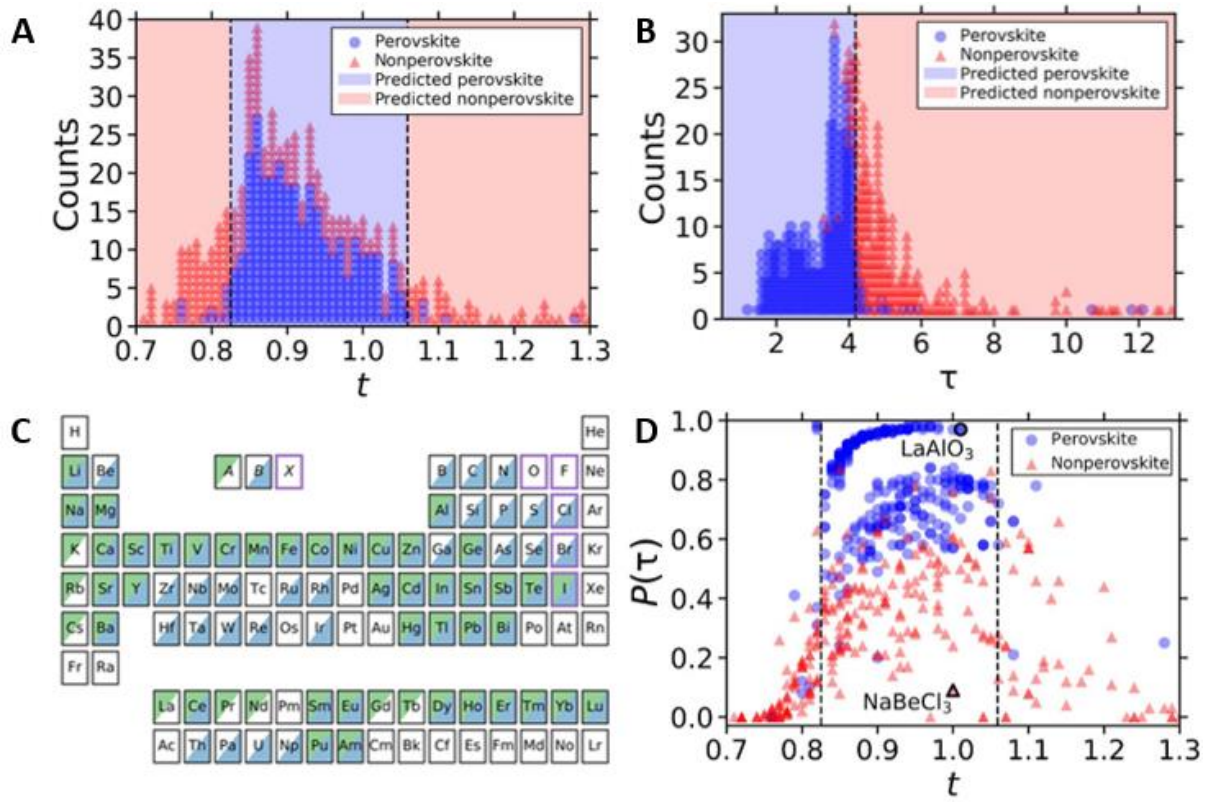

Source: (Bartel *et al.*, 2019) with adaptations.

Notably, metal halide perovskites exhibit significant polymorphism, and diverse structural phase transitions highly dependent on temperature and pressure. These structural phase transitions have been shown to profoundly impact the electronic and optical properties of MHPs (Burger *et al.*, 2021; Octavio de Araujo *et al.*, 2022). Specifically, modifications in lattice parameters, phonon frequencies, and electron-phonon coupling strengths observed during the phase transitions can be harnessed to design new functional materials with applications in optoelectronics, flexible electronics, and smart windows.

For instance, while $CsBI_3$, with B = Pb, Sn adopts a non-perovskite structure and exhibits an insulating phase at room temperature, it is not ideal for optoelectronic device applications (Yao, Zhao e Liu, 2021). However, the relationship between polymorphism and optoelectronic properties could be less drastic in other systems (Duan *et al.*, 2022). One notable example is the tetragonal-to-cubic transition observed in methylammonium [MA= CH_3NH_3]

lead iodide $MAPbI_3$ at 330 K. This transition significantly impacts the charge carrier dynamics, resulting in the formation of self-trapped exciton states. Such dynamic behavior has made understanding several important structure−property relationships challenging and has obstructed a clear path toward commercialization due to inherent phase instability. Therefore, it is essential to deepen our understanding of the underlying mechanism and anion exchange in MHPs to gain a clearer perspective. Understanding and controlling polymorphism and structural phase transitions in perovskites are necessary to ensure the reliable performance of these compounds and to design and engineer new materials with desired properties for specific applications (Kim *et al.*, 2022; Tang *et al.*, 2022).

Metal halide perovskites are systems whereby their structural and compositional modifications impact the physical properties present in the sample (Gao *et al.*, 2019; Yan *et al.*, 2023). Thus, several important aspects regarding the underlying mechanism and anion exchange must be further studied to clarify the perspective of a correlation between crystal structure and physical property. For instance, two mechanisms control the perovskite phase and composition, which are highly related to properties such as octahedral tilting and anion exchange (Shi, Zejiao *et al.*, 2017). Synchrotron-based and conventional X-ray diffraction measurements elucidate the physical aspects of modifying the octahedral displacements related to perovskites and like-perovskites compounds. Differential optical methods reveal the anion exchange processes, and both analyses are developed in situ and separated from characterizing the tunable properties quantitatively. These are the first steps in the characterization of perovskites and like-perovskites. **Figure 5** exhibits the structural diversity of perovskites derived from the potential for the dynamic octahedra tilt with a corner-sharing network of an ABX_3 form (Ahn *et al.*, 2017; Chan *et al.*, 2022; Steele *et al.*, 2020; Tu *et al.*, 2018).

The octahedral tilting is essentially responsible for the structural variation and destabilization of the cubic ABX_3 phase in perovskites. **Figure 5**B illustrates how proper octahedral tilting prevents the collapse of the corner-sharing network while the temperature varies. As previously discussed, when the tolerance factor shifts away, the energy required for bond bending is sufficient to break them, forming like-perovskite or non-perovskite structures, such as side- or face-sharing octahedra (Grancini e Nazeeruddin, 2018). Restructuring the cubic phase into a lower symmetry subgroup is fundamental in halide perovskites and like-perovskite compounds.

Figure 5 – Phase transitions, anion exchange, and the phase-energy landscape in polymorphic ABX_3 perovskites. **A** Archetypal cubic crystal structure (t = 1) and anion exchange concept for ABX_3 perovskites. When t deviates from unity, octahedral tilts are introduced to accommodate a pseudo cubic distorted perovskite structure. **B** Ilustration of reversible phase transitions in polymorphic perovskites, transitioning though pseudo cubic structures via octahedral tilting and into a non-perovskite structure via bond breaking. **C** Overview of reported group-subgroup symmetries of tilted halide perovskites $APbX_3$ (A=MA, FA, Cs; X= Cl, Br, I), and $CsSnX_3$ (X=Cl, Br, I) with comparison to the archetypal $CaTiO_3$ perovskite system. The tilts are identified using Glazer notation and the dashed lines correspond to first-order transitions. Other subgroups have been reported under atypical environments and are not included for simplicity.

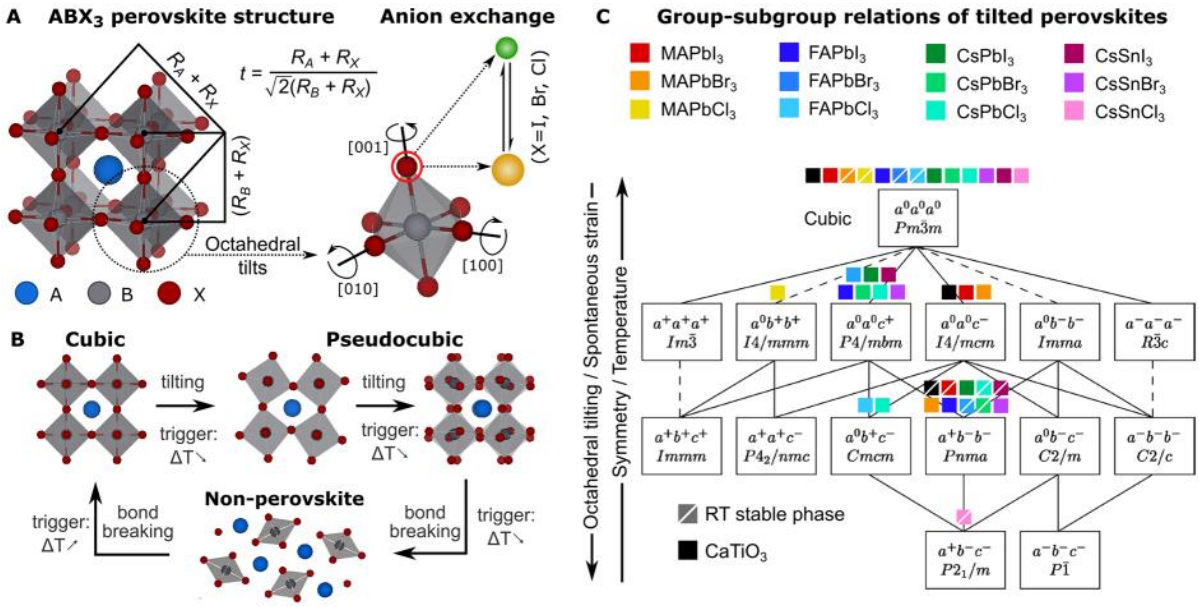

Source: (Steele *et al.*, 2020) without adaptations.

Figure 5C overviews the most common 15 different space groups of tilted perovskites predicted by the group-subgroup theory. The Glazer notation is used to classify the octahedral distortion throughout the crystal during thermal expansion or decrease (Howard e Stokes, 1998). For example, the $CaTiO_3$ perovskite exhibits the phase sequence upon heating as *Pnma*→*I4/mcm*→ $Pm\bar{3}m$ above 1000 °C (Yashima e Ali, 2009). Anion exchange can be achieved by partially or totally substituting halide ions. The flexible lattice and abundance of vacancies enable switching during or post-synthesis with an abundant source of halide precursors or a mixture of other anion species (see **Figure 5**A). The halide concentration drives the diffusion of ions into the crystal lattice, and as a result, bandgaps are dominantly dependent on the anion composition and valence. Thus, this phenomenon provides diverse relations on structural, physical, and optical properties. Additionally, anion exchange can modify or shift the photoluminescence (PL) emission across the visible spectrum (Bella *et al.*, 2016; Protesescu

et al., 2015). Proper anion exchange has been demonstrated to be versatile enough to modify the structures and properties of metal halide perovskites (Schmidt-Mende *et al.*, 2021).

Structural phase transitions result in significant changes in the physicochemical properties of materials, enabling the formation of phase-ferroics and phase-change optical devices. This allows deep insights into the current investigations of halide perovskites, and the experimental demonstrations of temperature and pressure-induced SPT open a pathway towards their discovery and understanding. This inspires the potential applications of perovskites in different devices, as the paradigm of crystal structure defining properties remain open, and it is the principal objective of this work in different family compounds. In this context, this thesis is structured as follows: Chapter 2 describes the methodology used for sample preparation and characterization techniques in detail. Chapter 3 investigates the erythrosiderite-type $A_2FeCl_5.H_2O$ (A = Cs, Rb, K, NH_4) family compounds at low temperatures, focusing on the ferroelastic structural phase transition in $Cs_2FeCl_5.H_2O$. Chapter 4 presents a study of the structural phase transition in $DMAPbX_3$ (X = Br, I) samples via an order-disorder mechanism, including the optoelectronic effects observed at low temperatures in $DMAPbI_3$. Chapter 5 investigates extreme conditions of low-temperatures and high-pressures in $CsCuCl_3$, characterizing the spin-phonon coupling at low temperatures and observing a structural phase transition at high pressures. Finally, it presents the conclusions and perspectives regarding the potential applications of these materials in future research.

2 EXPERIMENTAL SECTION

This chapter presents the experimental methods and analyses employed in this thesis, which are divided into three main sections: (1) synthesis of several investigated compounds, (2) characterization of materials under extreme conditions using a range of techniques, and (3) computational studies to complement experimental data.

2.1 Synthesis Method

The synthesis of various family compounds is critical for obtaining materials with tailored properties that can be used in various applications. The materials synthesized used the erythorosiderite-type family $A_2FeCl_5.H_2O$ (A= K, Rb, Cs, NH_4), the DMA-based hybrids perovskites $DMAPbX_3$ (X= Br, I), and the coupled-chain structure like-perovskite $CsCuCl_3$.

- *The erythorosiderite-type family $A_2FeCl_5.H_2O$ (A= K, Rb, Cs, NH_4) compounds:* Single crystals of $A_2FeCl_5 \cdot H_2O$ with orange prismatic and plumose morphology were obtained using the slow evaporation method. A mixture of HCL (47 wt% in H_2O), deionized water (18.6 MΩ cm, Milli-Q®, Millipore), and the stoichiometric amounts [2:1] of ACl and $FeCl_3.6H_2O$ were used to prepare the solution. The solution was heated at 70 °C for 3h after being sealed in a beaker with paraffin film with small holes and was then placed for two days at room temperature. The single crystals were at the bottom of the beaker, and the compounds were removed from the solution and cleaned with toluene.

- *DMA-based hybrids perovskites $DMAPbX_3$ (X= Br, I)*: Single-crystals of both $DMAPbX_3$ were obtained using the crystallization method from an N-N-Dimethylformamide (DMF) solution. Stoichiometric amounts of PbX_2 (X= Cl^-, Br^-) (4 mmol) and DMAX (X= Cl^-, Br^-) (4 mmol) were dissolved by adding 5 ml of DMF. The obtained solutions were filtered through 0.45 μm PTFE filters to minimize nucleation sites. Colorless needle-shaped single crystal of $DMAPbBr_3$ were obtained upon slow evaporation of the solvent at room temperature after several days. Additionally, polycrystalline powders of $DMAPbX_3$ were obtained by placing the single crystal in an agate mortar and carefully grinding with a pestle (García-Fernández *et al.*, 2017, 2019; Rodríguez-Hernández *et al.*, 2022).

- *The coupled-chain structure like-perovskite $CsCuCl_3$:* Dark red needles of $CsCuCl_3$ single crystals were grown using the slow evaporation method from acidic HCl (47 wt% in H2O)

containing stoichiometric amounts [1:1] of CsCl and $CuCl_2$. The preparation was heated at 120 °C for 1h. After heating, the solution was placed at room temperature and sealed in a beaker with paraffin film with small holes. The crystals were collected and cleaned with toluene.

2.2 Experimental Measurements

Various techniques were employed to investigate the structural-property relationship under extreme conditions. At low temperatures, Single Crystal X-Ray Diffraction (SCXRD), Differential Scanning Calorimetric (DSC), Raman spectroscopy, Photoluminescence and thermos-microscopy, while at high pressures, Synchrotron Powder X-Ray Diffraction (SPXRD), and Raman spectroscopy.

- ***Single crystal X-ray diffraction (SCXRD) measurements:*** Were conducted using a Bruker D8 Venture X-ray diffractometer equipped with a Photon II Kappa detector and Mo K radiation (λ = 0.71073 Å). Crystals were selected and mounted on a MiTeGen MicroMount using immersion oil. The crystals were cooled at various rates using a nitrogen gas cold stream from an Oxford Cryosystems cooler. The data were collected and integrated using APEX2 software (Bruker (2018), 2018). The Bruker SAINT software package (Bruker (2018), 2012) was used for data reduction and global cell refinement. The structures were solved by direct methods using the SHELXT (Sheldrick, 2015a) and refined by least-squares methods on SHELXL (Sheldrick, 2015b) included in Olex (Dolomanov *et al.*, 2009). The crystallographic illustrations were prepared in MERCURY (Macrae *et al.*, 2020) and VESTA software (Momma e Izumi, 2011).

- ***Differential scanning calorimetric (DSC)***: The analyses were conducted in a Netzsch Maia 200 F3. The samples were heated and cooled under a nitrogen atmosphere for several cycles at 5-10 $K.min^{-1}$.

- ***Raman spectroscopy at low-temperatures:*** The Raman-active low-temperature spectra were collected using a T64000 Jobin–Yvon spectrometer equipped with an Olympus microscope and an LN_2-cooled CCD to detect the scattered light. The spectra were excited with an Argon ion laser ($\lambda = 514$ nm). The temperature-dependent spectra were obtained by keeping the sample in a vacuum inside a He-compressed closed-cycle

cryostat. The temperature was controlled by a Lakeshore 330 controller that kept the precision around 0.1 K. Each Raman spectrum was deconvoluted into the sum of Lorentzian functions, respectively, by Fityk software (Wojdyr, 2010).

- ***Photoluminescence (PL):*** The PL spectra were collected using a T64000 Jobin–Yvon spectrometer equipped with an Olympus microscope and an LN_2-cooled CCD to detect the emitted radiation of the sample in a single mode. The spectra were excited with an external lamp (405 nm) using a long working distance plan-achromatic objective of 20x. The temperature-dependent spectra were obtained by keeping the sample in a vacuum inside a He-compressed closed-cycle cryostat for PL analyses. The temperature was controlled by a Lakeshore 330 controller that kept the precision around 0.1 K. The photoluminescent curves were adjusted with a Pearson7 fit profile using Fityk following the quantitative analysis of emission spectra for Kambhampati & Mooney (Mooney e Kambhampati, 2013).
- ***Thermo-microscopy:*** To collect images of samples at low temperatures, the Thermo-microscopy was conducted using an optical polarizing hot-stage microscopy station. The images were obtained from 300 to 125 K using a rate of 5 K/min lens magnification of 10x, recorded with a QICAM (Fast1394) camera, and processed in the Linkesys32 software. The temperature around the sample was controlled using the THMS600 LINKAM hot-stage station. Each photograph was taken after waiting about 4 seconds for temperature stabilization and attaining the equilibrium structure. The CellProfiler (Stirling *et al.*, 2021) software was used to edit the images.

- ***Synchrotron Powder X-Ray Diffraction (SPXRD):*** The SPXRD diffractograms were measured at the LNLS-SIRIUS, EMA beamline in the Laboratório Nacional de Luz Synchrotron (LNLS), Campinas, São Paulo. The collected data was integrated image per image using DIOPTAS (Prescher e Prakapenka, 2015) software, and the extracted XRD powder data was refined by EXPO 2014 (Altomare *et al.*, 2013).

- ***Raman spectroscopy at high-pressures:*** The pressure-dependent spectra were obtained using a membrane diamond anvil cell (MDAC) with a 350 μm diameter culet to achieve varying pressure levels. Stainless steel gaskets (200 μm of thickness, indented to 45 μm) with holes of about 150 μm served as the sample chamber. The pressure-transmitting medium was paraffin oil, Nujol. The ruby pressure gauge method was employed to

quantify the relationship between the applied pressure and line emission. The method involves using a ruby crystal as a pressure gauge to measure pressure changes based on the shift in the ruby's emission line (Shen *et al.*, 2020). The powder of $CsCuCl_3$ and ruby were placed together in the gaskets without contact. The Raman spectra obtained were analyzed by deconvoluting each spectrum into the sum of Lorentzian functions using Fityk software (Wojdyr, 2010).

2.3 Computational Details

Theoretical calculations in this study were conducted using the density functional theory (DFT) as implemented in the Quantum-ESPRESSO package (Giannozzi *et al.*, 2009, 2017). Firstly, structural optimization was performed using the SG15 Optimized Norm-Conserving Vanderbilt pseudopotentials (Hamann, 2013), followed by Γ-point phonon calculations. The phonon frequencies were calculated using the density functional perturbation theory (DFPT), with the exchange-correlation term determined within the generalized gradient approximation (GGA) parameterized by Perdev-Burke-Ernzerhof (PBE) (Perdew, Burke e Ernzerhof, 1996). The local-density approximation (LDA) was also employed for the exchange-correlation term for Raman intensity calculations. It is important to note that all calculations were carried out using the computational resources of the Centro Nacional de Processamento de Alto Desempenho em São Paulo (CENAPAD-SP) Project 823.

3 ERYTHOROSIDERITE-TYPE $Cs_2FeCl_5.H_2O$ COMPOUND AT LOW-TEMPERATURES

The erythrosiderite-type compounds are a class of halides complexes with the chemical formula $A_mBX_5.H_2O$, where A is occupied by elements such as alkali metals A = Li, Na, K, Rb, Cs or even little inorganic molecules such as ammonia (NH_4) or its deuterated equivalent ND_4, and B are transition metals as Cr, Mn, Fe, Co, Ni, Cu, with halide ions as fluorides (F), chlorides (Cl), bromides (Br) and iodides (I) serving as X anions. Among these compounds, the family $A_2FeX_5.H_2O$ (A = K, Rb, Cs, NH_4) have attracted significant attention due to its zero-field low-temperature antiferromagnetic phase transition occurs between 6-14 K (Alberto Rodríguez-Velamazán et al., 2015; Clune et al., 2019a; Rodríguez-Velamazán et al., 2017, 2018), making them traditionally magnetoelectric compounds. This chapter describes the investigation of the ferroelastic phase transition exhibited by $Cs_2FeCl_5.H_2O$ at low temperatures. Differential scanning calorimetric (DSC), Single crystal X-ray diffraction (SCXRD) and Raman spectroscopy measurements at low temperatures were used to investigate such phase transition.

3.1 Introduction

Multiferroic compounds refer to materials with more than one ferroic order related to ferromagnetism, ferroelectricity, or ferroelasticity within a narrow temperature range (Liang *et al.*, 2019). On the other hand, magnetoelectric materials are compounds that couple ferroelectricity and ferromagnetism and have been extensively investigated due to the interplay between magnetism and electricity (Dong *et al.*, 2015; Hughey *et al.*, 2022; Spaldin e Ramesh, 2019). This coupling allows the manipulation of magnetic properties through electric fields, making these materials attractive for their rich fundamental physics and potential industrial applications (Bichurin, Petrov e Tatarenko, 2020; Fiebig, 2005; Wang, Liu e Ren, 2009). Although magnetoelectric materials are not necessarily multiferroic, all multiferroics are linear magnetoelectrics, meaning that the applied electric or magnetic field induces a change in magnetization that is linearly proportional to its magnitude (Spaldin e Fiebig, 2005). An example of a multiferroic compound with magnetoelectric applications is erythrosiderite-related $(NH_4)_2FeCl_5.H_2O$, which belongs to the family of compounds with the basic formula $A_2FeCl_5.H_2O$, where A can be any alkali metal (Alberto Rodríguez-Velamazán *et al.*, 2015; Rodríguez-Velamazán *et al.*, 2017, 2018). The crystal structures of these compounds are orthorhombic with the space group *Pnma* for A = NH_4, K, Rb and *Cmcm* for A = Cs, respectively (Carlin e Palacio, 1985; Greedan *et al.*, 1980; Smirnov *et al.*, 2009). Both structure

types are closely related but not isomorphic (see **Figure 6** (a) and (b)). They consist of isolated A^+ units and isolated complex groups $[FeCl_5(H_2O)]^{2-}$ of sixfold octahedrally coordinated iron(III). The unit cells contain eight symmetrically equivalent A^+ cations and four $[FeCl_5(H_2O)]^{2-}$ octahedra. H-bonding between octahedra stabilizes the crystal structures and forms zigzag chains that run along *b*- for A = (NH_4), K, Rb, or *c-axis* for A = Cs. The magnetic ordering phenomena in the $A_2FeCl_5.H_2O$ family members have been subject to various investigations. The exploration of this property for potassium (K) and ammonium (NH_4) molecules was first observed in 1978, wherein the two isomorphic compounds showed a non-isomorphic antiferromagnetic (AFM) order transition at low temperatures, and a complete list of Neel temperatures are described in **Table 1**, with information about the crystal structure cell parameters.

Figure 6 – Room-temperature crystal structures of $A_2FeCl_5.H_2O$ **(a)** *Pnma*: $Rb_2FeCl_5.H_2O$ and **(b)** *Cmcm*: $Cs_2FeCl_5.H_2O$.

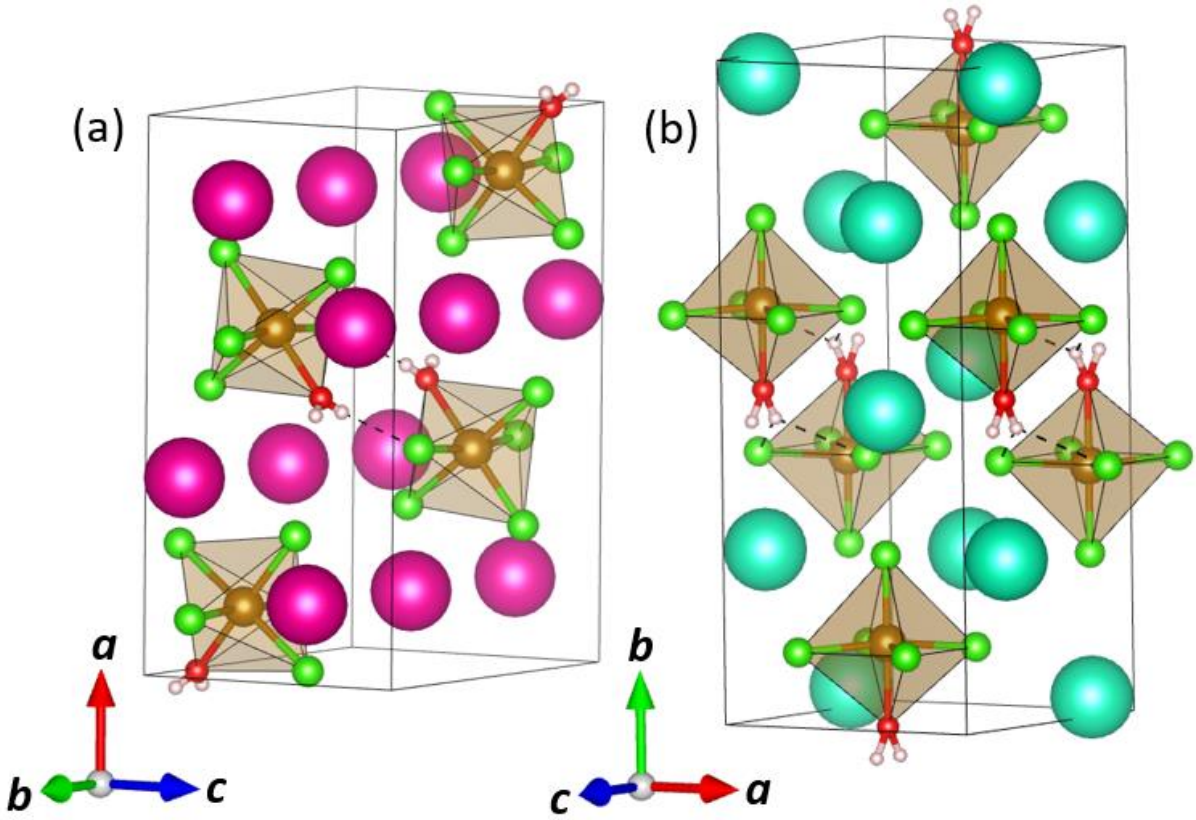

Source: Elaborated by the author.

Table 1 – Room-temperature lattice constants and Néel temperatures $A_2FeCl_5.H_2O$ with A = (NH_4), K, Rb, Cs.

	$(NH_4)_2FeCl_5.H_2O$	$K_2FeCl_5.H_2O$	$Rb_2FeCl_5.H_2O$	$Cs_2FeCl_5.H_2O$
Space Group	*Pnma*			*Cmcm*
a (Å)	13.706	13.5795	13.825	7.426
b (Å)	9.924	9.7024	9.918	17.306
c (Å)	7.024	7.0147	7.100	8.064
Ref:	(Ackermann *et al.*, 2014; Tian *et al.*, 2018)	(Gabas *et al.*, 1995)	(Becerra *et al.*, 1995; Gabas *et al.*, 1995)	(Fröhlich *et al.*, 2018; Greedan *et al.*, 1980)
T_N (K)	AFM_1: 7.25 AFM_2: 6.90	10.06	10.03	6.5
Ref:	(Alberto Rodríguez-Velamazán et al., 2015; Berlie, Cavaye e Le, 2022; Clune et al., 2019b; Lee, 2022; Rodríguez-Velamazán et al., 2017; Tian et al., 2018)	(Campo *et al.*, 2008; Gabas *et al.*, 1995; Lee, 2022; Luzón *et al.*, 2008)	(Gabas *et al.*, 1995; Lee, 2022; Luzón *et al.*, 2008)	(Freitas, Paduan-Filho e Becerra, 2015; Fröhlich *et al.*, 2018)

Source: Elaborated by the author.

$Cs_2FeCl_5{\cdot}H_2O$ has been found to display an antiferromagnetic state at 6.5 K, which determines the ferromagnetic behavior of the sample. Also, the compound is the only $A_2FeCl_5.H_2O$-related family member that shows a structural phase transition to a *C2/c* space group at low temperatures (151.5 K) (Ackermann *et al.*, 2013). Even though this SPT has already been reported on the $Cs_2FeCl_5{\cdot}H_2O$ sample, the ferroelasticity behavior is not discussed. According to Aizu (Aizu, 1970a; b), this SPT belongs to the *mmmF2/m* ferroic specie, which is a proper full ferroelastic. To investigate the ferroelasticity of the sample, a combination of single-crystal X-ray diffraction (SCXRD) and Raman spectroscopy at low temperatures, along with differential scanning calorimetry (DSC). The transition from the high-temperature paraelastic (*HT-phase*) phase to the low-temperature ferroelastic *(LT-phase*) phase is related to the displacement of the $[FeCl_5.H_2O]$ octahedra through a displacive mechanism, which has been confirmed by the hard-modes observed in Raman spectroscopy. To further study the ferroelasticity of $Cs_2FeCl_5.H_2O$, the strain matrix theory was employed to analyze the lattice-temperature dependence, which indicated that symmetry-strain e_5 component coupled with the

parameter order. Hence, it suggests a novel ferroic order in $Cs_2FeCl_5.H_2O$ at low temperatures. Specifically, a full ferroelastic transition at T_s = 156 K was weakly first-order (or nearly second-order). This ferroelastic *mmmF2/m* transition displays potential applications in multifunctional devices that harness the coupling between different ferroic orders. Combining the different ferroic orders could enhance functionality and improve device performance.

3.2 Low-temperature ferroelastic phase transition in multiferroic $Cs_2FeCl_5.H_2O$

The crystal structure and chemical composition of the $Cs_2FeCl_5.H_2O$ sample were confirmed using single-crystal X-ray diffraction. The compound crystallizes into an orthorhombic system with space group *Cmcm* (63) with cell parameters *a* = 7.458 (13) Å, *b* = 17.370 (3) Å, *c* = 8.054 (13) Å, and V = 1043.00 (3) $Å^3$ which is in good agreement with previous reports (Fabelo *et al.*, 2017; Fröhlich *et al*., 2018). At low-temperatures, the $Cs_2FeCl5.H_2O$ sample undergoes a structural phase transition (SPT) to the monoclinic *C*2/*c* system at T_s = 160 K (Fröhlich *et al*., 2018). To understand the symmetry relations between the two phases of the compound was used a lattice of maximal group-subgroup diagram from *Cmcm* (63) to *C*2/*c* (15) (see **Figure 7** (a)). The DSC thermogram was obtained for $Cs_2FeCl_5.H_2O$ in the temperature range of 140 to 170 K with a heating rate of 5 $K.min^{-1}$. The results confirm a reversible first-order SPT in $Cs_2FeCl_5.H_2O$ at T_C = 156 K during the heating cycle (blue curve), and at T_C = 160 K during the cooling cycle (red curve), exhibiting a small hysteresis of about 4 K. In DSC thermograms, the area below each calorimetric peak indicates the enthalpy (ΔH) and entropy (ΔS) due to the SPT. In this case, it was obtained ΔH = 0.2656 $J.g^{-1}$ and ΔS = 0.8581 $J.K^{-1}.mol^{-1}$ during the cooling process, while ΔH = 0.32336 $J.g^{-1}$ and ΔS = 1.1386 $J.K^{-1}.mol^{-1}$ during the heating process. Thus, the highest ΔS value obtained was $\Delta S = 0.2R \ln 2$, where *R* = 8.314 $K^{-1}.mol^{-1}$ is the universal gas constant. This value suggests that this SPT has a displacive behavior (Majzlan, Tangeman e Dachs, 2021).

Figure 7 – Group-Subgroup relation between *Cmcm* and *C*2/*c* space groups.

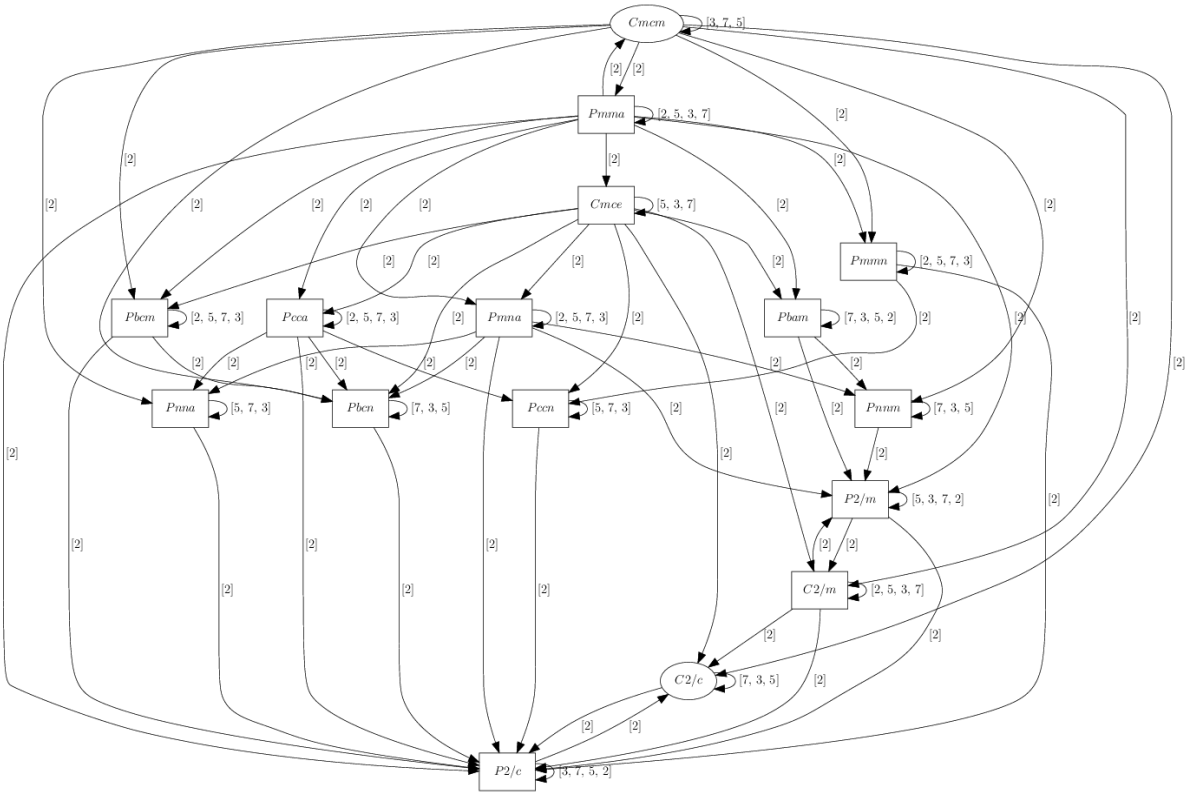

Source: (Ivantchev *et al.*, 2000) without adaptations.

To clarify the discussion about the displacive mechanism of this SPT, the *C*2/*c* monoclinic structure was transformed into the non-conventional space group *I*2/*c*, which are related by: $a_I = -a_C - c_C$, $b_I = b_C$, and $c_I = c_C$, where subscripts *I* and *C* are associated with *I*2/*c* to *C*2/*c* structures, respectively. Thus, at 100 K, in this new monoclinic set, $Cs_2FeCl_5.H_2O$ has the lattice parameters a = 17.117 (1) Å, b = 7.362 (3) Å, c = 16.135 (1) Å, β = 90.020 (3)° and V = 2030.65 (12) Å^3. **Figure 8** (b) shows the most significant differences between *Cmcm* and *I2/c* structures. As observed, the displacive mechanisms that drive the SPT in $Cs_2FeCl_5.H_2O$ are (i) a slight tilt about φ = 1° around the c_I axis; and (ii) an inclination of a water molecule by θ = 71°. Both mechanisms can be seen in **Figure 8** (b).

Figure 8 – **(a)** DSC thermogram obtained for $Cs_2FeCl_5.H_2O$ at 5 $K.min^{-1}$ in the temperature range from 140 to 170 K. **(b)** Comparison between high- and low-temperature $Cs_2FeCl_5.H_2O$ crystalline structures. The solid black box indicates that the Cs^+ ions were not plotted in the unit cell in both structural projections.

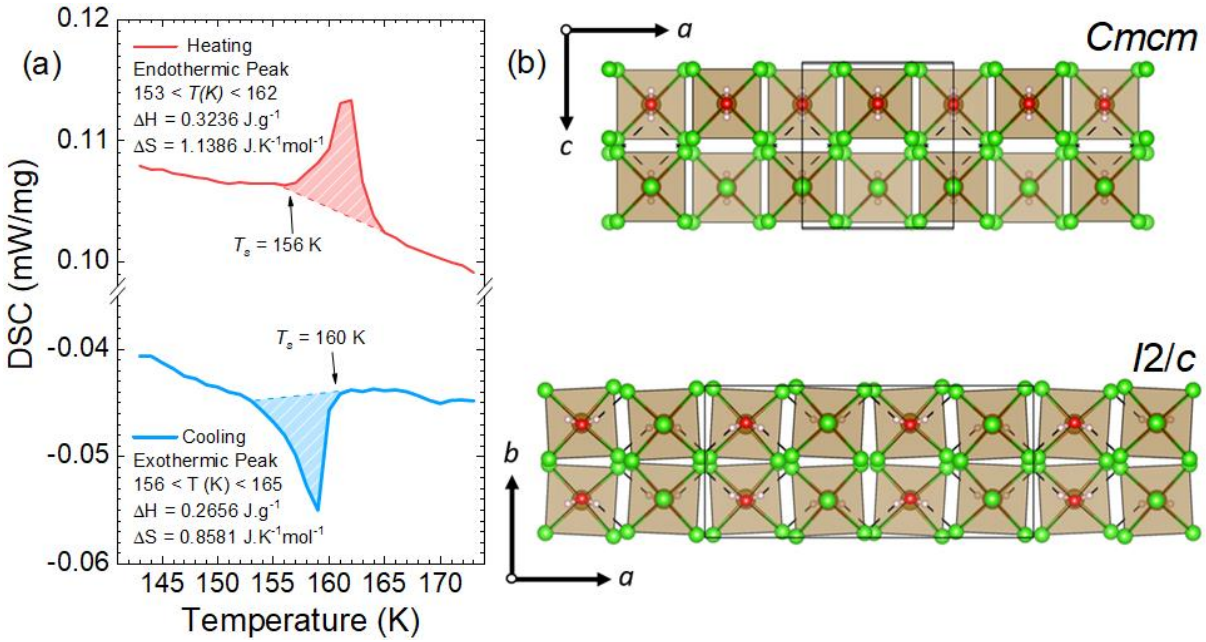

Source: Elaborated by the author.

To understand the importance of the intermolecular interactions involved in the SPT, Hirshfeld surface analyses for the $[FeCl_5.H_2O]$ octahedra were performed in both phases. The red-white-blue surfaces indicate intermolecular contacts that are shorter (red), around (white), and longer (blue) than van der Waals contacts (McKinnon, Jayatilaka e Spackman, 2007; Yuan *et al.*, 2019). As shown in **Figure 9**, both phases display a similar surface geometry, with intermolecular contacts Cs···Cl, H···Cl, Cl···Cl, Cs···O, H···H, and Cs···H represented in the 2D fingerprint. Regarding the changes in the 2D fingerprint plots, Cs···Cl (**Figure 9** c-k), and H···Cl (**Figure 9** d-l) did not show a significant change in their geometry distribution surface in both phases. However, the H···Cl contact weakens by approximately 2% contribution in the *LT-phase*. Such a difference suggests a weakening of H···Cl contact between the octahedra. The Cl···Cl exhibits a sharp tip in the *HT-phase* (**Figure 9**e) that becomes thinner in *LT-phase* (**Figure 9** m), but the contribution remains the same. Around the Cs···O (**Figure 9** f-o) and Cs···H (**Figure 9** h-p) interactions, significant modifications in their contribution were not displayed. However, the new geometry form of the 2D fingerprint plots in the Cs···H interactions proposes a displacement around the Cs ion, making them responsible for the movement of octahedra, as the Cs^+ ion oriented the $[FeCl_5.H_2O]^{2-}$. On the other hand, the H···H interactions (**Figure 9** g-n) increase the contribution of the total surface after the SPT (by

approximately 2%), which is attributed to the hardening of these ligands, compensating for the weakening H···Cl contact.

Figure 9 – Separated phases of **a)** and **i)** The Hirshfeld surfaces, **b)** and **j)** sum of all interconnects (mapped with d_{norm})decomposed fingerprint plots for both [$FeCl_5.H_2O$] octahedra resolved into **c)** and **k)** for Cs···Cl, **d)** and **l)** for H···Cl, **e)** and **m)** for Cl···Cl, **f)** and **o)** for Cs···O, **g)** and **n)** for H···H, and **h)** and **p)** for Cs···H contacts to *HT-phase* and *LT-phase*, respectively. Full fingerprints appear as grey shadows underneath.

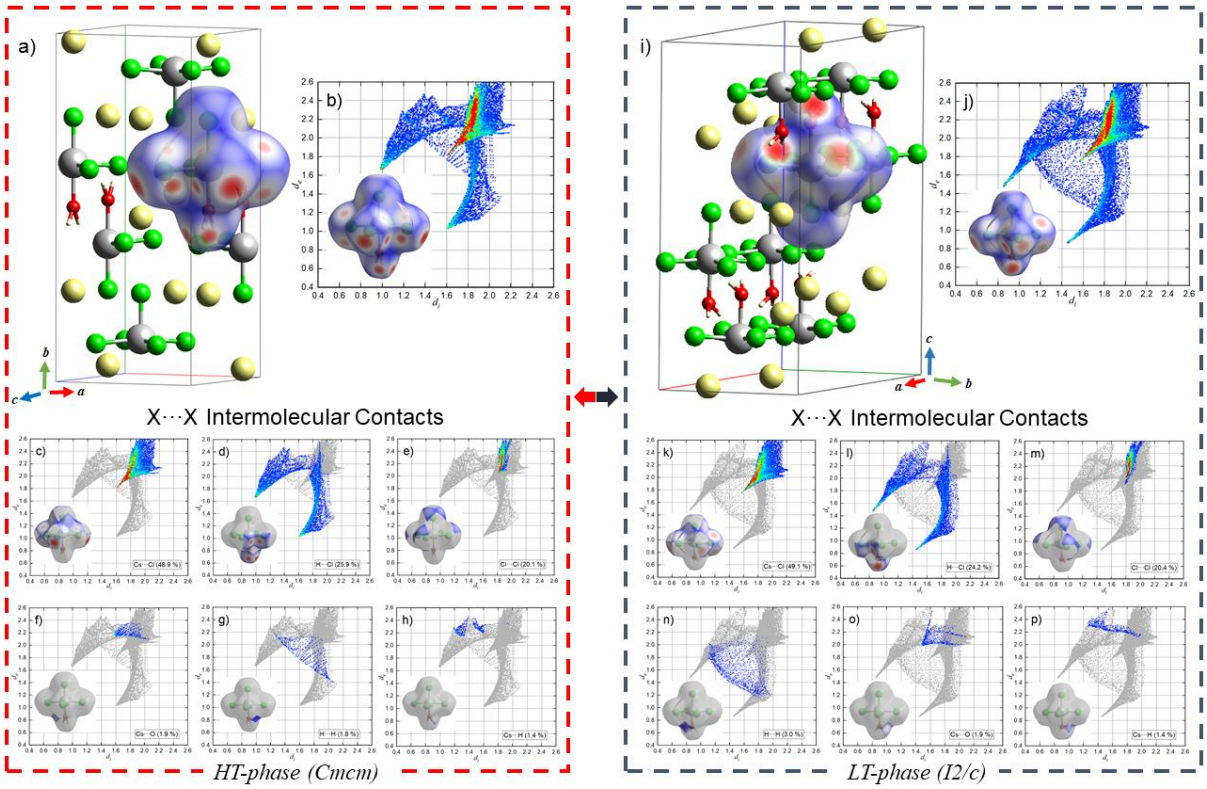

Source: Elaborated by the author.

Ferroelastic crystals are materials that exhibit two or more orientational states that can switch between them, displaying spontaneous strain components (e_i). These modifications in their group symmetries define the ferroic state and order (Carpenter, Salje e Graeme-Barber, 1998; Salje, 2013). During the structural phase transition from *Cmcm* (*HT-phase*) to *I2/c* (*LT-phase*), the number of symmetry elements decreases from 8 (*E, i, 3C2, 3σ*) to 4 (*E, i, C2, σh*). In principle, the relation of the *mmm* point group (*Cmcm*) to the *2/m (I2/c)* is a proper full ferroelastic transition between both phases, which is related to the Aizu-*type* ferroelastic species *mmmF2/m* (Sapriel, 1975). This SPT should be a proper full ferroelastic transition whose order parameter is the e_5 strain component (using the Voigt notation).

To describe the ferroelastic features of this SPT, the temperature-dependent unit-cell parameters of the crystal were measured, where a direct relationship between both phases following changes in the monoclinic cell parameters was established: *a**= *b*, *b**= *a*, *c**= *c/2*, and V*= V/2. This new basic set is a simple transformation from the *I*2/*c* monoclinic base to the *Cmcm* orthorhombic. **Figure 10** shows the linear temperature dependencies of the lattice parameters. At T_c = 158 K, all of them, including the unit cell volume, show a change in the slope of the temperature dependence, which agrees with the DSC measurements given in **Figure 8** (a). The temperature dependence of the lattice parameters is generally related to the linear thermal expansion (see **Figure 10**) and the spontaneous strain components along the SPT. Thus, the linear thermal expansion α can be calculated as:

$$l_i(T) = l_{0i}(1 + \alpha_i T) \tag{3}$$

where the sub-index i indicates the lattice cell parameters *a*, *b* and *c* (Angel, Gonzalez-Platas e Alvaro, 2014; Cliffe, Goodwin e Road, 2012), while l_{0i} is the lattice parameter at the lower measured temperature for each temperature phase. The obtained linear thermal expansion coefficients are summarized in **Table 2**.

Table 2 – Principal linear thermal expansion coefficients α_i $(i = a, b, c)$ in both $Cs_2FeCl_5.H_2O$ crystal phases along with the corresponding principal axes.

		Component of x_i along with the crystallographic cell parameters			
	α_i (MK^{-1})	*a*	*b*	*c*	*Approximate axis*
HT-Phase	22 (1)	0	0	1	[001]
	54 (2)	-1	0	0	$[\bar{1}00]$
	61 (1)	0	-1	0	$[0\bar{1}0]$
LT-Phase	40 (2)	0	-1	0	$[0\bar{1}0]$
	109 (3)	0.92	0	0.39	[301]
	133 (5)	-0.35	0	0.94	$[\bar{1}03]$

Source: Elaborated by the author.

It was observed that a positive thermal expansion (PTE) occurred along all crystallographic axes in both phases. Above the SPT, a decrease to half of the PTE coefficient was observed in all crystalline directions. This trend is related to the relationship between the crystal unit volume and phases $2V_m \approx V_o$. In fact, the total sum of the individual thermal expansion components for each phase is the thermal expansion volume. The final calculated values are α_V^{HT}= 138 MK^{-1} and α_V^{LT}= 282 MK^{-1} for each phase, respectively.

Figure 10 – Temperature-dependent lattice parameters of $Cs_2FeCl_5.H_2O$. The subscripts "*o*" and "*m*" indicate the orthorhombic and monoclinic cells, respectively.

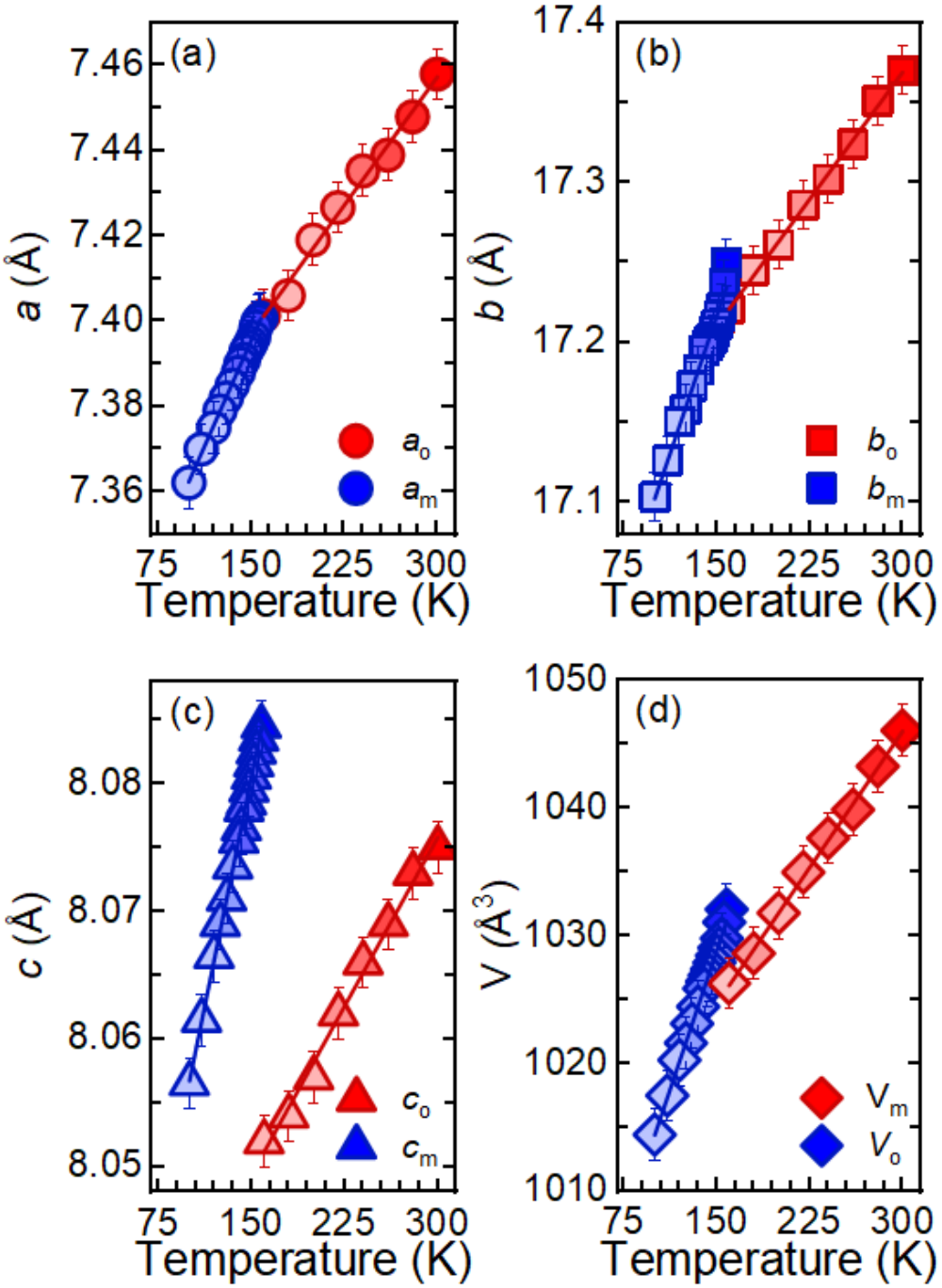

Source: Elaborated by the author.

Based on this temperature-dependent lattice parameter, the components e_i of the spontaneous-strain tensor in their main crystal axes were calculated using the following relation (using Voigt notation):

$$e_i = \begin{pmatrix} e_1 & 0 & e_5 \\ 0 & e_2 & 0 \\ 0 & 0 & e_3 \end{pmatrix} = \begin{pmatrix} (a-a_0)/a_0 & 0 & \frac{1}{2}(c(cos(\beta))/c_0) \\ 0 & (b-b_0)/b_0 & 0 \\ 0 & 0 & (c(sin(\beta))-c_0)/c_0 \end{pmatrix} \quad (4)$$

where a_0, b_0, and c_0 are the lattice parameters at room temperature (a_0 = 7.43 Å, b_0 = 17.40 Å, and c_0 = 8.07 Å). **Figure 11** shows all calculated components of the spontaneous strain, as well as the analogous volume strain $V_s = (V - V_0)/V_0$, and the scalar spontaneous strain (e_s) is given by:

$$e_s = ({e_1}^2 + {e_2}^2 + {e_3}^2 + 2{e_5}^2)^{1/2} \quad (5)$$

Figure 11 – Temperature-dependence of the spontaneous strain e_i components, of volume strain (V_s) and scalar spontaneous strain (e_{ss}) of the $Cs_2FeCl_5.H_2O$

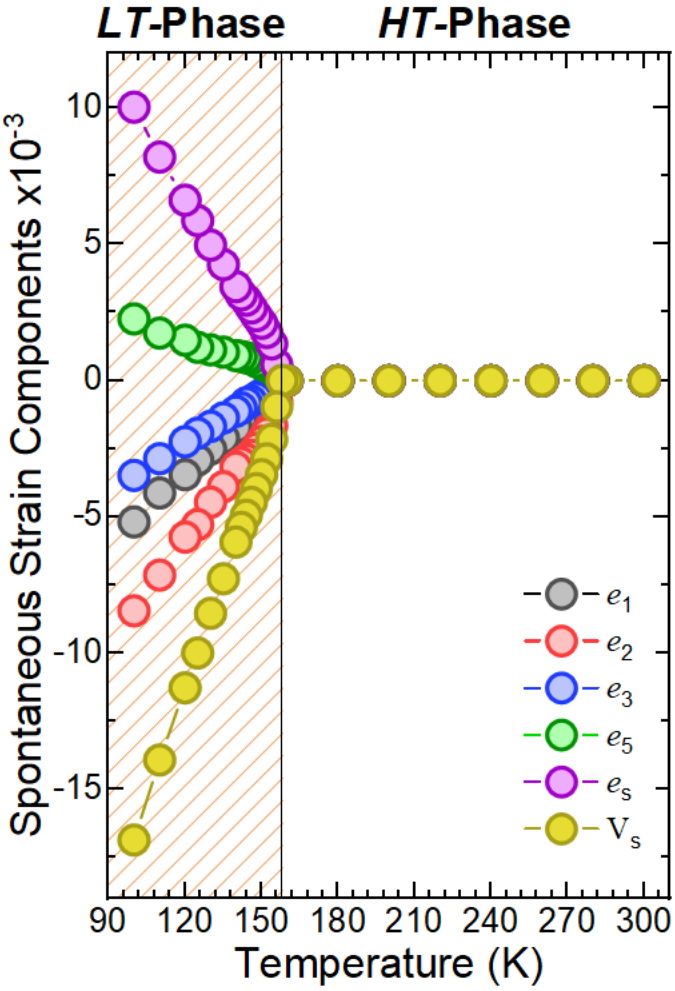

Source: Elaborated by the author.

Since the strain analysis in the *mmmF*2/*m* species reveals that all component calculations present ferroelasticity, the primary order parameter of the structural phase

transition defined in Landau theory, usually called q, behaves as the symmetry-adapted strain. In some cases, it may be coupled with the spontaneous strain components ($e_i \propto q$ or $e_i \propto q^2$) (Ardit, Martucci e Cruciani, 2015; Chen et al., 2022). According to (Aizu, 1970a), the unique symmetry-adapted strain in *mmmF*2/*m* is e_5. To validate the symmetry criteria, the following conditions in e_5 need to be checked: a) the volume strain is equivalent to the sum of the strain tensor components parallel to the reference axes (i,e, $e_1 + e_2 + e_3$); b) the primary order spontaneous strain and the scalar strain (e_s) are proportional; and c) the volume strain varies linearly with q^2(Aizu, 1970a; b; Ardit, Martucci e Cruciani, 2015; Carpenter, Salje e Graeme-Barber, 1998; Chen et al., 2022; Salje, 2013; Sapriel, 1975). These conditions were verified and shown in **Figure 12**.

Figure 12 – Validation of the e_5 as the symmetry-adapted strain order parameter: **(a)** sum of the linear strain vs. the volume strain, **(b)** spontaneous strain e_5 with the scalar strain modification, and **(c)** ${e_5}^2 \propto V_s$ dependence.

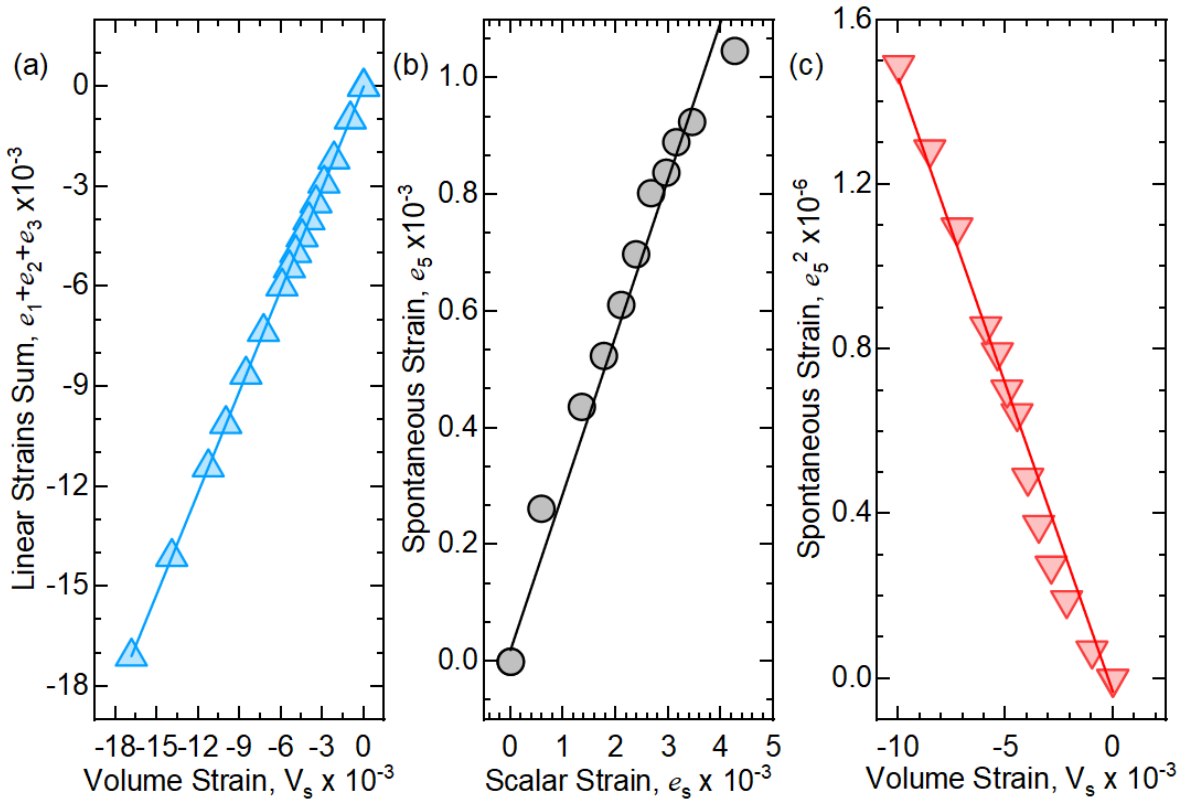

Source: Elaborated by the author.

As shown, the e_5 coupled with the order parameter of the SPT, which could be described as a function of the scaling law near the critical temperature given by:

$$e_5 = A(T_c - T)^{2\beta} \quad (6)$$

where 2β is the critical exponent of the order parameter. **Figure 13** shows the scaled temperature dependence of e_5, whose fit agrees with a $\beta = 1/4$ or 2β = 1/2 as expected for a second-order SPT (Chen *et al.*, 2021; He *et al.*, 2021; Lee, Choi e Lim, 2021). The symmetry-breaking strain e_5 describes a relationship with a single elastic constant C_{55} related to the *mmm* ⇌ *2/m* transition. The equilibrium variation of e_5 based on the Landau expansion (G) is generally expressed as:

$$G = G_0 + \frac{1}{2}A(T - T_c)e_5 + \frac{C}{6}{e_5}^2 \tag{7}$$

where T_c is the critical temperature, and A and C are constant. For this potential, the elastic constant C_{55} associated with the strain e_5 is given by:

$$C_{55} = \begin{cases} A(T - T_c), & T < T_c \\ 4A(T - T_c), & T > T_c \end{cases} \tag{8}$$

Figure 13 – **(a)** Temperature dependence of the spontaneous strains e_5 (symmetry-adapted strain), and **(b)** Linear slope modification of the elastic constant as C_{55} [2:1] relationship**.**

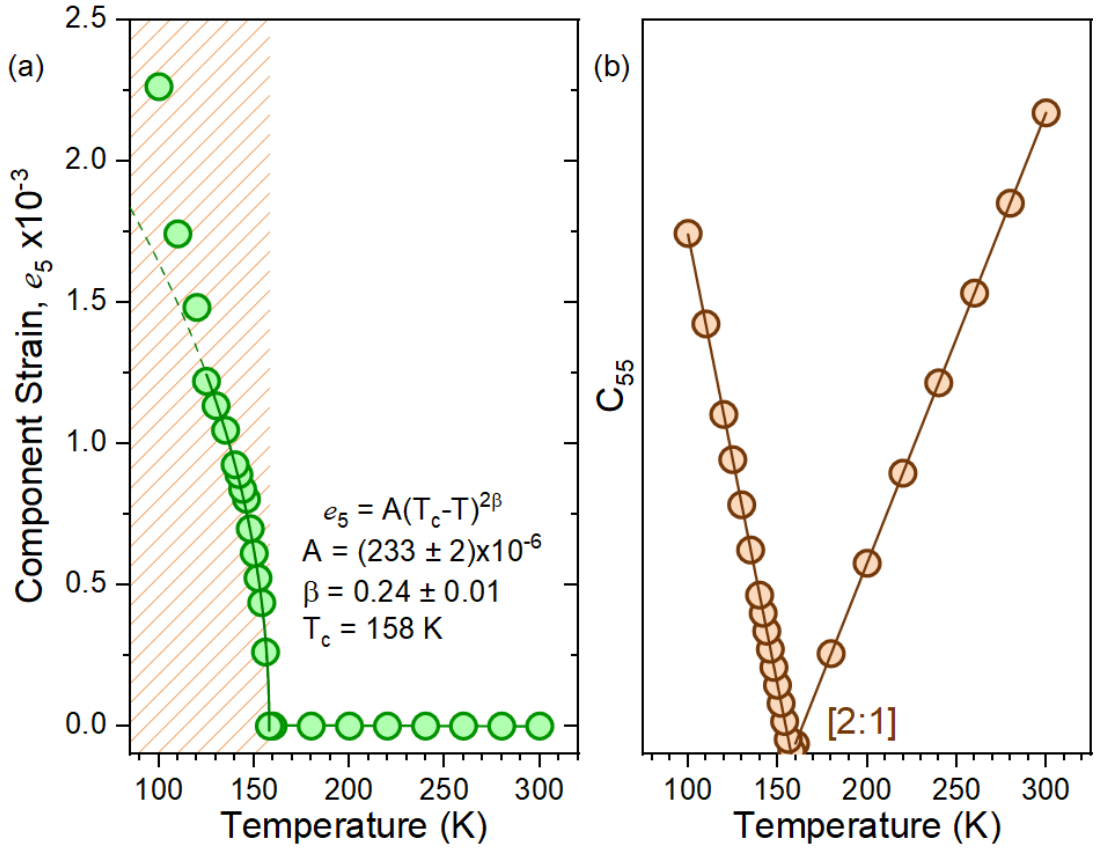

Source: Elaborated by the author.

Thus, the constant elastic behavior along the transition was calculated. The elastic constant goes to zero linearly at the critical point, and the slopes below and above T_C = 158 K described a [2:1] ratio between them (Allardo *et al.*, 2000; Carpenter e Salje, 1998; Chen *et al.*, 2021; He *et al.*, 2021; Salje, Hayward e Lee, 2005; Zhang *et al.*, 2020). Hence, take into account the strain analysis; the $Cs_2FeCl_5.H_2O$ at T_s = 156 K presents a ferroelastic second-order structural phase transition.

Raman spectroscopy is a sensitive technique for detecting ferroic transitions in materials. To study the temperature-dependence of Raman-active spectra of $Cs_2FeCl_5.H_2O$. The Raman-active modes at the center of the Brillouin zone (Γ-point) in each phase, based on group theory (Rousseau, Bauman e Porto, 1981), according to the factor group analysis for the *mmm* factor group. Such modes can be reduced in terms of the irreducible representations of this group as $\Gamma_{raman}^{HT} = 10A_g \oplus 9B_{1g} \oplus 4B_{2g} \oplus 10B_{3g}$.

Figure 14 – Raman spectrum of $Cs_2FeCl_5.H_2O$ in **(a)** 20-200 cm^{-1}, **(b)** 200-750 cm^{-1}, **(c)** 1550-1700 cm^{-1} and **(d)** 3300-3650 cm^{-1} range at room-temperature.

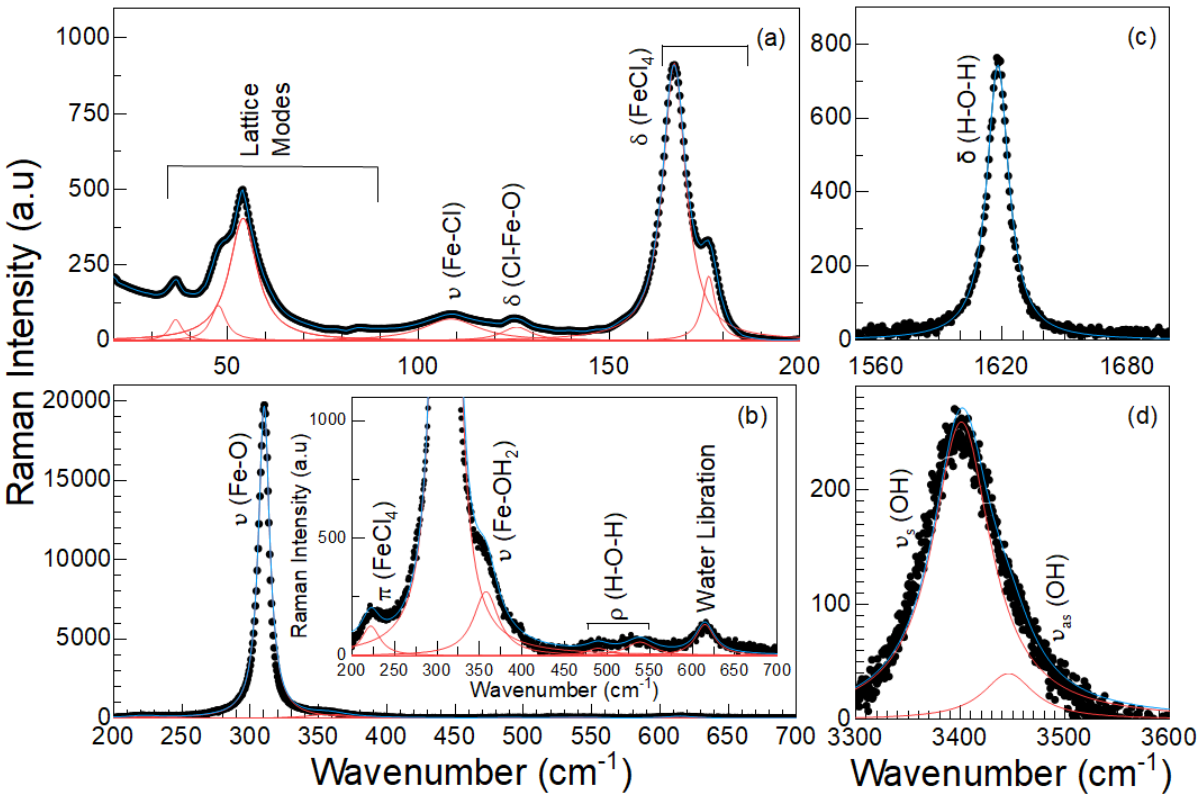

Source: Elaborated by the author.

Figure 14 shows the obtained Raman spectrum of $Cs_2FeCl_5.H_2O$ at room temperature in selected wavenumber ranges. It was observed 18 Raman-active modes in $Cs_2FeCl_5.H_2O$ in the 20-3650 cm^{-1} range. For wavenumbers lower than 750 cm^{-1}, 14 bands are related to the lattice, octahedra internal modes and water librations, and the other 4 are to water vibrations. Around 1600 cm^{-1} is observed in the mode corresponding to the δ (H-O-H) (Piszczek, Grodzicki e Engelen, 2003). This peak feature is a useful indication of the sample purity for the sharping format and the characteristic frequency value around for all family series $(A)_2FeCl_5.H_2O$ (A = NH_4, K, Rb, Cs). Finally, for wavenumbers between 3300 to 3600 cm^{-1}, three different peaks are observed, which are related to the water molecule symmetric and asymmetric stretching modes.

Table 3 – Frequencies (ω_n in cm^{-1}) and proposed assignments of room-temperature experimental Raman-active modes in $Cs_2FeCl_5.H_2O$ and the comparison for similar compounds $(A)_2FeCl_5.H_2O$ (A = NH_4, K, Rb, Cs) (Adams e D. C. Newton, 1972; Adams e Lock, 1971; McCarthy e Walker, 1983; Parker *et al.*, 1997; Piszczek, Grodzicki e Engelen, 2003; Sharma e Pandya, 1974).

# Mode	Frequency	Symmetry	Mode Assignment Attribution	Reference Value
ω_1	37	B_{1g}	Lattice Mode	37 cm^{-1}
ω_2	47	A_g	Lattice Mode	46 cm^{-1}
ω_3	54	A_g	Lattice Mode	53 cm^{-1}
ω_4	88	B_{1g}	Lattice Mode	87 cm^{-1}
ω_5	109	-	υ (Fe-Cl)	101–103 cm^{-1}
ω_6	126	B_{1g}	δ (Cl-Fe-O)	127–129 cm^{-1}
ω_7	167	A_g	δ ($FeCl_4$)	167 cm^{-1}
ω_8	176	B_{1g}	δ ($FeCl_4$)	174–180 cm^{-1}
ω_9	226	$A_g \oplus B_{1g}$	π ($FeCl_4$)	210–224 cm^{-1}
ω_{10}	311	A_g	υ (Fe-O)	293–320 cm^{-1}
ω_{11}	356	A_g	υ (Fe-OH_2)	350–384 cm^{-1}
ω_{12}	489	B_{1g}	ρ (H-O-H)	460 cm^{-1}
ω_{13}	538	A_g	ρ (H-O-H)	540 cm^{-1}
ω_{14}	615	-	Water Libration	655 cm^{-1}
ω_{15}	1618	-	δ (H-O-H)	1591 cm^{-1}
ω_{16}	3401	-	υ_s (OH)	3400 cm^{-1}
ω_{17}	3446	-	υ_{as} (OH)	3460 cm^{-1}

Source: Elaborated by the author.

Table 3 summarizes all the observed modes and their assignments, which were proposed based on previous literature (Adams e D. C. Newton, 1972; Adams e Lock, 1971; McCarthy e Walker, 1983; Parker *et al.*, 1997; Piszczek, Grodzicki e Engelen, 2003; Sharma e Pandya, 1974). **Figure 15** shows the normalized temperature-dependent Raman spectra for

selected wavenumbers. At low temperatures, $Cs_2FeCl_5.H_2O$ exhibits such mode distribution in terms of the irreducible representation of their respective point groups as $\Gamma_{raman}^{LT}=33A_g \oplus 33B_g$. The correlation between both vibrational modes phases is related to the *mmm* (D_{2h}) → *2/m* (C_{2h}) symmetry change. Hence, it must be observed: *i)* the A_g modes in *HT-phase* turn on A_g vibrations at *LT-phase*, *ii)* the B_{1g} and B_{2g} symmetry modes in the *mmm* change into B_g at *2/m*, and *iii)* the modification of the Raman-active mode B_{3g} in high-temperature phase to an A_g in low-temperature.

Figure 15 – Temperature dependent Raman spectra obtained for $Cs_2FeCl_5.H_2O$ in wavenumber ranges: **(a)** 20-200 cm^{-1}, **(b)** 200-300 cm^{-1}, **(c)** 300-320 cm^{-1}, **(d)** 320-650 cm^{-1}, **(e)** 1600-1680 cm^{-1} and **(f)** 3300-3600 cm^{-1}.

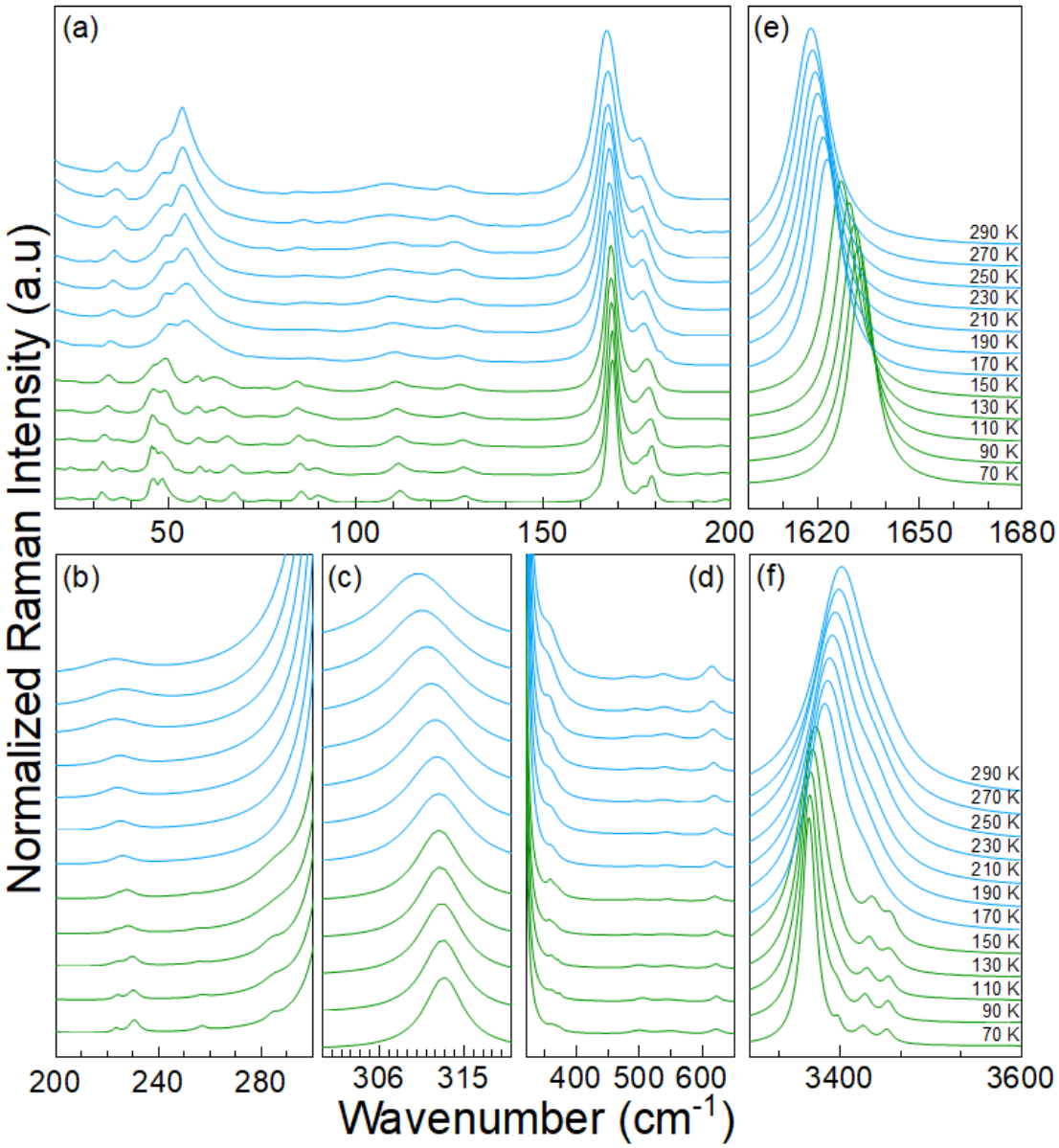

Source: Elaborated by the author.

The Raman spectra are different in both phases of the sample. The main changes are: (i) around 50 cm^{-1}, we have two bands that transform into four bands with a drastic change on mode profiles; (ii) an abrupt change in the position of the δ (H−O−H) mode around 1620 cm^{-1}; and (iii) strong anomalies in the H−O stretching modes observed between 3400 and 3500 cm^{-1}. Also, several new low-intensity modes were observed in the monoclinic phase. These features can be seen better in the temperature-dependent mode positions obtained from the spectra deconvolution by Lorentzian functions, shown in **Figure 16**.

Figure 16 – Temperature-dependence Raman mode positions obtained for $Cs_2FeCl_5.H_2O$ in wavenumber ranges: **(a)** 20-210 cm^{-1}, **(b)** 210-700 cm^{-1}, **(c)** 1616-1635 cm^{-1}, **(d)** 3300-3460 cm^{-1}

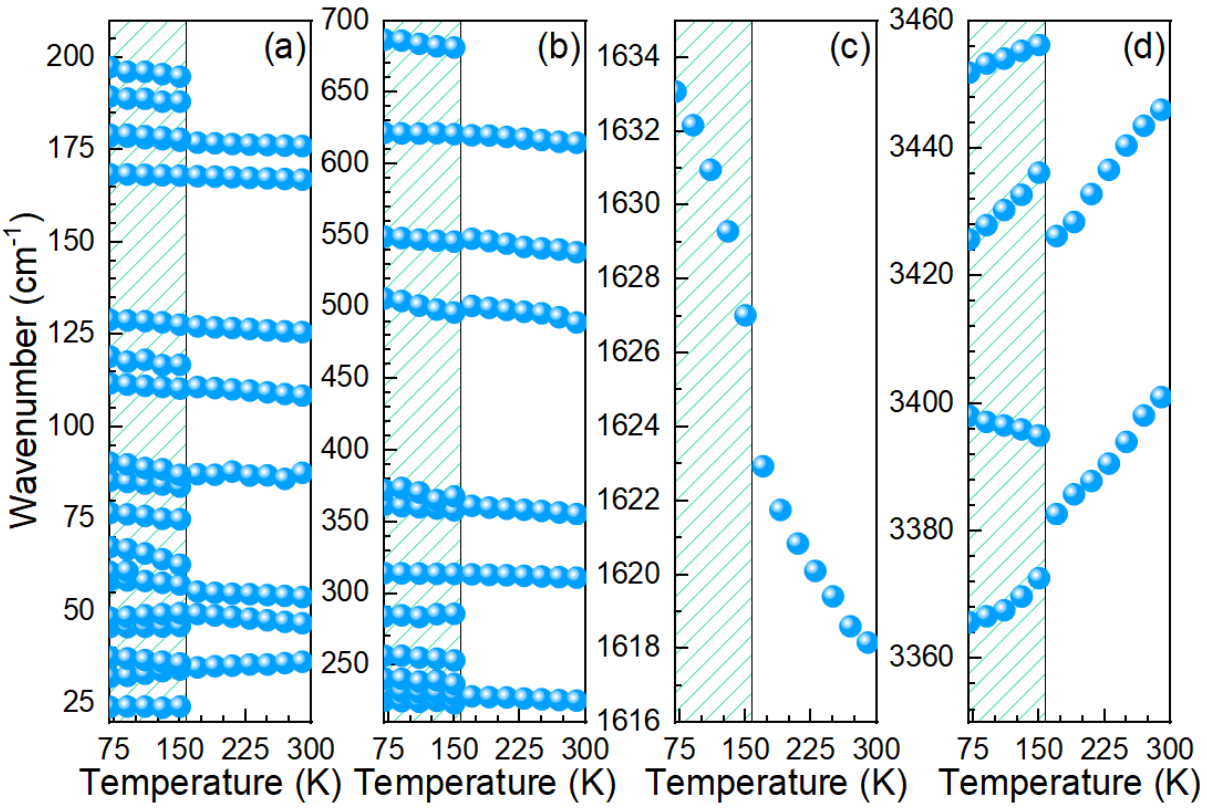

Source: Elaborated by the author.

All observed features involving water modes were expected since this molecule is important in the SPT of $Cs_2FeCl_5.H_2O$. In general, ferroic SPTs resulting from displacive mechanisms exhibit soft-mode features, as described by (Cochran, 1960) for ferroelectrics and by (Unruh, 1995) for ferroelastics. A soft-mode is a vibration of the high-symmetry phase whose frequency tends towards zero as the critical temperature approaches. This softening leads to the instability of the crystal against low-frequency phonons and is correlated with a critical temperature dependence of the quadratic term in the thermodynamic potential. However, ferroic

transitions can also exhibit hard-modes, where the frequency, intensity, and full width at half maximum (FWHM) are characteristic quantities related to the critical behavior of the macroscopic order parameter (Palmer, Bismayer e Salje, 1990; Salje e Bismayer, 1997; Scott, 1974). In ferroics, hard-modes typically depend on the order parameter Q, as given by the following expression:

$$(\Delta\omega)^2 = AQ^m + BQ^{2m} \tag{9}$$

The parameter m in equation (9) represents the faintness critical exponent that couples to the order parameter in the Landau free energy, with A and B dimensional constants. It has been previously established that the strain is the primary order parameter in proper ferroelastics. Equation (9) describes proper ferroelasticity for $m = 1$ (Aizu, 1972; Tolédano e Tolédano, 1980), while impropers correspond for $m \geq 2$ (Harter *et al.*, 2017). In pseudo-proper ferroelastics, the profile of the hard mode depends on $Q^m = (T_c - T)^m$, where T_c is the critical temperature. Therefore, for the experimental critical exponent of the order parameter obtained in equation (6), which is $m = 2\beta = 1/2$, the reduction of the temperature-dependent hard-mode frequency must follow the form for proper, improper, and pseudo-proper ferroelastics given by in the equation (9) as:

$$\begin{cases} (\Delta\omega)^2 = A(T_c - T) + B(T_c - T)^2 & Proper \\ (\Delta\omega)^2 = A(T_c - T)^2 + B(T_c - T)^4 & Improper \\ (\Delta\omega)^2 = A(T_c - T)^{1/2} + B(T_c - T) & Pseudo - Proper \end{cases} \tag{10}$$

Figure 17 shows the temperature dependence of selected Raman-active modes in $Cs_2FeCl_5.H_2O$. The low-temperature modes clearly describe the SPT in the sample. The fit of equation (10) for $T < T_c$ exhibit the behavior of the selected vibrations related to proper ferroelastics ($m = 1$ condition), indicating the presence of full proper ferroelasticity in the compound.

Figure 17 – Selected temperature-dependence Raman mode frequencies obtained for $Cs_2FeCl_5.H_2O$.

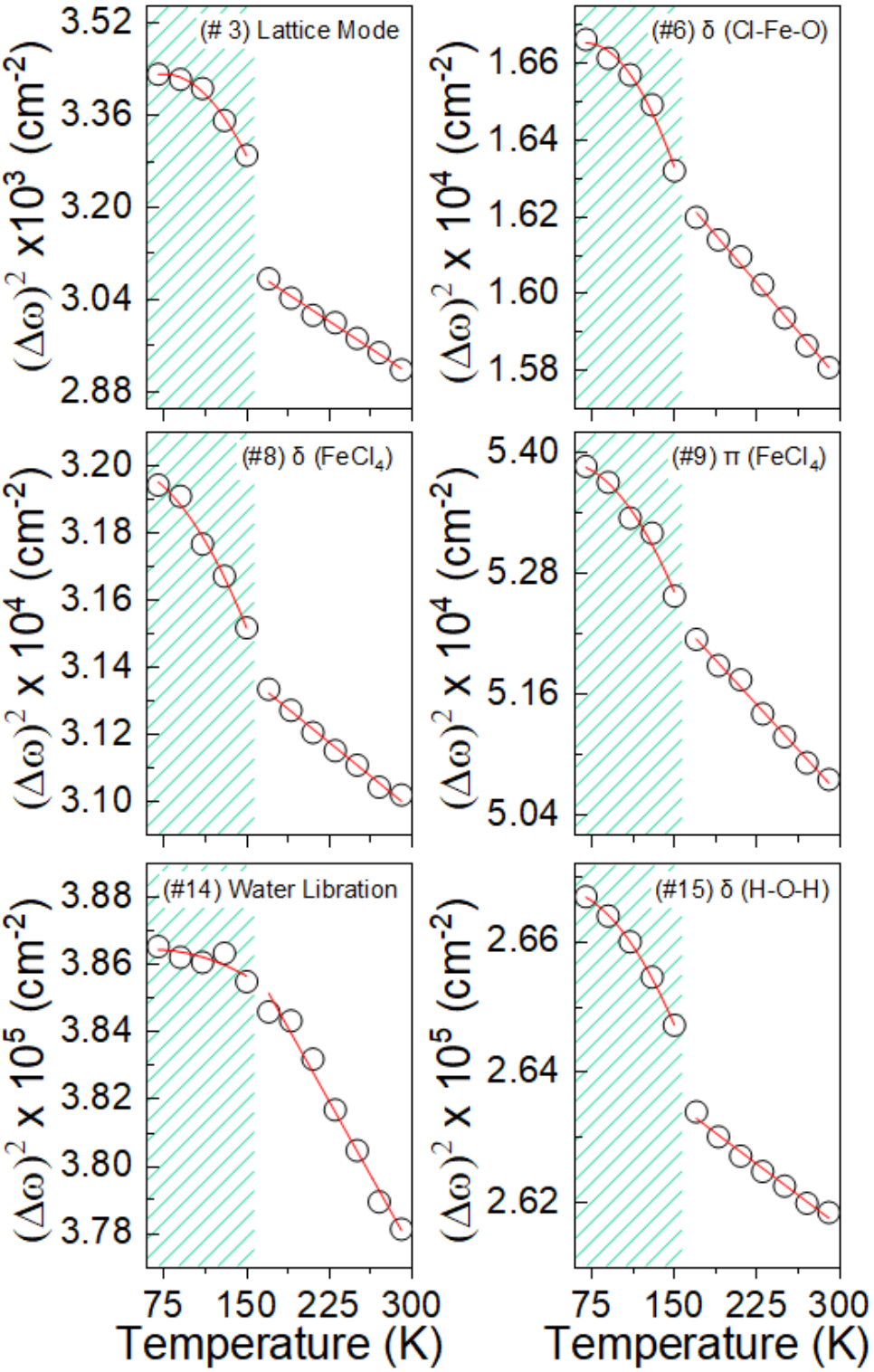

Source: Elaborated by the author.

Ultimately, the low-temperature SCXRD, DSC, and Raman spectroscopy were used to investigate the full ferroelastic Aizu-*type mmmF2/m* phase transition in $Cs_2FeCl_5.H_2O$,

thereby shedding new light on the novel ferroic order in this compound. Strain matrix theory has been employed to analyze the sample structural order and found that the strain-adapted symmetry component e_5 exhibits second-order behavior consistent with Landau theory. Our analysis shows that the transition is driven by a displacive mechanism of the $FeCl_5.H_2O$ octahedra, as revealed by DSC measurements, which show a first-order transition with the low-enthalpy present in the transition. Furthermore, the hard-mode displayed by Raman spectroscopy was used to validate the ferroelastic nature of the phase transition, which showed good agreement with the expression (9) for $m = 1$. This suggests that the compound presents both orders around the full ferroelastic transition, describing a weakly first-order (or nearly second-order) nature. Our results provide valuable insights into the complex ferroic behavior in $Cs_2FeCl_5.H_2O$ and suggest potential applications for this material in multifunctional devices that harness the coupling between different ferroic orders.

4 DMA-BASED HYBRIDS PEROVSKITES $DMAPbX_3$ (X= Br, I)

Hybrid halide perovskites (HHPs) have gained significant attention in optoelectronics due to their unique combination of tunable properties, solution processability, and low-cost fabrication. HHPs based on organic molecules, such as methylammonium (MA: $[CH_3NH_3]^+$), have attracted particular interest in the scientific community since their thin-film samples based on $MAPbI_3$ demonstrated record-breaking power conversion efficiencies in solar cells (22.1%) in 2014 (Huang *et al.*, 2017), his breakthrough spurred investigations into other organic ions to achieve similar or better results. For example, dimethylammonium (DMA: $[(CH_3)_2NH_2]^+$) has shown strong photoluminescence and promising properties for applications such as light-emitting diodes and lasers (McMeekin *et al.*, 2023). This chapter presents two distinct research, the investigation of order-disorder low-temperature structural transitions in $DMAPbBr_3$ using a combination of temperature-dependent synchrotron powder X-ray diffraction (SPXRD), differential scanning calorimetry (DSC) and Raman spectroscopy, which results were published in the high impact journal (*Journal of Materials Chemistry C*: IF-8.067) with a name: ***Uniaxial negative thermal expansion in the $[(CH_3)_2NH_2]PbBr_3$ hybrid perovskite*** (Rodríguez-Hernández *et al.*, 2022); and the study of the low-temperature dependence of the optical properties of $DMAPbI_3$ using thermomiscropy and photoluminescence.

4.1 Introduction

Lead hybrid halide perovskites are considered one of the biggest breakthroughs in the research field of solar cells in recent years. The confluence of several exceptional and unprecedented factors, including high efficiencies above 25% (Green *et al.*, 2022), abundant raw materials, and simple fabrication, makes lead halide perovskites very promising materials for the next generation of low-cost and high-efficiency photovoltaic technology (Yakunin *et al.*, 2015). Hybrid perovskite solar cells are based on organic–inorganic lead halide perovskites with the general formula $APbX_3$ where A is commonly an organic cation (such as methylammonium (MA) $[CH_3NH_3]^+$ or formamidinium (FA) $[CH(NH_2)_2]^+$), an inorganic cation (Cs^+) or a mixture of both types and X is a halide anion (Cl^-, Br^-, I^-) (Jeon *et al.*, 2014; Park, 2013). Despite the spectacular advances in improving efficiencies, many issues remain unclear and subject to debate, such as the origin of their photovoltaic performance and their light and thermal instability (Djurišić *et al.*, 2017).

Addressing these issues, cation engineering has provided a strategy to control the structure and properties of hybrid halide perovskites, resulting in solar cells with the highest

performance and improved stability. In this context, the effect of different dopants in the A-site has been tested in the last few years (Chatterjee e Pal, 2018; Gao *et al.*, 2020; Zhou *et al.*, 2018). Such studies have revealed that the introduction of a dimethylammonium (DMA) cation in this site leads to materials with high efficiencies (Chen *et al.*, 2019) that are highly stable (Eperon *et al.*, 2020). It is also worth noting that such doping can be intentionally promoted, as has been done in the hybrid perovskites ($MAPbI_3$ (Franssen *et al.*, 2018; Franssen, Heumen, Van e Kentgens, 2020; Ju *et al.*, 2017; Shi, Zhifang *et al.*, 2017), $MAPbBr_3$ (Anelli *et al.*, 2019; Simenas *et al.*, 2020), $CsPbI_3$ (Bian *et al.*, 2020; Ke *et al.*, 2018; Meng *et al.*, 2020; Pei *et al.*, 2019; Wang *et al.*, 2019) and $FA_xCs_{1-x}PbI_yBr_{3-y}$ (Kothandaraman *et al.*, 2020)); or it can take place unintentionally due to the formation of the DMA cation in the reaction medium as a consequence of the degradation of dimethylformamide (DMF), the most commonly used solvent for the synthesis of hybrid perovskites (Franssen, Heumen, Van e Kentgens, 2020; Ke *et al.*, 2018; Lee *et al.*, 2017). Dimethylamine obtained from the degradation of the DMF solvent plays an important role in solar cell crystallization and optoelectronic quality (Pei *et al.*, 2019).

Similar to MA-based HHPs, hybrids halide perovskites based on DMA ions have shown tunable optoelectronic properties that can be optimized for different applications, such as photovoltaics and light-emitting diodes. DMA-based perovskites have a smaller ionic radius than MA-based perovskites, which affects the material crystal structure and electronic properties (Wang *et al.*, 2021). DMA-based perovskites exhibit improved stability and moisture resistance compared to MA-based perovskites, making them attractive for practical applications (Chen *et al.*, 2019). The previous facts highlight the importance of investigating pure DMA-based perovskites to understand the role of DMA cations in mixed-cation hybrid perovskites (García-Fernández *et al.*, 2018; Mancini *et al.*, 2016). In this context, investigate the thermal evolution of the crystal structure of the $DMAPbBr_3$ compound, particularly close to its structural phase transition, to obtain information about the thermomechanical response and the relationship between its crystal structure and functional properties. To achieve this goal, the structural transition and lattice dynamics of the $DMAPbBr_3$ hybrid hexagonal perovskite were characterized by temperature-dependent Raman spectroscopy.

4.2 Order-disorder structural phase transition on $DMAPbBr_3$

From a structural perspective, $DMAPbX_3$ compounds exhibit hexagonal perovskite polytypes due to the relatively large size of the A-site cation, which is too large to fit into the cuboctahedral cavity of a conventional cubic perovskite (Nguyen e Cava, 2021). While compounds with Cl^- and Br^- exhibit a *4H*-hexagonal perovskite polytype, $DMAPbI_3$ presents a *2H*-hexagonal perovskite structure (García-Fernández *et al.*, 2017). The main difference between these polytypes is the arrangement of the inorganic framework. The *4H*-polytypes consist of $[Pb_2X_9]^5$ units formed by two face-sharing $[PbX_6]^4$ octahedra and bioctahedra connected by corner-sharing, forming a 3D framework. In contrast, the crystal structure of the *2H*-polytype comprises infinite chains of face-sharing $[PbI_6]^4$. In both cases, the DMA organic cations are located in the cavities or among the chains of the inorganic framework.

As the basic cubic hybrid lead halide perovskites (Faghihnasiri, Izadifard e Ghazi, 2017; Linaburg *et al.*, 2017; Wang, Xiao e Wang, 2020; Xu *et al.*, 2017), the *2H*- and *4H*-hexagonal perovskites also exhibit first-order thermally induced crystal structural phase transitions (SPT) at T_t, where the low-temperature (LT) phase transforms into a high-temperature (HT) phase upon heating. For $DMAPbBr_3$, an SPT occurs at T_t = 250 K, from an *LT-phase* with orthorhombic symmetry with space group (S.G) $P2_12_12_1$ to an *HT-phase* with hexagonal symmetry S.G: $P6_3/mmc$ (García-Fernández *et al.*, 2019). DSC measurements confirm the expected first-order structural phase transition described by (García-Fernández et al., 2019), as shown in **Figure 18**.

The difference between these polytypes lies in the arrangement of the inorganic framework. The *4H*-polytypes consist of $[Pb_2X_9]^5$ units formed by two face-sharing $[PbX_6]^4$ octahedra and bioctahedrons connected by corner-sharing, forming a 3D framework. In contrast, the *2H*-polytype has infinite chains of face-sharing $[PbI_6]^4$. In both cases, the DMA organic cations are in the cavities or among the chains of the inorganic framework. Both crystalline phases of $DMAPbBr_3$ crystal structures were confirmed using the *Le Bail* method using the EXPO-2014 method to refine the temperature-dependent synchrotron powder X-ray diffraction (SPXRD) patterns with those reported in the crystallographic database codes ICSD: 402591 from room temperature (Geselle e Fuess, 1997), and the CCDC:1855520 from low-temperatures (García-Fernández *et al.*, 2019) (see **Figure 19**).

Figure 18 – DSC results as a function of temperature obtained by heating and cooling cycles of the $DMAPbBr_3$ sample at $5K.min^{-1}$ in the 150-300K range.

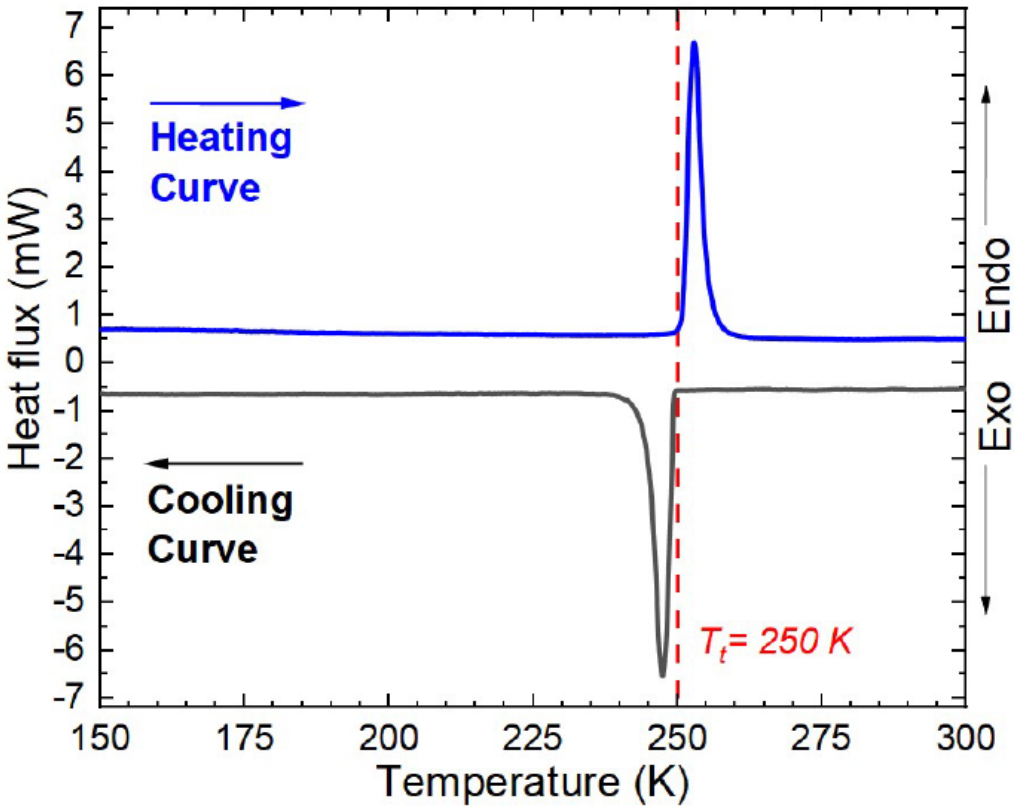

Source: Elaborated by the author.

The observed thermal hysteresis confirms the first-order phase transition, resulting in an entropy change (ΔS) of ~ 8.6 J mol^{-1} K^{-1} (heating) to 9.8 J mol^{-1} K^{-1} (cooling), mainly attributed to the disorder of the $[(CH_3)_2NH_2]^+$ guest. In the *LT-phase*, all atoms have unitary occupation factors, and the dipole moments associated with the DMA cations are arranged antiparallel. However, the DMA cations in the *HT-phase* are strongly disordered over two different configurations. These configurations are characterized by: (a) the DMA cations occupying the unobstructed hexagonal channels formed by the framework along the *c*-axis, where each C atom occupies eight positions (occupancy factors 0.17×6 for C_3 and 0.5 for C_1) while the N atoms are disorder over six sites (occupancy factors 0.17×6 for N_2), and (b) in which the N (N_1) atoms have a six-fold disorder, and the C (C_2) atom is split between two positions.

Figure 19 – The crystal structures of **(a)** $P6_3/mmc$ at 330 K with the ICSD: 402591, **(b)** the $P2_12_12_1$ at 130 K with the CCDC:1855520.

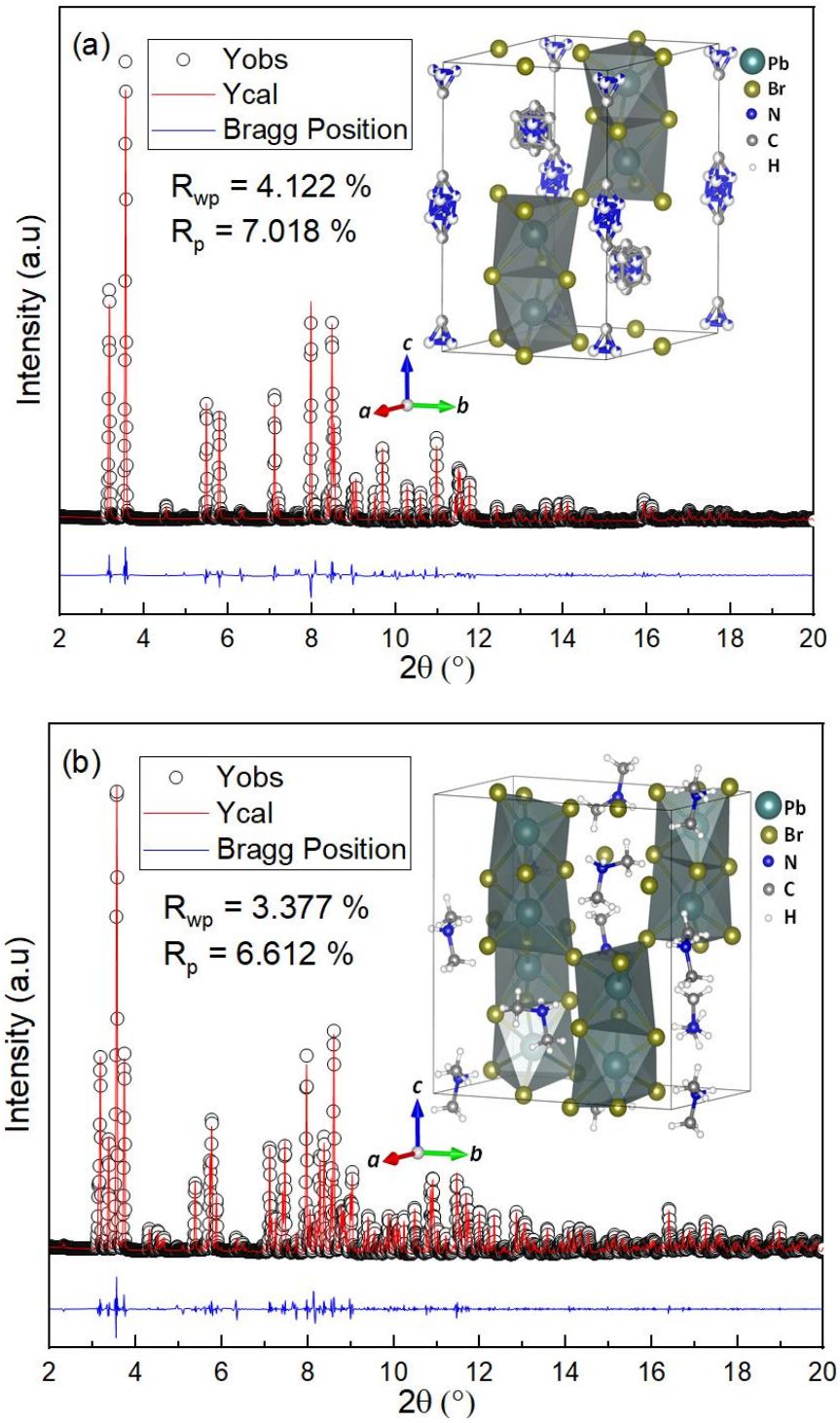

Source: Elaborated by the author.

According to crystallographic data analysis of the ordered to six-fold disordered $[(CH_3)_2NH_2]^+$ ions, the ratio of the respective numbers of microstates N_2/N_1, where N_1 and N_2 is the number of states possible states at low-phase and high-phase, respectively. Both phases

can be estimated using Boltzmann's equation $\Delta S = R\ln(N)$, where R is the gas constant, and N is the ratio of the number of configurations in the disordered and ordered systems. The corresponding value of $N = 6$ was calculated, and therefore, an entropy change of 14.9 J.mol^{-1} K^{-1} should be expected. This residual entropy suggests an important role for the relaxing character in the order-disorder mechanism involved in the transition (Du, Sun, *et al.*, 2015; Du, Xu, *et al.*, 2015; Samantaray *et al.*, 2012).

Figure 20 shows the obtained Raman spectra of both crystal *HT*- and *LT*- phases, which are similar to those reported for other hybrid halide perovskites with methylammonium (MA) cations (Lavan *et al.*, 2021; Nakada *et al.*, 2019; Quarti *et al.*, 2014), $FAPbBr_3$ FA= formamidinium (Ghosh *et al.*, 2021; Mączka e Ptak, 2022; Spirito *et al.*, 2022), $MHyPbCl_3$ [MHy (methylhydrazinium) = $CH_3NH_2NH_2]^+$ (Mączka *et al.*, 2020), and other compounds such as $(HA)_2PbX_4$ with X = Br or I and [HA (hexylammonium) = $C_6H_{13}NH_3]^+$, $(BA)_2PbI_4$ [BA (butylammonium) = $C_4H_9NH_3]^+$ and $(BNA)_2PbI_4$ [BNA (benzylammonium) = $C_6H_5CH_2NH_3]^+$ (Lavan *et al.*, 2021) (see **Table 4**).

Figure 20 – Raman spectra of $DMAPbBr_3$ at 300 K (orange) and 140 K (blue) in **(a)–(c)** low wavenumbers and **(b)–(d)** DMA-internal modes.

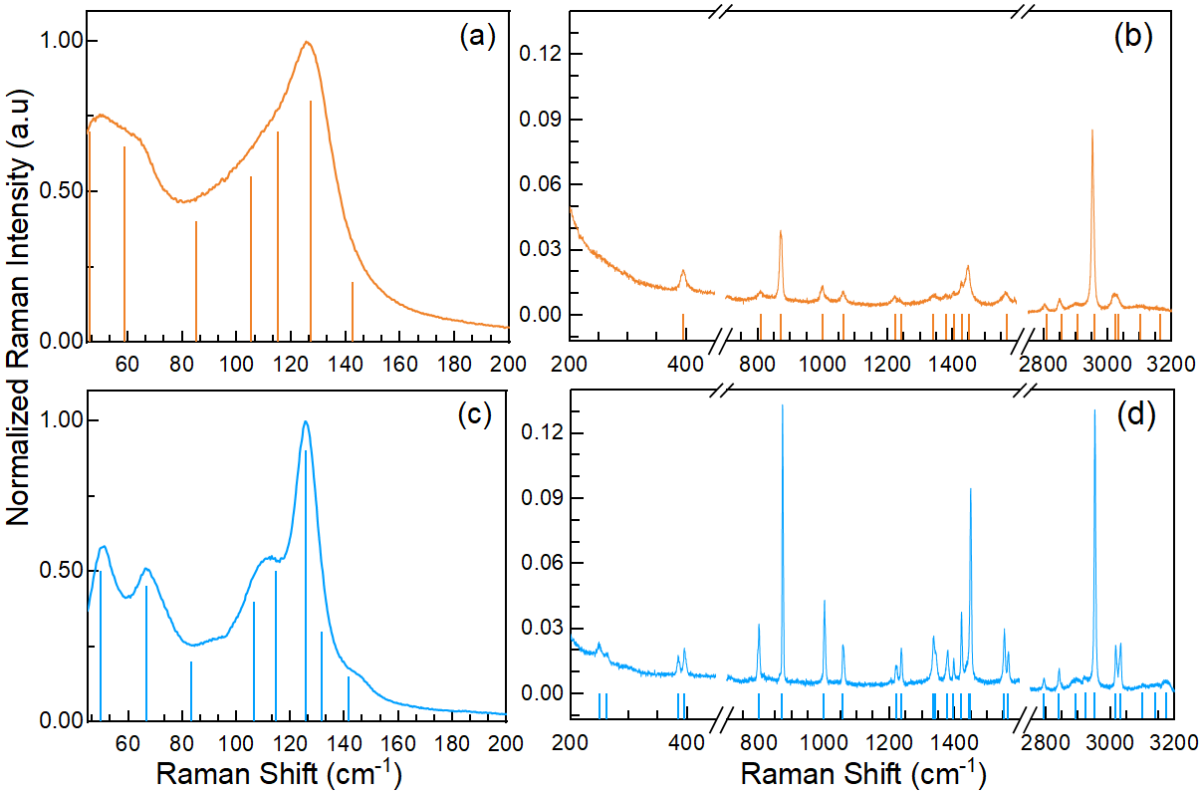

Source: Elaborated by the author

Table 4 – Frequencies (ν in cm^{-1}) and proposed assignments of experimental Raman-active modes in $DMAPbBr_3$ in both phases compared for similar compounds $APbX_3$ (A=DMA, MA, FA; X=Br, I, HCCO) (Ibaceta-Jaña *et al.*, 2020; Kontos *et al.*, 2020; Leguy *et al.*, 2016; Mączka, M. *et al.*, 2014; Niemann *et al.*, 2016; Pérez-Osorio *et al.*, 2015, 2018).

Mode (#)	$DMAPbBr_3$ 295K (cm^{-1})	$DMAPbBr_3$ 140K (cm^{-1})	Observed Position in Similar Compounds (cm^{-1})	Assignment
1	46	50	41-50	δ_s (Br-Pb-Br)
2	59	67	56-66	δ_{as} (Br-Pb-Br)
3	85	83	76-93	ν_s (Br-Pb-Br)
4	106	107	98-106	ν_{as} (Br-Pb-Br)
5	116	115	118	DMA Translation
6	128	126	126-129	DMA Libration
7	--	132	138	DMA Libration
8	143	142	145-175	DMA Libration
9	--	250	243-262	τ (H_3C-N-CH_3)
10	--	262	262-297	τ (H_3C-N-CH_3)
11	--	385	323-326	τ (H_3C-N-CH_3)
12	395	396	401-402	τ (H_3C-N-CH_3)
13	807	798	803	δ (H_3C-N-CH_3)
14	870	871	890-906	ρ (H_3C-N-CH_3)
15	998	1000	994	ν (H_3C-N-CH_3)
16	1063	1058	1030-1059	ν_{as} (H_3C-N-CH_3)
17	1222	1221	1227	ρ (CH_3)
18	1238	1236	1231-1236	ρ_s (CH_3)
19	1339	1335	1351-1353	δ_s (CH_3)
20	--	1343	1351-1353	δ_s (CH_3)
21	1379	1378	1366-1370	δ_s (CH_3)
22	1402	1397	1399-1403	δ_{as} (CH_3)
23	1427	1421	1416-1428	δ_s (NH_2)
24	--	1444	1444-1450	δ_s (NH_2)
25	1447	1449	1457-1478	δ_{as} (NH_2)
26	--	1553	1533-1536	δ_{as} (NH_2)
27	1563	1565	1544-1596	δ_{as} (NH_2)
28	2802	2792	--	ν (C-H)
29	2849	2841	2821-2845	ν_s (C-H)
30	2900	2892	2896	ν_s (C-H)
31	--	2923	2931-2938	ν_{as} (C-H)
32	2952	2951	2952-2966	ν_{as} (C-H)
33	3017	3016	3026	ν_{as} (C-H)
34	3029	3032	3030-3036	ν_s (N-H)
35	3095	3101	3080-3106	ν_s (N-H)
36	3157	3140	3124-3144	ν_{as} (N-H)
37	--	3174	3172-3179	ν_{as} (N-H)

Abbreviations: ν: stretching; δ: bending; τ: twisting/torsion; ρ: rocking; ω: wagging; as: asymmetric; s: symmetric.

Source: Elaborated by the author.

As shown in the Raman spectra of $DMAPbBr_3$ (see **Figure 20**), numerous bands are observed in the wavenumber range of 55 to 3200 cm^{-1}, with 37 modes in the *LT-phase* and 28 in the *HT-phase*. The bands are broad mainly at low wavenumbers, where the lattice modes are

located. This broadening is expected due to the disordered structure of the *HT-phase*. In contrast, at low temperatures (*LT-phase*), more defined modes and new modes are observed. The proposed assignment of the observed modes in both phases is provided in **Table 4**. Such assignment was based on a comparison of the measurement spectrum with other similar compounds with the same structural formula $APbX_3$, where A is an organic molecule such as DMA, MA, and FA, and X is an anion such as bromide (Br), iodide (I), and HCCO (formate).

Figure 22 to Figure 25 describe the temperature-dependent Raman spectra obtained for $DMAPbBr_3$ obtained in the temperature range from 10 K up to room temperature. The temperature-dependent spectra presented in **Figure 21** are related to Br–Pb–Br modes (40–110 cm^{-1}) and rigid-body motion of DMA organic cation modes (115–150 cm^{-1}). The Br–Pb–Br modes are more susceptible to the off-center shift of the lead atoms. It was observed that the bending modes at 46 and 59 cm^{-1} exhibit a standard softening on heating, while the stretching modes at 85 and 106 cm^{-1} undergo a sudden blueshift. These changes can be related to the shrinking of the bonds, as the octahedra become more regular and the Pb–Br bonds shorten and become stronger (García-Fernández *et al.*, 2019).

Regarding the spectrum range associated with the rigid DMA motion, the modes at 116, 128, and 143 cm^{-1} show significant changes in the mode position, highlighting the SPT at 250 K. The most intense band in this spectral region is the mode at 128 cm^{-1}, which is assigned to DMA rotation and exhibits such modifications. A new band (at 132 cm^{-1}) was also observed at low temperatures, which was assigned to another DMA libration (Leguy *et al.*, 2016). The modes in the wavenumber range higher than 200 cm^{-1} correspond mainly to the internal vibrations of the DMA-cation entities in channels/cavities. Although these band zone descriptions are present and well-defined in the Raman spectrum, the organic and inorganic sublattices can couple, causing lattice distortion (Grechko *et al.*, 2018; Menahem *et al.*, 2021). In particular, hydrogen bonding has been identified as a significant contribution to the relative stability of crystal phases that lead to organic cation ordering at low temperatures (El-Mellouhi *et al.*, 2016; Svane *et al.*, 2017).

Figure 21– **Left panel:** Temperature-dependent normalized Raman spectra obtained for the $DMAPbBr_3$ crystal range between 140-300 K in the 40–200 cm^{-1} range, **Right panel:** Temperature-dependent behavior of the mode positions observed in this wavenumber region.

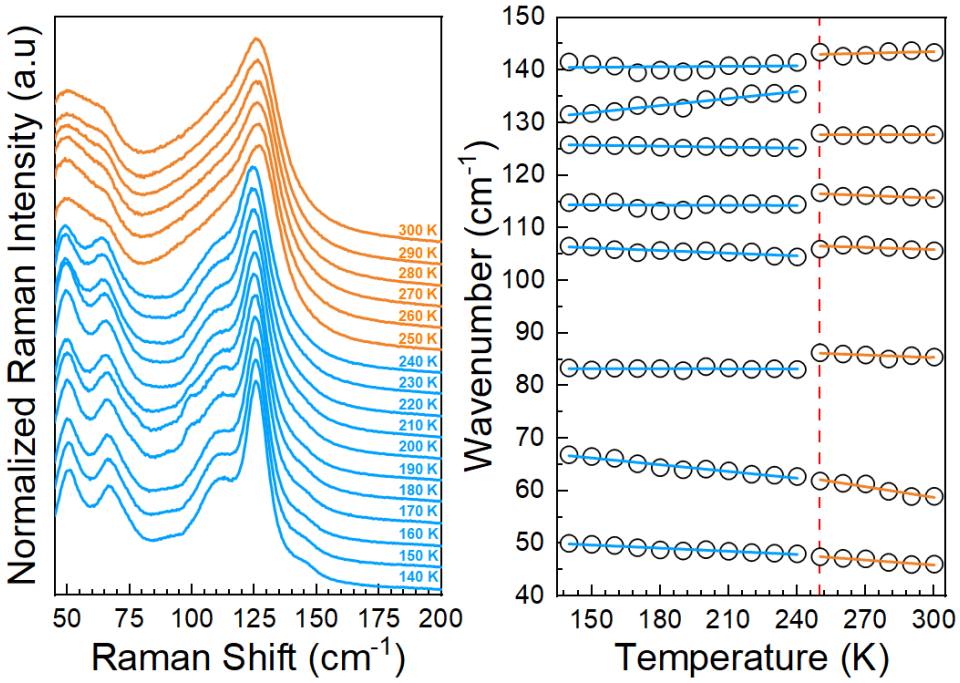

Source: Elaborated by the author.

Figure 22– **Left panel:** Temperature-dependent normalized Raman spectra obtained for the $DMAPbBr_3$ crystal range between 140-300 K in the 200-600 cm^{-1} range, **Right panel:** Temperature-dependent behavior of the mode positions observed in this wavenumber region.

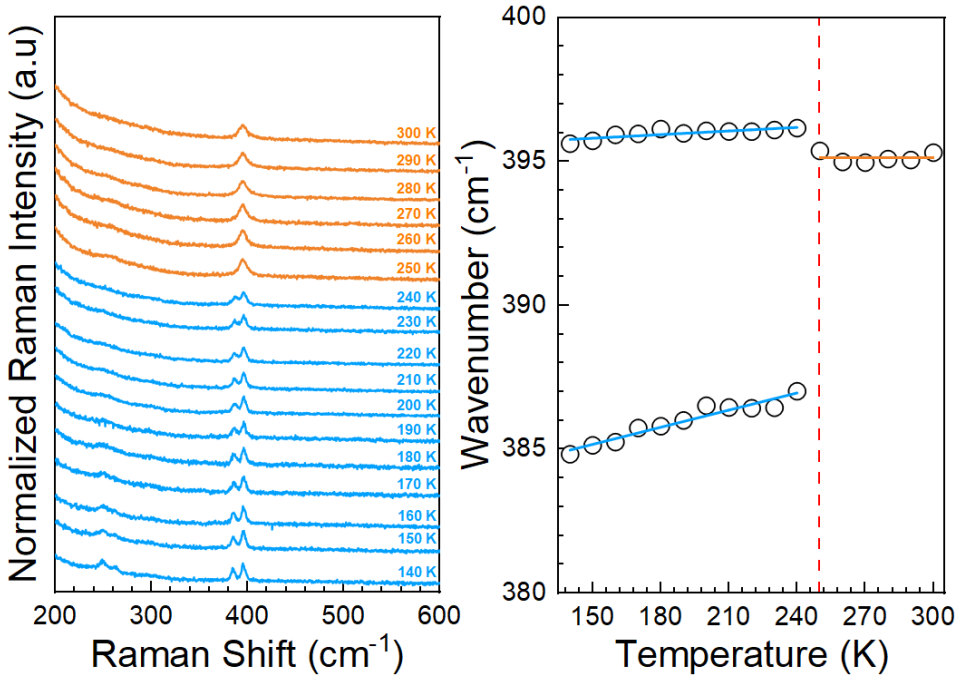

Source: Elaborated by the author.

Figure 22 shows the temperature-dependent behavior of Raman spectra in the range from 200 to 600 cm^{-1}, primarily showing the DMA molecule torsions. This region presents low-intensity modes, with the modes at 250 and 260 cm^{-1} only detected below 170 K. The mode observed in both structural phases at 395 cm^{-1} exhibits anomalous hardening with heating and undergoes a discontinuity in the mode position at T_t =250 K. Additionally, a new band emerges at 385 cm^{-1} after the SPT and presents abnormal hardening. **Figure 23** shows the temperature dependence of the modes observed between 750 and 1100 cm^{-1}. Modifications in the mode positions are observed in these modes, confirming the SPT at 250 K. In particular, the band at ~ 800 cm^{-1}, assigned to ($H_3C–N–CH_3$) bending, exhibits anomalous hardening, followed by a strong discontinuity (~ 8 cm^{-1}) and sudden broadening of the full width at half maximum (FWHM), as shown later. The ($H_3C–N–CH_3$) and NH_2 bending, stretching, and rocking modes are sensitive to the hydrogen bond between the DMA cation and the Pb-Br framework. Therefore, they are suitable probes for this coupling interaction (El-Mellouhi *et al.*, 2016; Grechko *et al.*, 2018; Kieslich *et al.*, 2018; Svane *et al.*, 2017).

Figure 23 – **Left panel:** Temperature-dependent normalized Raman spectra obtained for the $DMAPbBr_3$ crystal range between 140-300 K in the 750–1100 cm^{-1} range, **Right panel:** Temperature-dependent behavior of the mode positions observed in this wavenumber region.

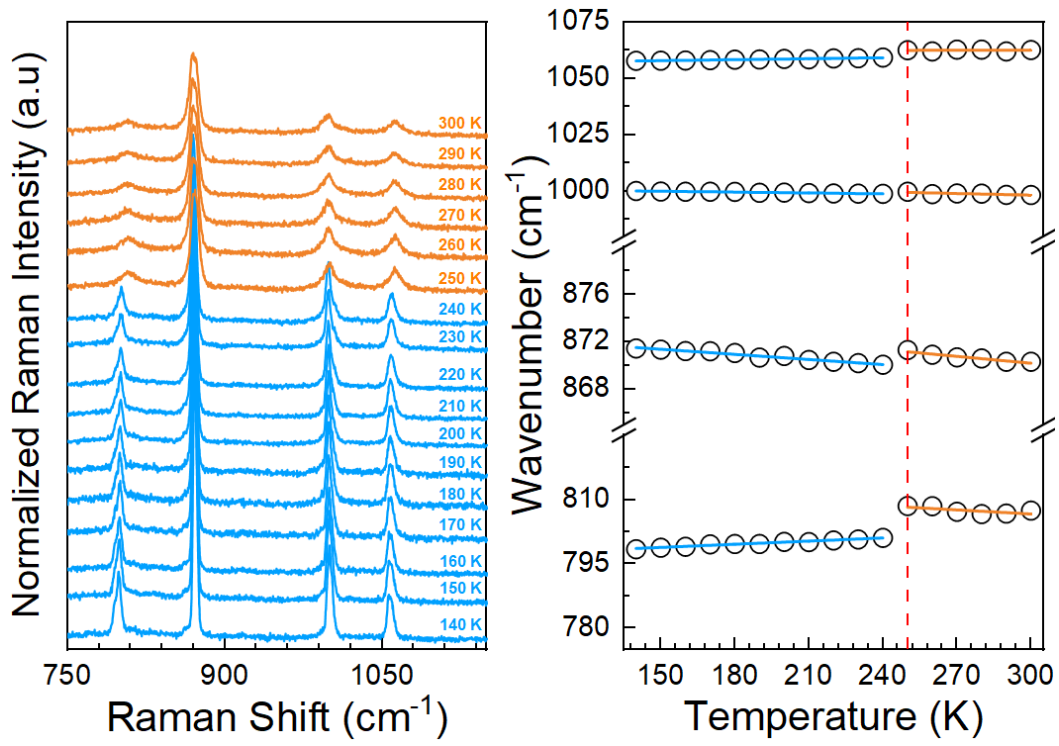

Source: Elaborated by the author.

The CH_3 rocking modes and CH_3 and NH_2 bending of the DMA groups are observed in the wavenumber region between 1200 and 1600 cm^{-1}, which is shown in **Figure 24**. It is interesting to observe that some modes are not very sensitive to SPT. This is not surprising since the main change involving the DMA cations at the transition consists of its freezing into one position under cooling. Nonetheless, the main changes observed in this region are the splitting of the modes at 1339, 1447, and 1563 cm^{-1}, which are assigned to the symmetric bending of CH_3, symmetric bending of NH_2, and antisymmetric bending of NH_2, respectively, and the anomalous hardening (on heating) of the mode at 1553 cm^{-1}, which is observed only in the *LT*-phase, and is assigned as antisymmetric bending of NH_2.

Figure 24 – **Left panel:** Temperature-dependent normalized Raman spectra obtained for the $DMAPbBr_3$ crystal range between 140-300 K in the 1100–1600 cm^{-1} range, **Right panel:** Temperature-dependent behavior of the mode positions observed in this wavenumber region.

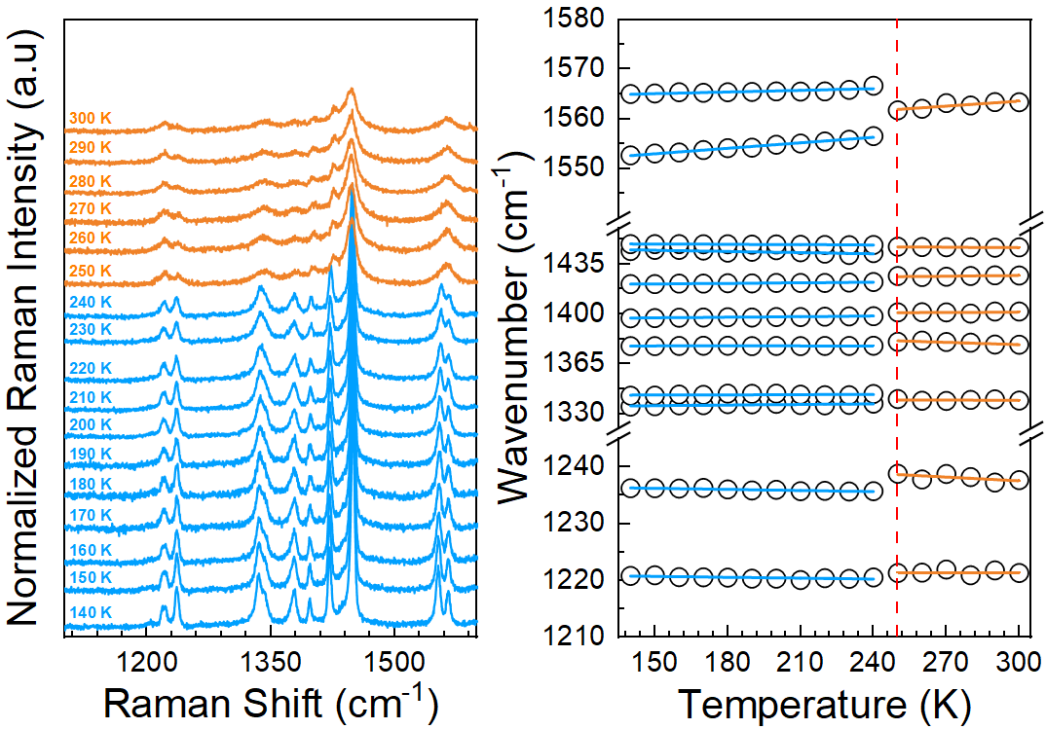

Source: Elaborated by the author.

Figure 25 shows the last wavenumber range (2700–3200 cm^{-1}) of the measured Raman spectra, which relates to the CH_3 and NH_2 stretching modes. Notably, some of the previous observations are highlighted in this region. First, significant changes in the modes at 2849, 2900, 2950, and 3017 cm^{-1} clearly show the SPT. Second, a new mode at 2923 cm^{-1} in the *LT-phase* is observed, exhibiting a standard softening on heating. It was observed four NH_2 stretching modes in the spectra, which are highly associated with the H-bond coupling. Usually,

these modes shift toward lower wavenumbers (Arunan *et al.*, 2011; Arunan e Mani, 2015; Bordallo *et al.*, 2007; Haughey e Beveridge, 1969). *H*-bond formation in the structure affects the N–H stretching vibrations. Usually, when no *H*-bonds are formed, such modes are observed for wavenumbers higher than 3300 cm^{-1} (Haughey e Beveridge, 1969). However, in the presence of H-bonds, such stretching modes shift toward lower wavenumbers (Arunan *et al.*, 2011; Arunan e Mani, 2015; Bordallo *et al.*, 2007). However, in the presence of *H*-bonds, such stretching modes shift toward lower wavenumbers. As we can see, the NH_2 stretching modes observed here were up to 3173 cm^{-1}, which suggests the presence of *H*-bonds in the structure. Another significant point is the hardening of the NH_2 stretching modes in both phases when the temperature increases. As the temperature increases, the H-bonds become weaker, which leads to a hardening of these modes. Additionally, the broadening of NH_2 bands, including scissoring at 1563 cm^{-1}, suggests that these *H*-bond are dynamically disordered.

Figure 25 – **Left panel:** Temperature-dependent normalized Raman spectra obtained for the $DMAPbBr_3$ crystal range between 140-300 K in the 2700–3200 cm^{-1} range, **Right panel:** Temperature-dependent behavior of the mode positions observed in this wavenumber region.

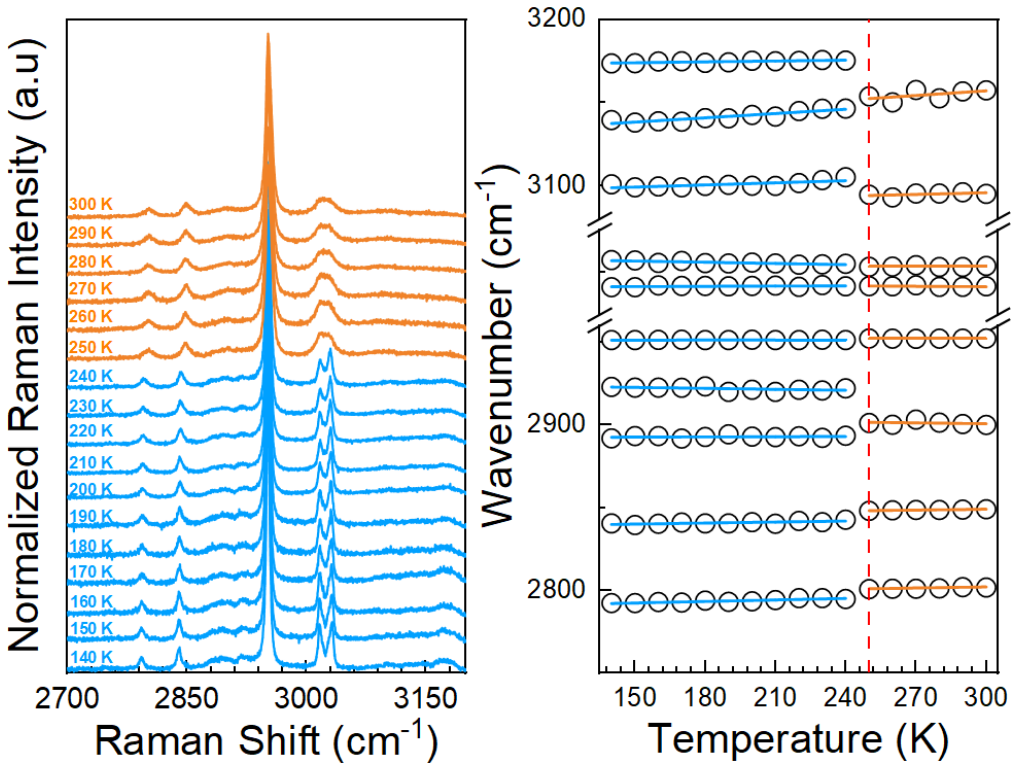

Source: Elaborated by the author.

On the other hand, since the phonon lifetime depends on the structural features, it could be related to the SPT in the $DMAPbBr_3$ perovskite. The common FWHM broadening with increasing temperature relates to anharmonicity and thermally activated reorientation

processes. However, order–disorder phase transitions are usually observed in metal-organic frameworks, and the molecular guest has highly dynamic behavior. Thus, we expect some modes to exhibit significant changes in the FWHM related to SPT at the critical temperature. Additionally, it is interesting that FWHM is sensitive to short- and long-range disorder effects since the internal modes are more dependent on short-range order (Mirosław Mączka *et al.*, 2014; Silva *et al.*, 2020). Indeed, several DMA-related phonons exhibit significant changes in FWHM, as shown in **Figure 26**.

Figure 26 – Temperature-dependent FWHM of selected modes of $DMAPbBr_3$.

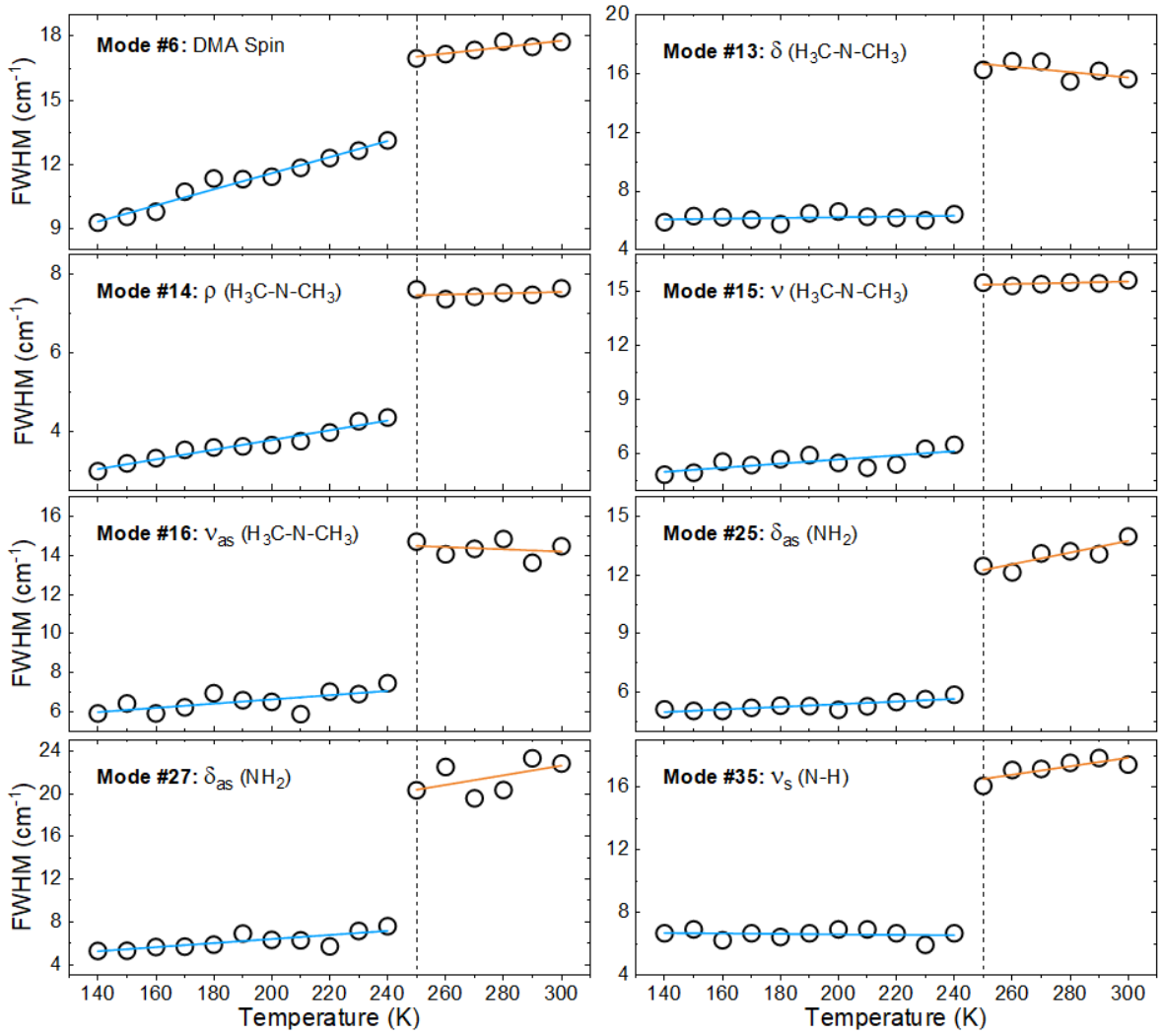

Source: Elaborated by the author.

The FWHM increases around T_t, indicating a short phonon lifetime due to a much less ordered structure at high temperatures. Specifically, the deformation modes of the DMA^+ framework, namely the δ ($H_3C–N–CH_3$), ρ ($H_3C–N–CH_3$) and υ ($H_3C–N–CH_3$) modes exhibit abrupt variations, almost doubling its FWHM. This significant increase in their widths reflects

the statistical disorder of the DMA cations and their hopping motion between different orientations (Schlaak, Couzi e Huong, 1976; Trzebiatowska *et al.*, 2019). Furthermore, as mentioned before, the $H_3C–N–CH_3$ framework and NH_2 modes are expected to be sensitive to H-bonds. As the dynamic disorder of the cations increases, the bandwidths of modes involving vibrations of the NH_2 groups are also expected to increase. This effect is observed in the bending mode δ_{as} (NH_2) and the symmetrical stretching mode υs (N–H), which show variations in their widths of ~12 and ~ 9 cm^{-1}, respectively. The strong increase in FWHM after the SPT reflects the dynamic nature of the HT-phase and provides evidence for ordering *H*-bonds at low temperatures (El-Mellouhi *et al.*, 2016; Mączka, Mirosław *et al.*, 2014; Munson *et al.*, 2018; Rok *et al.*, 2019; Trzebiatowska *et al.*, 2019). This increase also demonstrates a correlation between the strengths of hydrogen bonding, the free motion of the DMA, and the mechanisms of structural order-disorder phase transitions.

Finally, the low-temperature measurements showed the first-order structural phase transition of $DMAPbBr_3$ via an order-disorder mechanism at 250 K. At room temperature, $DMAPbBr_3$ exhibits a complex disordered structure for DMA with space group $P6_3/mmc$, which is frozen at low temperatures. The low-temperature crystalline structure is orthorhombic with space group $P2_12_12_1$. Additionally, the thermal evolution of the crystal structure and lattice dynamics was studied by Raman spectroscopy, which evidenced the order–disorder nature of the transition, probing the presence of an *H*-bond between the DMA cation and the framework. The full width at half maximum (FWHM) of the Raman peaks shows a sharp increase during the phase transition, and the high-temperature phase exhibits broader peaks than the low-temperature phase, which can be attributed to the molecular motions of the DMA cations in the high-temperature phase.

Furthermore, we have observed the weakening of the intermolecular interactions (*H*-bond) upon heating, indicating the correlation with the DMA^+ cation dynamics in the high-temperature phase related to the frameworks. These observations suggest that the dynamics of the DMA cations and the framework are strongly coupled and play a crucial role in the structural phase transition mechanism of $DMAPbBr_3$. The combined powder X-ray diffraction, DSC, and Raman spectroscopy provide a comprehensive understanding of the structural and lattice dynamics of $DMAPbBr_3$. The observed anomalous thermomechanical response and the weakening of intermolecular interactions and molecular motions of DMA cations shed light on the importance of the cation-framework interaction in organic-inorganic hybrid perovskites.

4.3 Low-temperature optical response of $DMAPbI_3$

As discussed in the $DMAPbBr_3$ subsection, the $DMAPbX_3$ (X =Cl, Br, I) *2H*- (for iodide) and *4H*-hexagonal (for chloride and bromide) perovskites exhibit first-order thermally induced crystal structural phase transitions (SPT) at T_t, whereby the low-temperature (*LT*) phase transforms into a high-temperature (*HT*) phase upon heating (García-Fernández *et al.*, 2017, 2019; Rodríguez-Hernández *et al.*, 2022). The *4H*-polytypes are characterized by a 3D framework consisting of $[Pb_2X_9]^5$ units formed by two face-sharing $[PbX_6]^4$ octahedra and bioctahedrons connected by corner-sharing, while the crystal structure of the *2H*-polytype comprises infinite chains of face-sharing $[PbI_6]^4$. In both cases, the DMA cation is located in the cavities or among the chains of the inorganic framework in a disordered position.

The $DMAPbX_3$ compounds with X = Cl or Br as a halide ion exhibit an SPT at T_t (for Cl) at 320 K and a T_t (for Br) at 250 K from an *LT-phase* with orthorhombic symmetry with space group (S.G) $P2_12_12_1$ to an *HT-phase* with hexagonal symmetry S.G: $P6_3/mmc$ (see **Figure 19**) (García-Fernández *et al.*, 2019; Rodríguez-Hernández *et al.*, 2022). Meanwhile, $DMAPbI_3$ undergoes a structural phase transition at T_t = 250 K from monoclinic symmetry with S.G: $P2_1/c$ (*LT-phase*) to hexagonal symmetry with S.G: $P6_3/mmc$ at room temperature (*HT-phase*) (García-Fernández *et al.*, 2017). Remarkably, these three DMA hybrid compounds involve two cooperative processes: a) an order-disorder process involving the DMA cations, whereby in the *LT-Phase,* all DMA atoms occupy a single crystallographic position ordering the molecule above *Tt,* while those atoms occupy higher symmetry sites in the *HT-Phase.* However, the atoms of the organic molecule exhibit a larger orientational degree of freedom and do not occupy the complete crystal site(Shi, Z. *et al.*, 2021); and b) a shift of the Pb^{2+} cations from an off-centered position in the *LT-phase* to a centered one in the *HT-phase*. To validate the successful synthesis of the $DMAPbI_3$ compound, powder x-ray diffraction was performed, and the results were corroborated with those reported by (García-Fernández *et al.*, 2017) ICSD:243860 (see **Figure 27**).

Figure 27 – The $DMAPbI_3$ crystal structure at room-temperature refined by Rietveld with the (ICSD:243860).

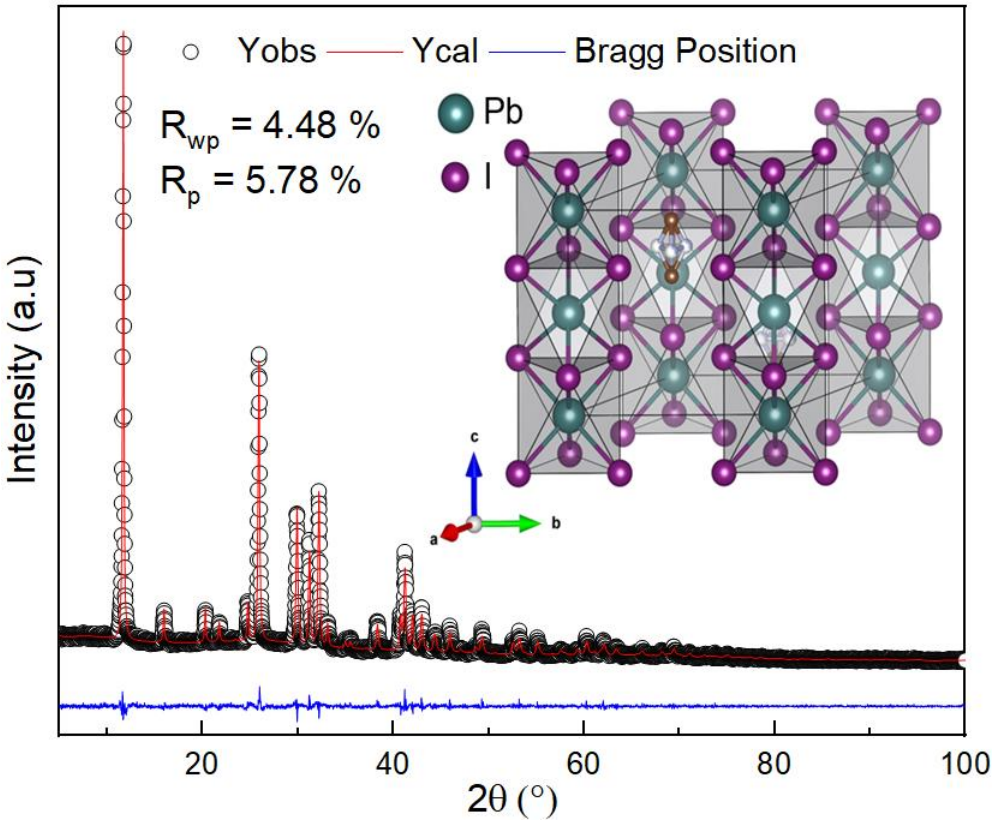

Source: Elaborated by the author.

A sharp dielectric transition occurs in all three hybrid DMAPbX3 hexagonal perovskites associated with the structural phase transition discussed above. The *LT-phase* of the bromide compound exhibits a broad red-light photoluminescence (PL) emission (620 nm) and PL excitation with a maximum at a soft UV wavelength (360 nm). This broadband emission is suggested to be related to the self-trapped exciton mechanism, which may be associated with the particular structural arrangement of the Pb-Br framework, while the significant Stokes shift is connected to the large structural distortion. These features make lead halide hexagonal perovskites promising crystal structures for understanding and designing new hybrid materials with broad photoluminescence emission and dielectric properties (García-Fernández et al., 2017, 2018, 2019). The DMA-based family compound and the $DMAPbI_3$ could offer potential optoelectric applications and properties in extreme conditions. Hence, optical analyses at low-temperature have been provided; two different phenomena were described, i) a thermo-chromic character after *Tt*, whereby the sample loses its characteristic yellow color to become white, and ii) the prohibited electronic states change during the proper modification involving the SPT

in the material to permit a bright red-light low-temperature PL. This subsection details the observed results for the $DMAPbI_3$ compound, highlighting their features.

Methylammonium lead iodide ($MAPbI_3$) is a prototypical hybrid perovskite that undergoes multiple temperature-dependent structural phase transitions. One of the more extensively studied phase transitions is tetragonal ($P4mm$) to cubic ($Pm\bar{3}m$) transition at 327 Kodifies the metal-halide octahedra network (Stoumpos, Malliakas e Kanatzidis, 2013). As a result, the material's optoelectronic and solar cell performance lightly changes upon structural phase transition (Lin *et al.*, 2018). The phase transition features new optoelectronic properties, such as bandgap, photoluminescence, quantum efficiency, and charge carrier mobility (Xu *et al.*, 2021). Induced structural phase transitions could lead to switchable characteristic states with distinctive visible phenomena, making these materials promising candidates for photovoltaic solar cells and smart windows for partial or total color modification as a function of an external condition (Shi *et al.*, 2020; Xue *et al.*, 2018). Previous research has demonstrated that $DMAPbI_3$ undergoes an SPT at Tt = 250 K, with an order-disorder mechanism similar to other DMA-related family compounds. The transition process involves the manifestation and modification of specific orbital interactions between the 6s orbital of $Pb^{2+,}$ which permits the off-center Pb movement in the $[Pb_2X_9]^5$ unit (García-Fernández *et al.*, 2017). Typically, this orbital mixing is low; however, a strong orbital mixing occurs due to the active pair effect, producing electronic states (Brenner *et al.*, 2016). Exceptionally, $DMAPbI_3$ exhibits stronger orbital mixing than $MAPbI_3$, which could potentially show new properties of the sample at low temperatures.

Figure 28 shows images of a high-resolution intensity map scale obtained from $DMAPbI_3$ when excited with white LED light **Figure 28**(a)) and excited with UV 405 nm (**Figure 28** (b)) for selected temperatures, which were obtained by thermomicroscopy. The images show that $DMAPbI_3$ exhibits two distinct phenomena associated with the SPT at *Tt.* Such events occur after the complete transformation of the phase, as shown in the cooling cycle in the DSC measurement (**Figure 28** (c)). First, when irradiated with white light, the crystal exhibits a thermochromic effect, where the characteristic yellow color of the sample becomes white (**Figure 28** (a)). Also, when irradiated with UV light, it shows an orange-red PL emission appearance (**Figure 28** (b)).

Figure 28 – High-resolution intensity maps of $DMAPbI_3$ showing **(a)** the thermo-chromic effects and **(b)** the light orange-red photoluminescence after the structural phase transition, accompanied by **(c)** the cooling DSC process. The orange dashed bar separates the two phases, and the linear guides (blue and green) the eyes, indicating the trend modification of both curves around *Tt*.

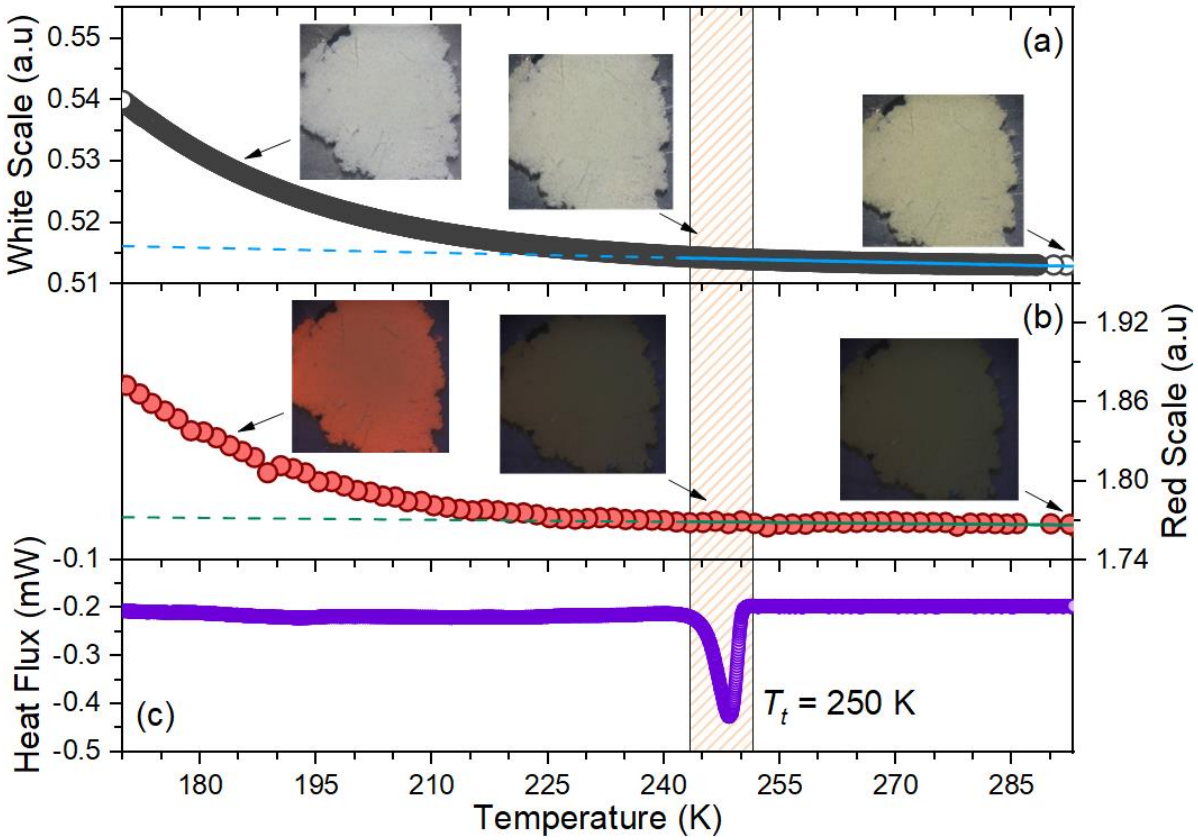

Source: Elaborated by the author.

Both optical phenomena, thermochromic and photoluminescence, are reversible and depend on temperature. Interestingly, the intensity of both phenomena increases as the temperature decreases, similar to the behavior observed in $MAPbI_3$. It was suggested that thermochromism in $MAPbI_3$ is due to a reversible hydration/dehydration process induced by the SPT is responsible for thermochromism. Moisture ingress causes the lattice to relax to its initial phase, resulting in a return to the original sample color (Lin *et al.*, 2018).

The low-temperature photoluminescence phenomenon observed in $DMAPbI_3$ has been attributed to the presence of self-trapped excitons (STEs) produced by photogenerated holes resulting from the SPT mechanism (Liu, S. *et al.*, 2021; Roy *et al.*, 2021). The difference in photoluminescence between the high-temperature and low-temperature phases can be reasonably explained by considering the thermal lattice and interaction between electrons and phonons (Han *et al.*, 2022). At high temperatures, both processes are maximized, leading to a

non-radiative emission path. However, at low temperatures, the lattice relaxation facilitates the conditions for producing electron-hole pairs, generating STEs states with radiative emissions equivalent to the observed photoluminescence.

It is important to note that a thorough understanding of the underlying mechanisms that govern these phenomena is crucial for optimizing $DMAPbI_3$-based devices. In this context, a deeper understanding of the low-temperature photoluminescence of the sample is essential for developing advanced and efficient optoelectronic devices. Thus, let us discuss the mechanisms that govern the photoluminescence origin of $DMAPbI_3$ at low temperatures. The crystal structure of $DMAPbI_3$ can be described as a one-dimensional (1D) infinite chains of octahedra and bioctahedra connected by corner-sharing along the *c*-axis, which classifies the compound as low-dimensional hybrid halide perovskites (HHPs). Such low-dimensional HHPs materials usually exhibit typical luminescent properties of large Stokes shift and broadband emissions (Mao, Stoumpos e Kanatzidis, 2019). The presence of vacancies in the sample via structural disorder facilitates optical excitation, typically attributed to recombining STEs. The formation of STEs is due to the strong electron-phonon coupling present in distortional lattices, which generally generates small polarons binding the excitons under excitation (Ghosh e Spano, 2020; Han, Cheng e Cui, 2022). Photoluminescence spectroscopy shows that the PL spectra are highly susceptible to distortions in the material, as well as to the electronic-charge carrier, resulting in modifications of the energy emission, intensity, and full width at half maximum (FWHM) of the broadband, which could be directly related to a significant dependency of STEs emissions with structural distortions.

It has been observed that low-dimensional perovskite-type configurations materials having distorted octahedra (intrinsically exhibiting electron-phonon interaction) have a higher probability of producing STEs emissions. Furthermore, in some cases, these states can only be accessed with external conditions that help relax the crystal structure, thereby increasing the STEs states contribution (Li *et al.*, 2020; Zhang *et al.*, 2021) or by undergoing a structural phase transition, which modifies the arrangement of the crystal structure (Shi *et al.*, 2019; Shi, Y. *et al.*, 2021). It is noteworthy that $DMAPbI_3$, as previously described, exhibits an SPT involving the order-disorder mechanism related to an off-center Pb^{+2} distortion in the octahedra and an indirect bandgap (García-Fernández *et al.*, 2017). This unique behavior of $DMAPbI_3$ provides an opportunity to investigate the underlying mechanisms governing the STEs emission in the sample and the effect of structural distortion on photoluminescence properties.

The $DMAPbI_3$ exhibits a continuous strong red bright broad emission centered at 680 nm, equivalent to 1.82 eV at the *LT-phase*, similar to $DMAPbBr_3$, which is attributed to a STE

mechanism too (García-Fernández *et al.*, 2017). **Figure 29** (a) shows the PL measurements at low temperatures of $DMAPbI_3$. Observe that when the temperature decreases, the intensity of the PL spectra emission increases. It is important to highlight that the compound exhibited a double self-trapped exciton (STEs) emission band at 110 K, which increased to a triple-emission band at 70 K. The thermal expansion coefficient and the vibration lattice cover these emissions at high temperatures (Dar *et al.*, 2016).

Accordingly, STEs are a band-to-band luminescence, indicating that electrons in the conduction band recombine with holes in the valence band, and the recombination process emits a phonon by a defect (Li *et al.*, 2019; Shi, Y. *et al.*, 2021). Thus, once electrons and holes are photogenerated, these excitons are self-trapped instantly because these self-trapped states are accessible and more stable in the presence of lattice distortion.

The strength of electron-phonon can be evaluated by the Huang-Rhys factor $S = \Delta E/\hbar\omega$, which is the number of phonons emitted after the carrier capture (Whalley *et al.*, 2021). **Figure 29** (b)–(d) describes the separated Pearson contributions related to each PL band present in $DMAPbI_3$ denominated as PL-$Bn_{i\ (i=1,2,3)}$. The increase and presence of STEs bands modify the color emission from light orange-red to strong bright red at low temperatures. **Figure 29** (e) describes the center peak temperature dependence on all displayed bands. As a band-to-band nature PL, all the STEs recombinations processes could be explained and fitted by the following equation:

$$E(\mathrm{T}) = E_0 + A_{TE}T + A_{EP}\left[\frac{2}{e^{\frac{\hbar\omega}{k_bT}} - 1} + 1\right] \tag{11}$$

where the $E(\mathrm{T})$ is the unnormalized bandgap at $T = 0$ (E_0), A_{TE} is the weight of the thermal expansion, A_{EP} is the electron-phonon energy interaction, and $\hbar\omega$ is the average optical phonon energy. The A_{EP} in equation (11) is analogous to ΔE for the Huang-Rhys factor (*S*), which indicates the electron-phonon coupling strength. **Table 5** summarizes the adjusted parameters for (11) and the Huang-Rhys factor for each STEs PL-$Bn_{i\ (i=1,2,3)}$.

Figure 29 – **(a)** Temperature-dependence PL spectra of $DMAPbI_3$, obtained by exciting the sample with 405 nm light. The Pearson function decomposition of the spectrum exhibiting the self-trapped exciton (STEs) contribution states, refers as $PL\text{-}Bn_{i\ i=1,2,3}$ (Photoluminesce Band) at **(b)** 10K, **(c)** 70K and **(d)** 140 K, in which each temperature enables the contribution to the color coding. **(e)** The low-temperature dependence of peak centers for each STEs $PL\text{-}Bn_{i\ (i=1,2,3)}$, where the data fits the equation (11).

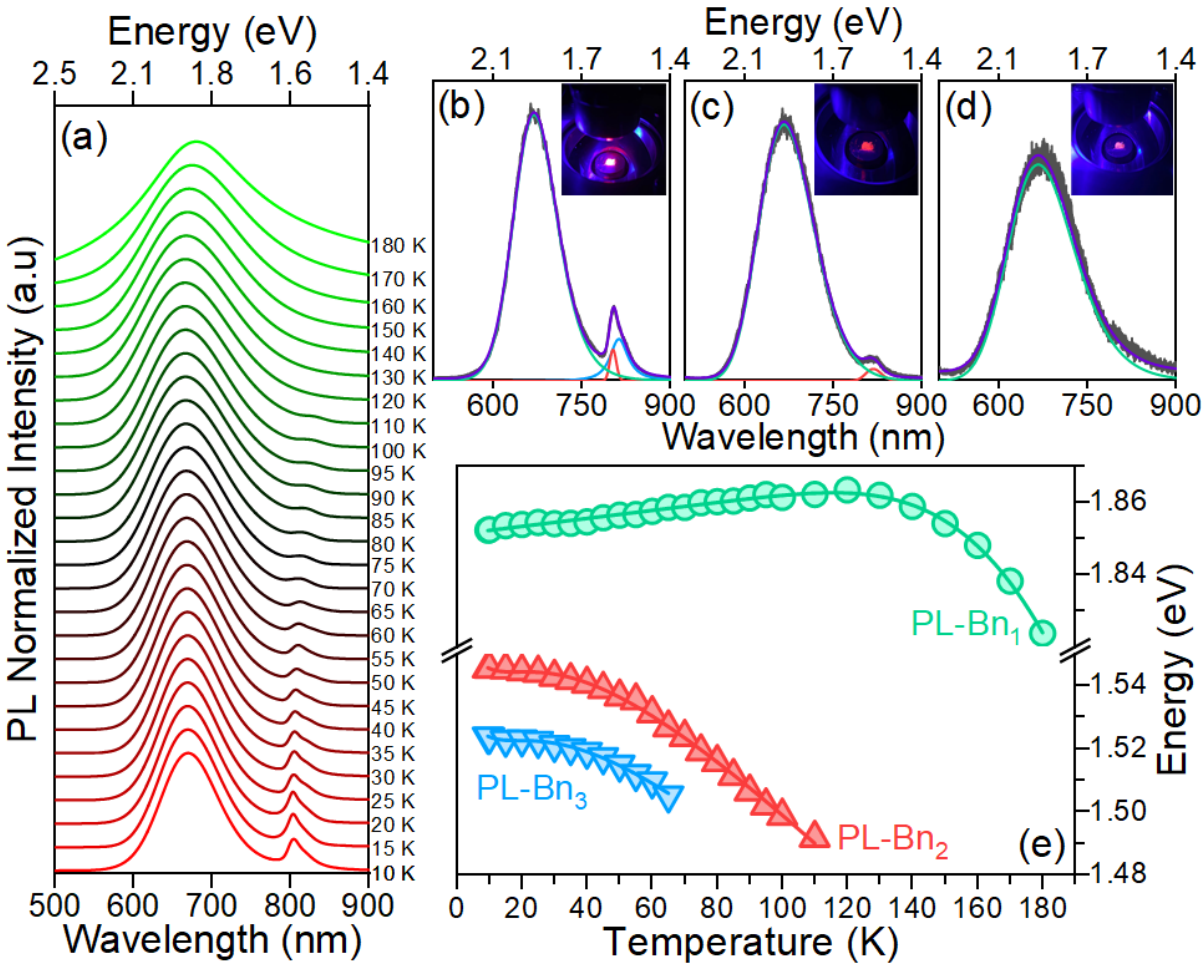

Source: Elaborated by the author.

Table 5 – Fitted values of the adjustments for the PL Center parameters with the equation (11), where k_b is the Boltzmann constant ($8.617\ x10^{-5}$ eV/K).

STEs Contribution	$E_{g\ (T=0K)}$ (eV)	A_{TE} (meV.K^{-1})	A_{EP} (eV)	$\hbar\omega$ (meV)	S
$PL\text{-}Bn_1$	7.6 ± 0.9	0.111 ± 0.003	5.7 ± 0.9	100 ± 3	57
$PL\text{-}Bn_2$	1.5401 ± 0.0008	1.08 ± 0.04	0.014 ± 0.009	173 ± 11	0.08
$PL\text{-}Bn_3$	1.5195 ± 0.0009	1.00 ±0.09	0.013 ± 0.002	3.3 ± 0.2	3.93

Source: Elaborated by the author.

The intensity increasing and presence of STEs bands in $DMAPbI_3$ have important implications for optoelectronic applications as they modify the color emission and provide insight into the electron-phonon coupling strength of the material. The model described in (11) is used to understand the majority of contributions of the photoluminescence temperature dependence. The values in **Table 5** show that electron-phonon coupling has a more significant effect than the thermal expansion effect. The Huang-Rhys factor (S), which measures the strength of electron-phonon coupling, is a figure of merit for evaluating and optimizing the STEs emission regime and establishing the carrier trapping process in soft semiconductors (Usually, $S \gg 1$ for a strong coupling regime). In $DMAPbI_3$, the values of $S \sim 60$ indicate a strong electron-phonon coupling regime, similar to other halide perovskites such as the inorganics $CsPbBr_3$ ($S = 12$) (Pan *et al.*, 2022), $Cs_3Sb_2I_9$ ($S = 42.7$), $Rb_3Sb_2I_9$ ($S = 50.4$), $Cs_3Bi_2I_9$ ($S = 79.5$)(McCall *et al.*, 2017), and similar to 1D hybrids perovskites as $C_5H_{16}N_2Pb_2Br_6$ ($S = 54$), $[C_6H_7ClN]CdCl_3$ ($S = 62.94$) (Xu *et al.*, 2022), and $[C_7H_{10}N]_3[BiCl_5]Cl$ ($S = 45$) (Klement *et al.*, 2021).

The accessible self-trapped excitons in high temperatures present a non-radiative recombination rate, which is unfavorable for the efficient emission of STEs at room temperature. However, at low temperatures, the $DMAPbI_3$ compensated by the structural phase transition, the dynamics of inorganic off-center displacement of the Pb^{+2} ion is prone to SPT, producing the distortions surrounding the octahedra. These distortions are followed by electron capture, indicating the involvement of electron-phonon coupling and the production of excitons from self-trapping origins on the photoluminescence PL-$Bn_{i\ (i=1,2,3)}$ bands.

To investigate the potential applications of intense red light-emitting diodes (LEDs), the effect of spectral power distribution was evaluated by CIE 1931 color space curve, which describes the (*x,y*) chromaticity coordinates (Zhu *et al.*, 2019). The chromaticity coordinates of $DMAPbI_3$ in the CIE-1931 color space as a function of temperature is presented in **Figure 30**, with the corresponding values given in **Table 6**. As shown, there is a distinct color transition from red-orange at 180 K to intense bright red at low temperatures, as depicted in **Figure 29** (b)-(d).

Figure 30 – CIE-1931 color space with the temperature-dependent chromaticity coordinates of PL emissions of $DMAPbI_3$ (Blue dots).

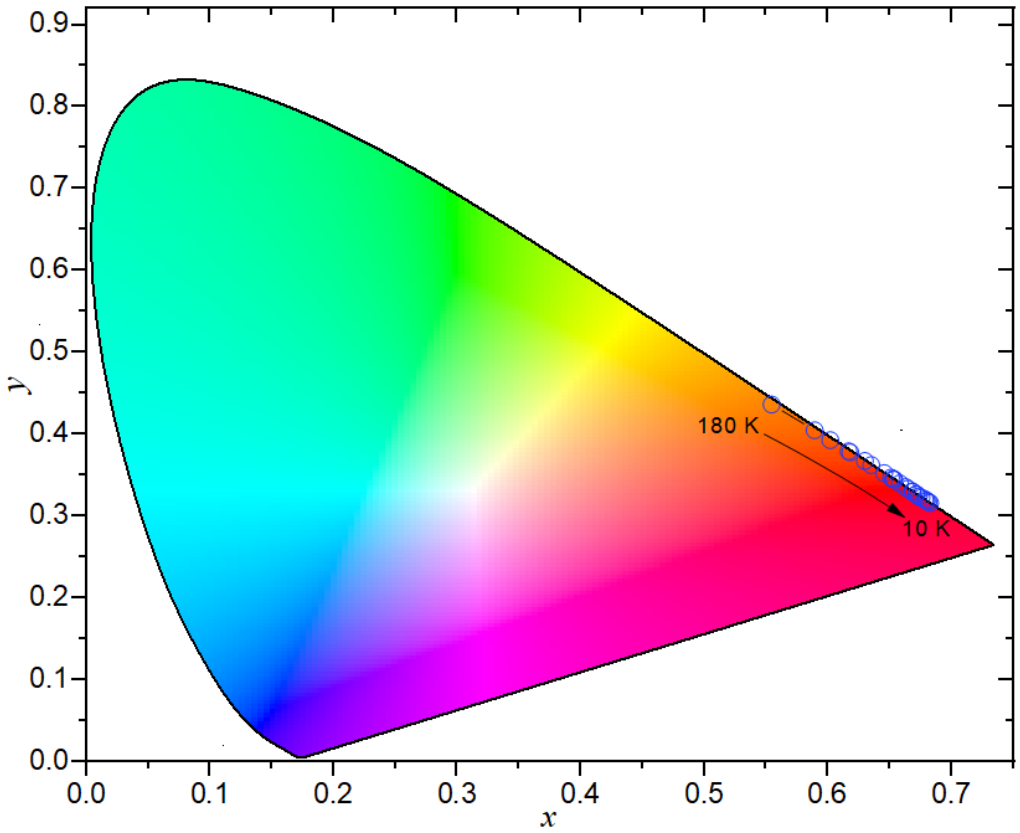

Source: Elaborated by the author.

The observed changes in color and brightness of $DMAPbI_3$ are attributed to the appearance of the novel self-trapped exciton (STEs) PL-Bn_2 at 110 K and PL-Bn_3 at 70 K contributions in the photoluminescence spectra. These contributions modify the intensity of the emitted light and result in different chromaticity coordinates. This behavior is consistent with the previous discussion on the significant dependency on STEs and highlights the importance of understanding their role in determining the luminescent properties of low-dimensional hybrid halide perovskites. It is worth noting that the novel STEs contributions detected at low temperatures are indicative of the relaxation of the crystal structure, which enables the appearance of previously inaccessible states. Identifying these novel STEs contributions provides valuable insights into the luminescent properties of low-dimensional hybrid halide perovskites and their potential applications in optoelectronics. Moreover, the observed color transition in $DMAPbI_3$ highlights the tunability of the optical properties of these materials at low temperatures, paving the way for the development of novel light-emitting devices.

Table 6 – Temperature-dependent chromaticity coordinates of $DMAPbI_3$.

Temperature (K)	CIE *x*	CIE *y*	Temperature (K)	CIE *x*	CIE *y*	Temperature (K)	CIE *x*	CIE *y*
180	0.55457	0.43658	95	0.65118	0.34734	50	0.67846	0.32089
170	0.58936	0.40509	90	0.65281	0.34589	45	0.68024	0.31908
160	0.60211	0.3931	85	0.6539	0.34483	40	0.68155	0.31772
150	0.61691	0.37965	80	0.65831	0.34032	35	0.68286	0.3165
140	0.61814	0.37828	75	0.66308	0.33584	30	0.6828	0.31655
130	0.62997	0.36771	70	0.66492	0.3339	25	0.6798	0.31928
120	0.63516	0.3628	65	0.66827	0.33069	20	0.67583	0.32288
110	0.64567	0.35298	60	0.66854	0.33016	15	0.67373	0.32436
100	0.65348	0.34532	55	0.67178	0.32696	10	0.67151	0.32706

Source: Elaborated by the author.

The investigation of $DMAPbI_3$ at low- has provided valuable insights into the thermo-chromatic and luminescent properties of low-dimensional hybrid halide perovskites. The structural phase transition of the sample, which presents an order-disorder mechanism, permits the appearance of novel self-trapped exciton (STEs) contributions in the photoluminescence spectra at *Tt*. These novel contributions modify the intensity of the emitted light and result in different chromaticity coordinates. The observed changes in color and brightness are attributed to the relaxation of the crystal structure, which enables the appearance of previously inaccessible states. The significant dependency on STEs has been discussed, and the values displayed in **Table 5** confirm the electron-phonon coupling to be the dominant contribution to the photoluminescence temperature dependence. This study deepens our understanding of the electron-phonon coupling strength in $DMAPbI_3$, an important factor in designing optoelectronic devices. The observed electron-phonon coupling at low temperatures is consistent with other hybrid perovskites, and the color transition in $DMAPbI_3$ highlights the tunability of its optical properties. The ability to tune the color emission in $DMAPbI_3$ at low temperatures is due to changes in energy level structure and crystal structure relaxation, which could be used to develop efficient red-light emitting devices and smart windows. The promising feature of this color transition from red-orange to intense bright red at low temperatures is presented in **Figure 30**.

5 THE $CsCuCl_3$ LIKE-PEROVSKITE COMPOUND UNDER EXTREME CONDITIONS

The $CsCuX_3$ family is a group of total inorganic-metal halide perovskite-like compounds with a general chemical formula of AB_yX_z, where A = Rb, or Cs; B = Mn, Fe, Co, Ni, or Cu; and X = Cl, Br, or I. These materials have attracted significant attention due to their potential applications in optoelectronics, catalysis, and energy storage (Cao e Li, 2021; Lu *et al.*, 2021; Roccanova *et al.*, 2019; Zhang *et al.*, 2022). $CsCuX_3$ compounds possess optical and electronic properties similar to their Pb-based counterparts but offer advantages such as greater stability and reduced toxicity compared to lead halides. Therefore, there has been interest in partially or completely substituting Cu^+ as a potential replacement (Bechir e Dhaou, 2021; Wu *et al.*, 2021; Zheng *et al.*, 2020). This chapter investigates the $CsCuCl_3$ perovskite-like compound at low temperatures and high pressure to provide a structural-property analysis for its potential applications.

5.1 Introduction

Typically, halide perovskites with the general formula ABX_3 and a transition metal ion B crystallize in derivatives of the hexagonal perovskite structure, which can give rise to the Ruddlesden-Popper and Dion Jacobsen series of materials, as well as quasi-1D and full 1D (one-dimensional) like-perovskite compounds (Fop *et al.*, 2019; Nguyen e Cava, 2021). From a symmetry perspective, the intrinsic *3*- or *6*-fold rotational symmetries frustrate the ordering of magnetic moments or orbital occupancies of the framework ions into a single lowest-energy state at low temperatures, making them promising candidates for the quantum spin-liquid state (Balents, 2010).

Among the $CsCuX_3$ family, the $CsCuCl_3$ is a like-perovskite material with Cu^{2+} (S = 1/2) spins with antiferromagnetic order below T_N = 10.7 K (Collocott e Rayne, 1987; Miyake *et al.*, 2015; Ueda *et al.*, 2022). The antiferromagnetic (AFM) effect in the sample is produced by the exchange interaction within the intrachain and the antisymmetric exchange (Dzyaloshinskii-Moriya) interaction, allowed by the twist of 120° in the AFM phases along the [001] direction (Plakhty *et al.*, 2009). At room temperature, the compound possesses a polytype distorted hexagonal perovskite structure belonging to chiral space groups $P6_522$ or $P6_122$, which undergoes a structural phase transition at high temperatures (423 K) induced by the Jahn-Teller effect to the space group $P6_3/mmc$ (Kroese e Maaskant, 1974a). The crystal structure of the hexagonal phase $P6_522$ (usually named left-handed for their spin rotation direction) consists

of two face-shared distorted $[CuCl_6]^{4-}$ octahedra forming a $[Cu_2Cl_9]^{5-}$ dimer unit, which displays a 1D chain of dimers along the *c*-axis, with the Cs^+ ion occupying the void space between the chains (Plakhty *et al.*, 2009) (see **Figure 31**). From an optoelectronic perspective, $CsCuCl_3$ exhibits a direct semiconductor profile with a 1.92 eV band gap value and absorption in the near-infrared region but does not display a photoluminescence signal (Cui *et al.*, 2020).

Figure 31 – (a) Crystal structure of $CsCuCl_3$ ($P6_522$) with dimer chains along the *c*-axis, and (b) the left-handed helical with the principal chiral arrangement of Cu^{2+} along the [001] axis. (The blue and red helices are guides for eyes).

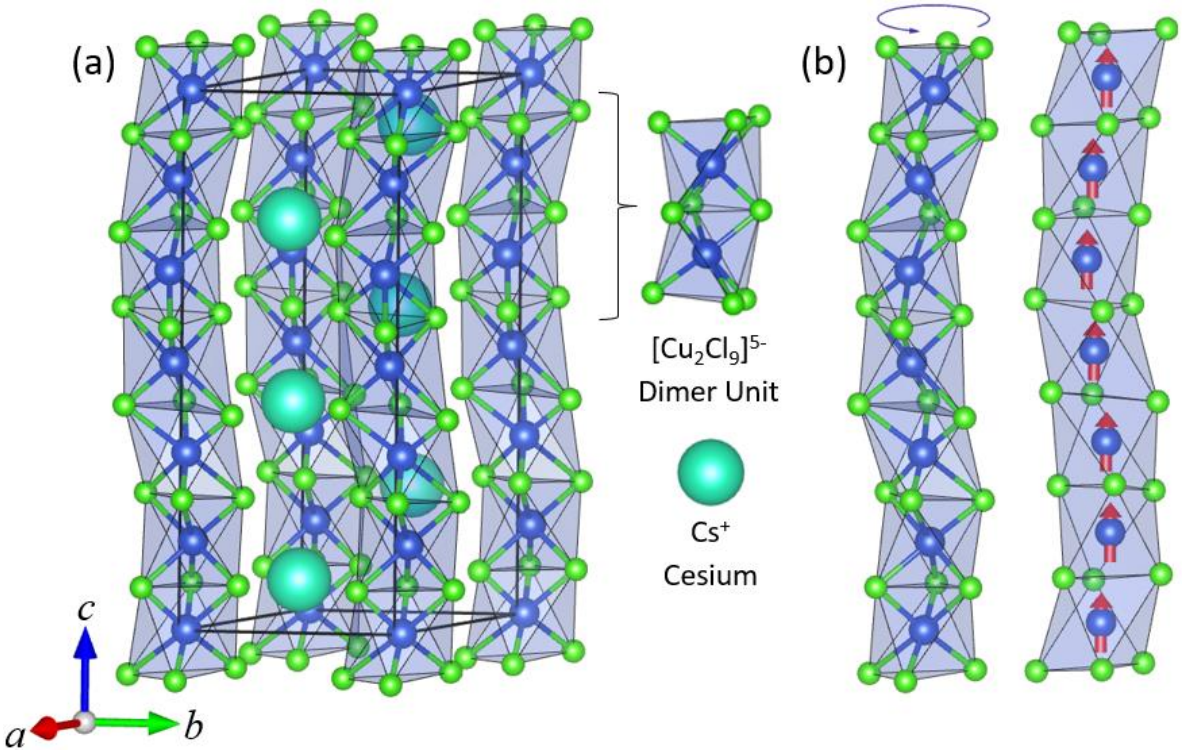

Source: Elaborated by the author.

Frustrated quantum many-body systems, such as $CsCuCl_3$, provide promising examples for investigating the effects of high pressure on competing interactions at low-energy states. The manipulation of external pressure on frustrated quantum materials can provide a means to actively modulate the amount of quantum correlations across the classical and quantum-mechanical regimes, enabling the exploration of exotic phenomena emerging in the crossover between these two regimes (Nihongi *et al.*, 2022). The magnetic diagram of $CsCuCl_3$ at low temperatures, as a function of the longitudinal magnetic field ($\boldsymbol{H} \parallel c$), exhibits a quantum-phase transition ($\boldsymbol{H}$ =12.5 T) from an umbrella phase to a *2-1* coplanar phase as the magnetic field increases. Similarly, under pressure effects, the incommensurate (IC) wavenumber increases with the magnetic field and pressure, which enhances the neighboring spins in the

sample and modifies the magnetic diagram by the enhanced Dzyaloshinskii-Moriya interaction (Hosoi, Matsuura e Ogata, 2018; Sera *et al.*, 2017). Consequently, pressure-induced new quantum phases are observed, which can be distinguished by the ICN notation (with N from 1 to 5 for each phase), advancing the scientific concept of controlling quantum mechanical correlations in weakly-coupled spin chain materials through the application of external pressure in $CsCuCl_3$ (Yamamoto *et al.*, 2021).

Although different authors have studied $CsCuCl_3$, the compound offers potential applications in data storage and memory, particularly in controlling the ICN quantum phases, which could aid in understanding these exotic states under external conditions. Raman spectroscopy at low temperatures and high pressure provides insights into the structural changes occurring in $CsCuCl_3$, making it a valuable technique for studying this material.

5.2 Raman spectroscopy at low-temperatures in $CsCuCl_3$ – Spin-phonon coupling

The coupling between spin, charge, lattice, and orbital is fundamental in condensed matter physics, giving rise to emergent phenomena and applications, such as multiferroics and spintronics (Liu, Y. *et al.*, 2021). Recently, there has been growing interest in spin-phonon coupling (SPC) in materials, which simultaneously controls magnetic and phononic properties (Qin *et al.*, 2020; Zhang *et al.*, 2019). Magnetic states can be stabilized by modifying epitaxial strains or by displacing magnetic ions in the sample through external conditions such as high magnetic fields, high pressure, or low temperatures. The Hamiltonian describing spin-related phenomena in solids can be written as a sum of isotropic exchange (IE), the Dzyaloshinskii-Moriya (DM), the anisotropic exchange (AE), and the single-ion anisotropy (SIA) interactions (Pesin e Balents, 2010; Sohn *et al.*, 2017), given by:

$$H_{spin} = \sum_{ij}^{nn} [J_{IE}(\boldsymbol{S}_i \cdot \boldsymbol{S}_j) + \boldsymbol{D}_{ij} \cdot (\boldsymbol{S}_i \times \boldsymbol{S}_j) + \boldsymbol{S}_i \cdot \boldsymbol{\Gamma}_{ij} \cdot \boldsymbol{S}_j] + A \sum_i (\mathbf{n}_i \cdot \boldsymbol{S}_i)^2 \qquad (12)$$

where J_{IE}, $\boldsymbol{D}_{ij}$, $\boldsymbol{\Gamma}_{ij}$, and A are the coefficients IE, DM, AE, and SIA interactions, respectively, while $\mathbf{n}_i$ is the vector direction axis, and $\boldsymbol{S}_i$, $\boldsymbol{S}_j$ are the neighboring spins in the i and j sites. Around the terms described in (12), the interactions of the spins are highly dependent on Coulomb interactions, but J_{IE}, $\boldsymbol{D}_{ij}$, $\boldsymbol{\Gamma}_{ij}$, and A are terms that dynamically modify by the lattice vibration, resulting in some cases in an SPC, which is observed as a renormalization of phonon frequencies (Son *et al.*, 2019).

As was previously described, the $CsCuCl_3$ exhibits an antiferromagnetic ordering at T_N = 10.7 K produced by DM interaction, which is allowed by the twist of the $[Cu_2Cl_9]^{5-}$ dimer unit along the [001] direction. This magnetic ordering can induce a SPC in $CsCuCl_3$. To investigate such coupling, we performed temperature-dependent Raman spectroscopy at low temperatures. The crystal structure at room-temperature of $CsCuCl_3$ (SG: $P6_522$) was verified using Single Crystal X-Ray Diffraction (SCXRD), which was consistent with the hexagonal $P6_522$ reported by Chen *et al*. (Cui *et al.*, 2020) (ICSD: 120370). The group-theory analysis of the $P6_522$ symmetry for $CsCuCl_3$ yields 35 Raman-active phonon modes, represented by $\Gamma_{raman}=6A_1\oplus15E_2\oplus14E_1$ for the point group D_6 (see **Table 7**).

Table 7 – Group factor analysis of the $CsCuCl_3$ crystal structure at room pressure (space group $P6_522$ (179))

$P6_522$ (179)			
Atoms	**Wyckoff notation**	**Site symmetry**	**Irreducible representation**
Cs_{01}	*6b*	C_2'	$A_1\oplus2A_2\oplus2B_1\oplus1B_2\oplus3E_1\oplus3E_2$
Cu_{01}	*6a*	C_2	$A_1\oplus2A_2\oplus B_1\oplus2B_2\oplus3E_1\oplus3E_2$
Cl_{01}	*12c*	C_1	$3A_1\oplus3A_2\oplus3B_1\oplus3B_2\oplus6E_1\oplus6E_2$
Cl_{02}	*6b*	C_2'	$A_1\oplus2A_2\oplus2B_1\oplus1B_2\oplus3E_1\oplus3E_2$
	Total	D_6	$6A_1\oplus9A_2\oplus8B_1\oplus7B_2\oplus15E_1\oplus15E_2$
Modes Classifications			
			$\Gamma_{raman}=6A_1\oplus15E_2\oplus14E_1$
			$\Gamma_{IR}= 8A_2\oplus14E_1$
			$\Gamma_{acoustic}= A_2\oplus E_1$
			$\Gamma_{silent}=7B_2$

Source: Elaborated by the author.

Figure 32 shows the high-resolution Raman spectrum in the 100-320 cm^{-1} range for the $CsCuCl_3$ powder sample at 9.2 K and 300 K did now present any structural phase transition. As the temperature decreases, the crystal lattice relaxes, leading to an increase in the intensity of the Raman peaks and the number of displayed phonons (from 8 at room-temperatures to 15 at low-temperatures). The bands become sharper, better defined, and shifted, the Raman assignment was based on the stable lattice dynamics calculated around the Γ-point using Differential Functional Perturbation Theory (DFPT). The DFPT calculations relax the crystallographic cell size and shape by minimizing all quantum forces in the static lattice, which approximates the crystal structure to T = 0 K.

Figure 32 – High-resolution Raman spectra of $CsCuCl_3$ at 300 K and 9.2 K. (The blue and red curves represent the Lorentzian oscillator phonons bands and the total modes convolution, respectively).

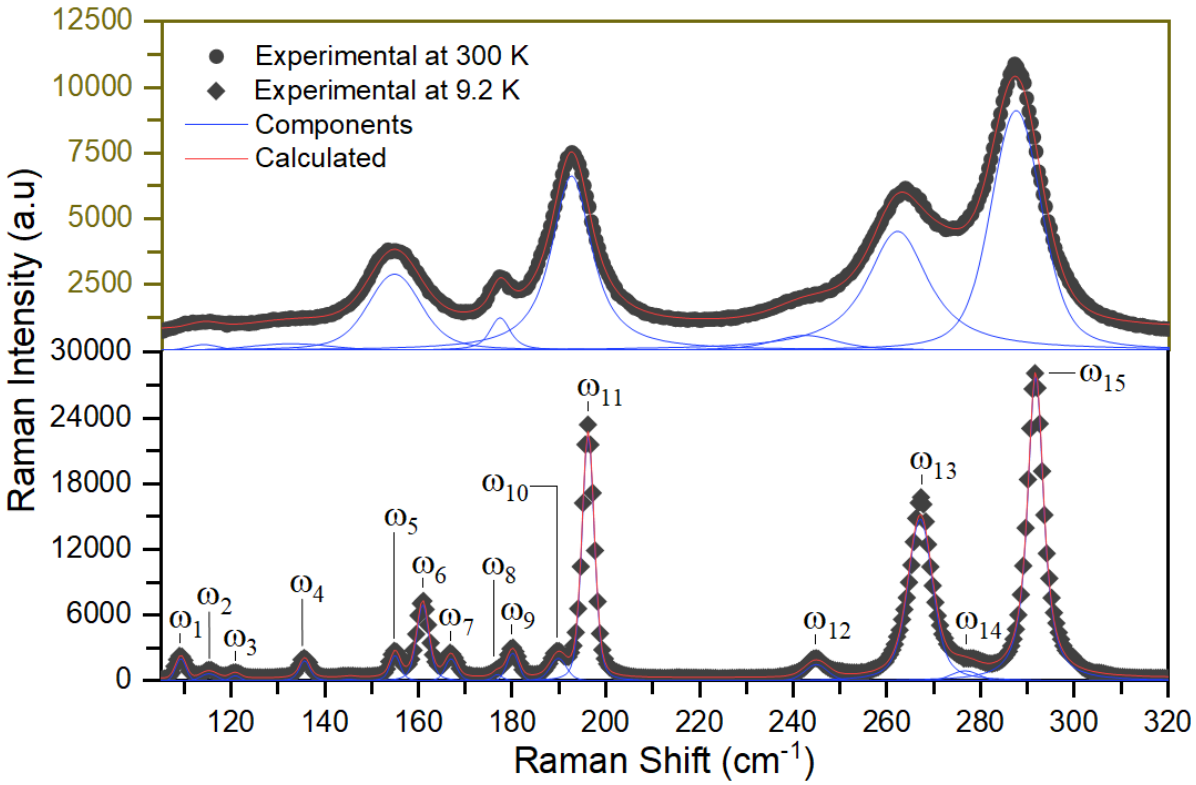

Source: Elaborated by the author.

Table 8 summarizes the experimental Raman frequencies (300 K and 9.2 K) and the DFPT-calculated phonons, which were compared with previous Raman or IR measurements of similar materials such as $ABCl_3$ (A=Cs, Rb; B=Mn, Co) (G. Mattney Cole, Jr. Charles F. Putnik e Smith L. Holt, 1975; Kambli e Giidel, 1984; Petzelt *et al.*, 1981), $CsBBr_3$ (B=Co, Mg, Cd)(C. W. Tomblin, G. D. Jones e R. W. G. Syme, 1984), and Cs_2XCl_4 (X=Cu, Co) (Jara *et al.*, 2019; Nataf *et al.*, 2017), $[(CH_3)_4N]_2MnX_4$ (X=Cl, Br) (Rodríguez-Lazcano, Nataf e Rodríguez, 2009). These vibrations were separated into Cl-Cu-Cl bendings and Cl-Cu-Cl stretchings. **Figure 33** shows the calculated atomic Raman modes in $CsCuCl_3$, which were described around the $[Cu_2Cl_9]^{5-}$ dimer unit.

Table 8 – Experimental Raman (Exp.) at room-pressure (300K), low-temperature (9.2K) and Density Functional Perturbation Theory (DFPT) phonon frequencies in $CsCuCl_3$ calculated using GGA pseudopotential. The corresponding lattice constant are $a = b = 7.19$ Å, c = 18.08 Å. The modes were given for the wavevector along the Γ in the Brillouin zone. (C. W. Tomblin, G. D. Jones e R. W. G. Syme, 1984; Jara *et al.*, 2019; Nataf *et al.*, 2017; Petzelt *et al.*, 1981)

Mode Frequency	Mode Sym (R)	Exp. (300K) (cm^{-1})	Exp. (9.2 K) (cm^{-1})	DFTP (cm^{-1})	Vibrational Assignment
ω_1	E_1		109	105.8	δ_{as} (Cl-Cu-Cl) str.
ω_2	E_2		115	116.1	δ_s (Cl-Cu-Cl) str.
ω_3	E_2	115	121	122.3	τ (Cl-Cu-Cl) wk.
ω_4	E_2	132	136	138.1	ω (Cl-Cu-Cl) str.
ω_5	E_2		145	152.6	ρ (Cl-Cu-Cl) str.
ω_6	E_1		155	156.8	γ (Cl-Cu-Cl) str.
ω_7	A	155	161	160.9	γ (Cl-Cu-Cl) str.
ω_8	E_1		167	164.0	ω (Cl-Cu-Cl) str.
ω_9	E_2	177	180	175.5	τ (Cl-Cu-Cl) str.
ω_{10}	E_2		190	191.4	ν (Cu-Cl) wk.
ω_{11}	E_1	191	196	210.3	ν_s (Cl-Cu-Cl) wk.
ω_{12}	A	242	245	245.9	ν_s (Cl-Cu-Cl) str.
ω_{13}	E_1	265	267	266.4	ν (Cu-Cl) wk.
ω_{14}	A		276	267.4	ν_{as} (Cl-Cu-Cl) str.
ω_{15}	E_2	286	292	273.7	ν_s (Cl-Cu-Cl) str.

Abbreviations: δ: bending; τ: twisting/torsion; ω: wagging; ρ: rocking; γ: scissoring; ν: stretching; as: asymmetric; s: symmetric; str: strong; wk: weak.

Source: Elaborated by the author.

The temperature-dependent Raman spectra of $CsCuCl_3$ in the low-temperature range of 9.2 to 300 K are presented in **Figure 34**. As anticipated, the material does not exhibit a structural phase transition (SPT) within the temperature range investigated. In the absence of an SPT, the behavior of the phonon mode (ω) and the Full Width at Half Maximum (FWHM) can be described by the Balkanski model equations (13) and (14), respectively (Balkanski, Wallis e Haro, 1983). These equations have been successfully applied to various materials and consider contributions from three- and four-phonon anharmonic processes. The equations are given by:

$$\omega(T) = \omega_0 + C\left[1 + \frac{2}{e^x - 1}\right] + D\left[1 + \frac{3}{e^y - 1} + \frac{3}{(e^y - 1)^2}\right] \quad (13)$$

$$\Gamma(T) = A\left[1 + \frac{2}{e^x - 1}\right] + B\left[1 + \frac{3}{e^y - 1} + \frac{3}{(e^y - 1)^2}\right] \quad (14)$$

where A, B, C, and D are constants reflecting the strength of the anharmonic contributions and the ω_0 is the zero-temperature frequency of the corresponding vibrational mode without spin-phonon interaction. To simplify the analysis, the dimensionless parameters $x = \hbar\omega_0/2k_BT$ and $y = \hbar\omega_0/3k_BT$ were also used in these equations. The adjustment of the equations (13) and (14) in the experimental data (see **Figure 35**) allows for a detailed description of the paramagnetic phase (T > 15 K) of $CsCuCl_3$, with the values of the anharmonic constants for each curve summarized in **Table 9**. However, it should be noted that the obtained values of the anharmonic constants should be regarded as estimates rather than precise values due to the assumptions and approximations used in the model.

Figure 33 – Calculated atomic vibrations for Raman-actives modes in $CsCuCl_3$. Note that the dimer unit $[Cu_2Cl_9]^{5-}$ is described along the *a*, *b* and *c* directions.

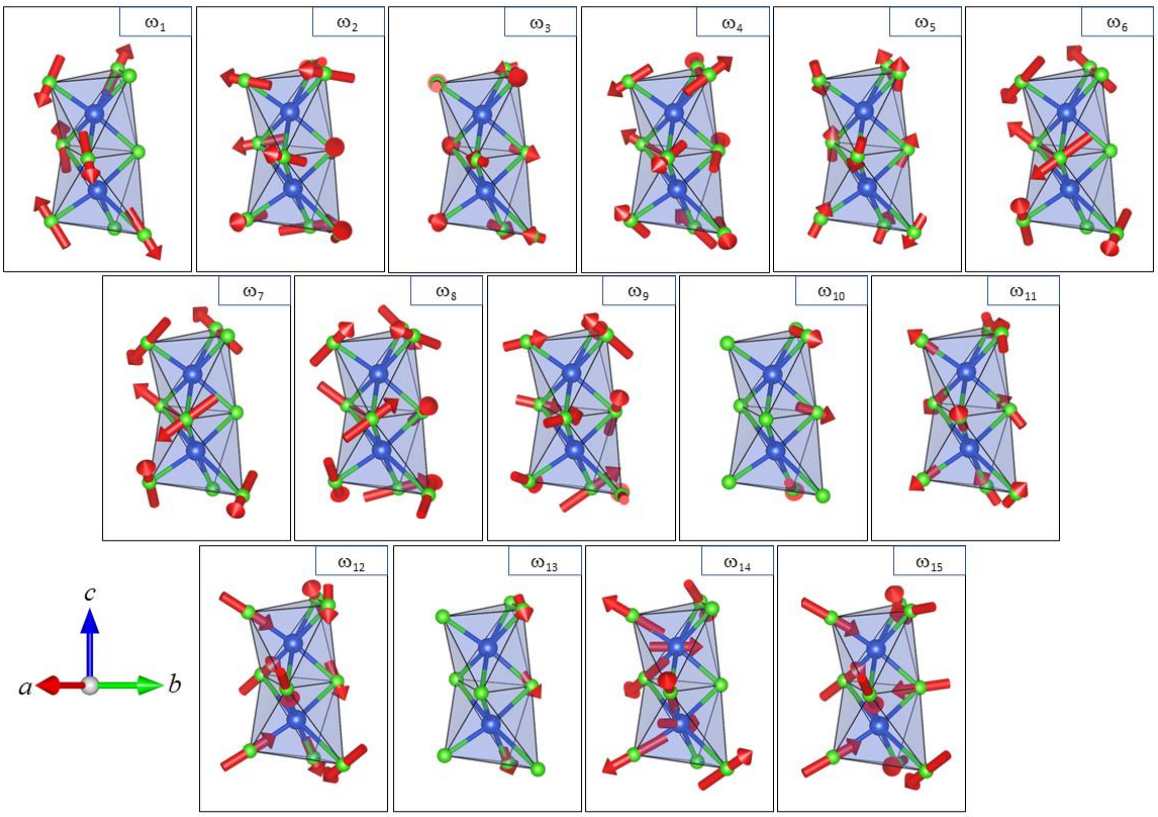

Source: Elaborated by the author.

Figure 34 – Temperature-dependence of the Raman spectra of $CsCuCl_3$ in the ranges **(a)** 100-145 cm^{-1}, **(b)** 145-175 cm^{-1}, **(c)** 175-225 cm^{-1}, **(d)** 225-250 cm^{-1}, **(e)** 250-280 cm^{-1}, and **(f)** 280-310 cm^{-1}.

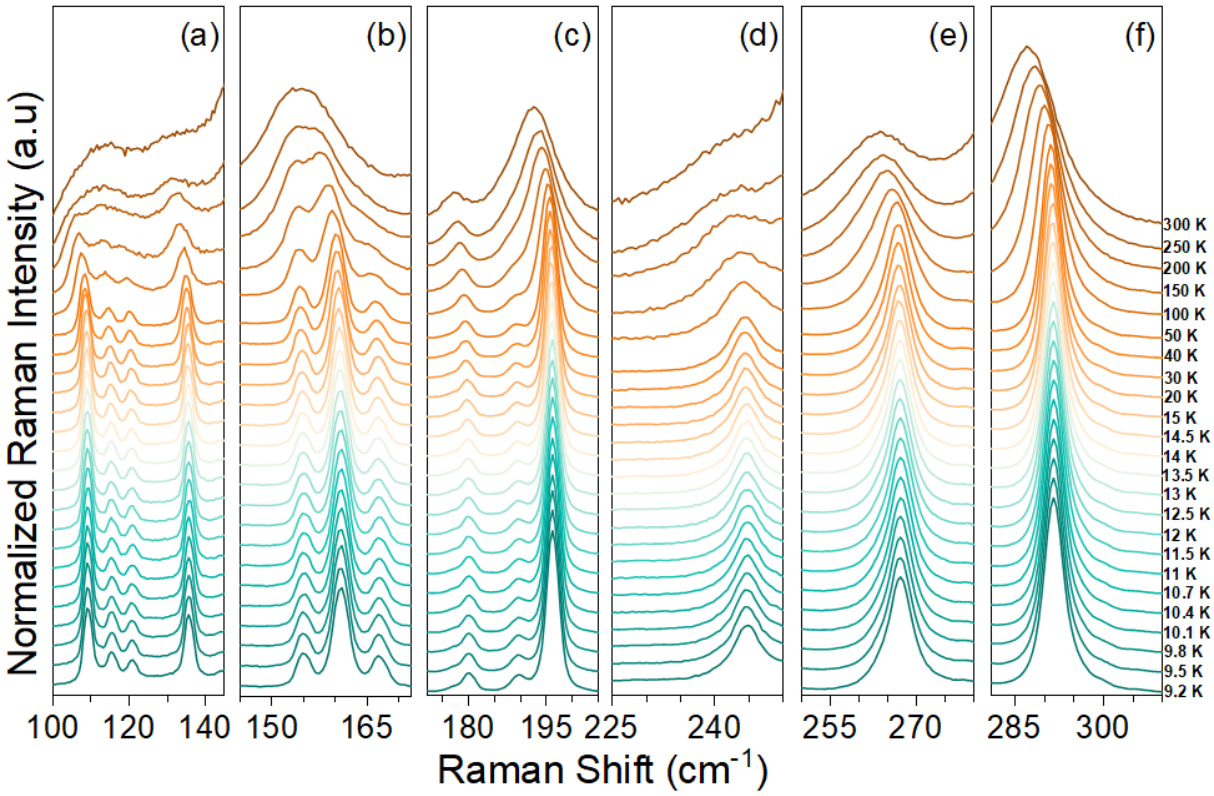

Source: Elaborated by the author.

The phonons depicted in **Figure 36** exhibit anomalies in both the $\omega(T)$ and $\Gamma(T)$ models around T^* = 15 K. There is an abrupt hardening of vibrations until the antiferromagnetic transition at T_N = 10.7 K. Below T_N, there is a softening of the Raman modes. Notably, T^* represents a new low-temperature correlation in the system, unrelated to any abnormal lattice distortion, electronic phase transition, or reported structural or magnetic phase transitions in the compound. This result suggests a spin-phonon coupling (SPC) in $CsCuCl_3$, which is reflected in modifying both mode parameters (position and FWHM). The SPC noticeably affects the vibrational frequencies by renormalizing the phonon frequencies. Typically, these frequency changes are small, predominantly on the order of 1 cm^{-1} or even smaller. However, the changes are systematic, which gives robustness to the result.

Figure 35 – Temperature-dependence of phonon frequencies (left axes) and FWHM (right axes) for selected phonons in paramagnetic (described by equations (13) and (14): solid lines).

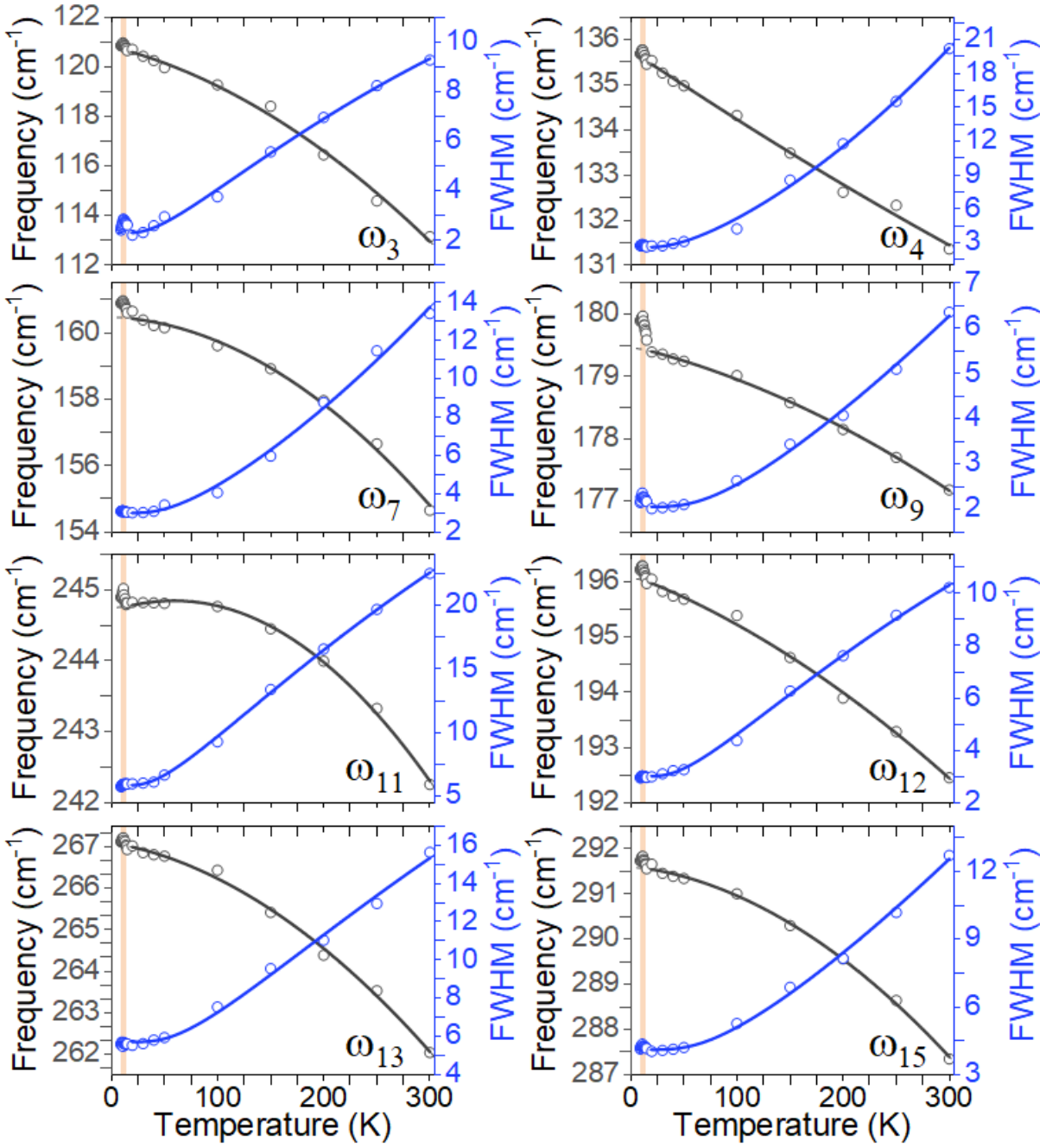

Source: Elaborated by the author.

Figure 36 – Temperature-dependence of phonon frequencies (left axes) and FWHM (right axes) for selected phonons in paramagnetic (described by equations (13) and (14): solid lines) and antiferromagnetic phase, where the orange band described an anomalous hardening region (10.7 K < T^*< 15 K) for (a) ω_3, (b) ω_4, (c) ω_7, (d) ω_{11}, (e) ω_{12}, (f) ω_{13}, and (g) ω_{15} phonons.

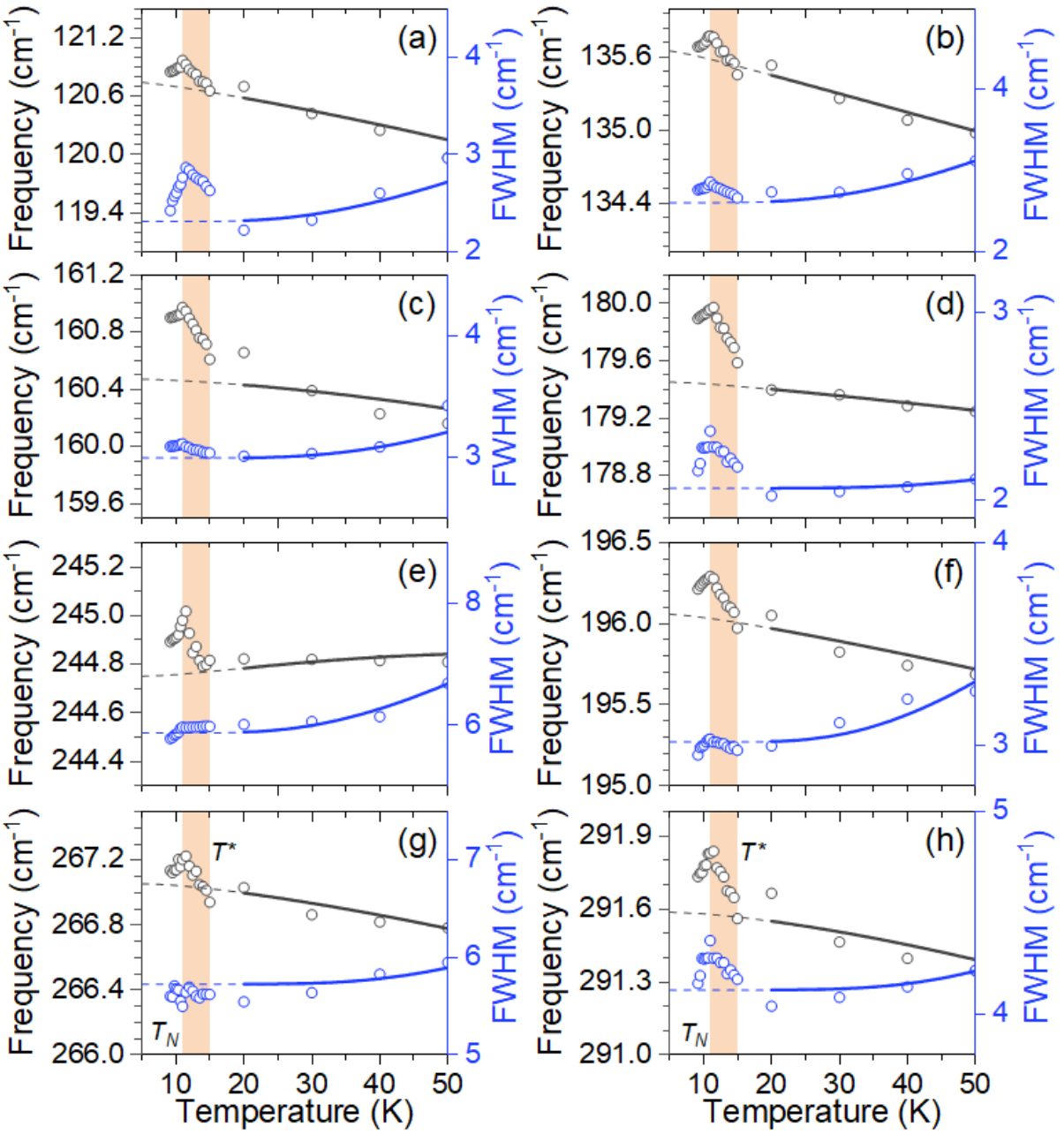

Source: Elaborated by the author.

The contribution of the spin-phonon interaction can be described using the static spin-spin correlation average, given as $\Delta\omega = \omega - \omega_0 = \lambda\langle \boldsymbol{S}_i \cdot \boldsymbol{S}_j \rangle$, where λ is the coupling constant, and $\langle \boldsymbol{S}_i \cdot \boldsymbol{S}_j \rangle$ denotes the statistical average for the neighboring spins in the i and j sites (Aytan *et al.*, 2017; Du *et al.*, 2019; Silva *et al.*, 2013). Thus, at $T > T^*$ (paramagnetic phase) the $\langle \boldsymbol{S}_i \cdot \boldsymbol{S}_j \rangle$ the term is null, since there is no spin ordering. However, at $T_N < T <$

T^*, it is already observed a renormalization on the mode frequency before T_N. This is solid evidence that an unconventional magnetic correlation (frustration, quantum phase, for example) is occurring in $CsCuCl_3$ before the antiferromagnetic ordering. This kind of behavior was already reported in antiferromagnetic RMn_2O_5 (R=Bi, Eu, Dy) compounds (García-Flores *et al.*, 2006, 2007).

The magnetic order may couple to the phonon frequencies through modulation of the DM interaction parameter. However, for $T_N < T$, the contribution of the softening is driven by the AFM effect. Therefore, it is convenient to estimate the magnetic contribution to the renormalization of the phonon frequency as a function of $\Delta\omega$. The easiest way to do this is by estimating the $\Delta\omega$ dependence with the mean-field approach $((\langle S^z \rangle)/S)^2)$ described by the molecular-field approximations mechanism as $(M(T)/M_0)^2$, where $M(T)$ is the temperature dependence of magnetization, and M_0 is the magnetization at zero-temperature (Araújo *et al.*, 2020; Prosnikov *et al.*, 2018). To obtain the $(M(T)/M_0)^2$ was using (Yamamoto *et al.*, 2021) longitudinal susceptibility $\chi_{||}$ data at low temperatures obtained at $H = 1T$. Thus, based on the spin-phonon coupling mechanism proposed by (Granado *et al.*, 1999), the phonon renormalization induced by the SPC could be reduced as:

$$\Delta\omega = \omega - \omega_0 \;=\; \lambda\langle \boldsymbol{S}_i \cdot \boldsymbol{S}_j \rangle \propto \left(\frac{M(T)}{M_0}\right)^2 \tag{15}$$

Figure 37 shows the $\Delta\omega$ as a function of $(M(T)/M_0)^2$ for the selected phonons. By the proposed model given in equation (15), the presence of a linear correlation between the phonon renormalization process and modifications in the linear profile slope for each temperature range ($T^* > 15$ K; $T_N < T < T^*$; $T_N < T$) confirms the existence of spin-phonon coupling. Notably, the observed phonon changes at T^* strongly suggest the onset of SPC in $CsCuCl_3$, which is unrelated to any lattice distortion, electronic phase transition, or reported structural or magnetic phase transitions in the material, as discussed before. The obtained slopes related to the SPC are summarized in **Table 9**. These results provide strong evidence supporting the proposed models for phonon energy renormalization correction. It is worth noting that the slope modifications observed in **Figure 37** are consistent with related materials such as Cs_2OCl_2 (Araújo *et al.*, 2018). The observed anomalies in the phonon spectrum of $CsCuCl_3$ at T^* indicate the onset of SPC, which affects the vibrational frequencies. The linear correlation strongly supports the existence of SPC in $CsCuCl_3$.

Table 9 – Three (A/C)- and four (B/D)-phonon anharmonic contributions to the frequencies and FWHMs of selected phonons.

Mode Frequency	ω_0 (cm^{-1})	A	B	C	D	$\Delta\omega_{T^*}$ (cm^{-1})	$\Delta\omega_{T_N}$ (cm^{-1})
ω_3	120.8 ± 0.2	2.80 ± 0.01	-0.06 ± 0.01	-0.07 ± 0.02	-0.0013 ± 0.0003	0.14	0.07
ω_4	135.8 ± 0.1	2.30 ± 0.02	0.30 ± 0.01	-0.12 ± 0.01	0.0002 ± 0.0001	-0.09	-0.02
ω_7	160.5 ± 0.1	2.70 ± 0.02	0.20 ± 0.01	-0.10 ± 0.01	-0.0026 ± 0.0003	0.49	0.44
ω_9	179.5 ± 0.1	1.97 ± 0.06	0.09 ± 0.01	-0.04 ± 0.01	-0.0069 ± 0.0001	0.46	0.45
ω_{11}	196.1 ± 0.1	3.11 ± 0.08	-0.09 ± 0.01	-0.08 ± 0.02	-0.0011 ± 0.0003	0.15	0.13
ω_{12}	244.6 ± 0.1	6.02 ± 0.03	-0.14 ± 0.02	0.07 ± 0.01	-0.0047 ± 0.0002	0.30	0.27
ω_{13}	267.1 ± 0.1	5.90 ± 0.02	-0.18 ± 0.06	-0.07 ± 0.02	-0.0051 ± 0.0008	0.07	0.03
ω_{15}	291.6 ± 0.1	3.94 ± 0.01	0.18 ± 0.01	-0.04 ± 0.02	-0.0057 ± 0.0005	0.20	0.19

Source: Elaborated by the author.

In this context, low-temperature Raman spectroscopy was performed on $CsCuCl_3$ to investigate the spin-phonon coupling. The results revealed a renormalization process in the frequency and FWHM parameters for selected phonons related to the Cl-Cu-Cl bendings and stretchings. The spin-phonon coupling generated an anticipated contribution to the phonon frequencies, which was observed at $T^*=15\ K$ due to the significant magnetic frustration in the sample. A hardening of the phonon temperature dependence was observed around the expected renormalization temperature value T_N = 10.7 K, with another modification observed due to the involvement of the AFM effect. Based on the description of $\Delta\omega$ as a function of $(M(T)/M_0)^2$, it is possible to confirm the modification around the spin-phonon coupling renormalization process at T^*. This consideration supports and suggest a significant magnetic frustration in the sample between the paramagnetic and AFM phases.

Figure 37 – Temperature-dependence from the anharmonic behavior of selected phonon as a function of $(M(T)/M_0)^2$ for a) ω_3, (b) ω_4, (c) ω_7, (d) ω_{11}, (e) ω_{12}, (f) ω_{13}, and (g) ω_{15} phonons. (The purple, blue and red are linear guides for the eyes separated for each region).

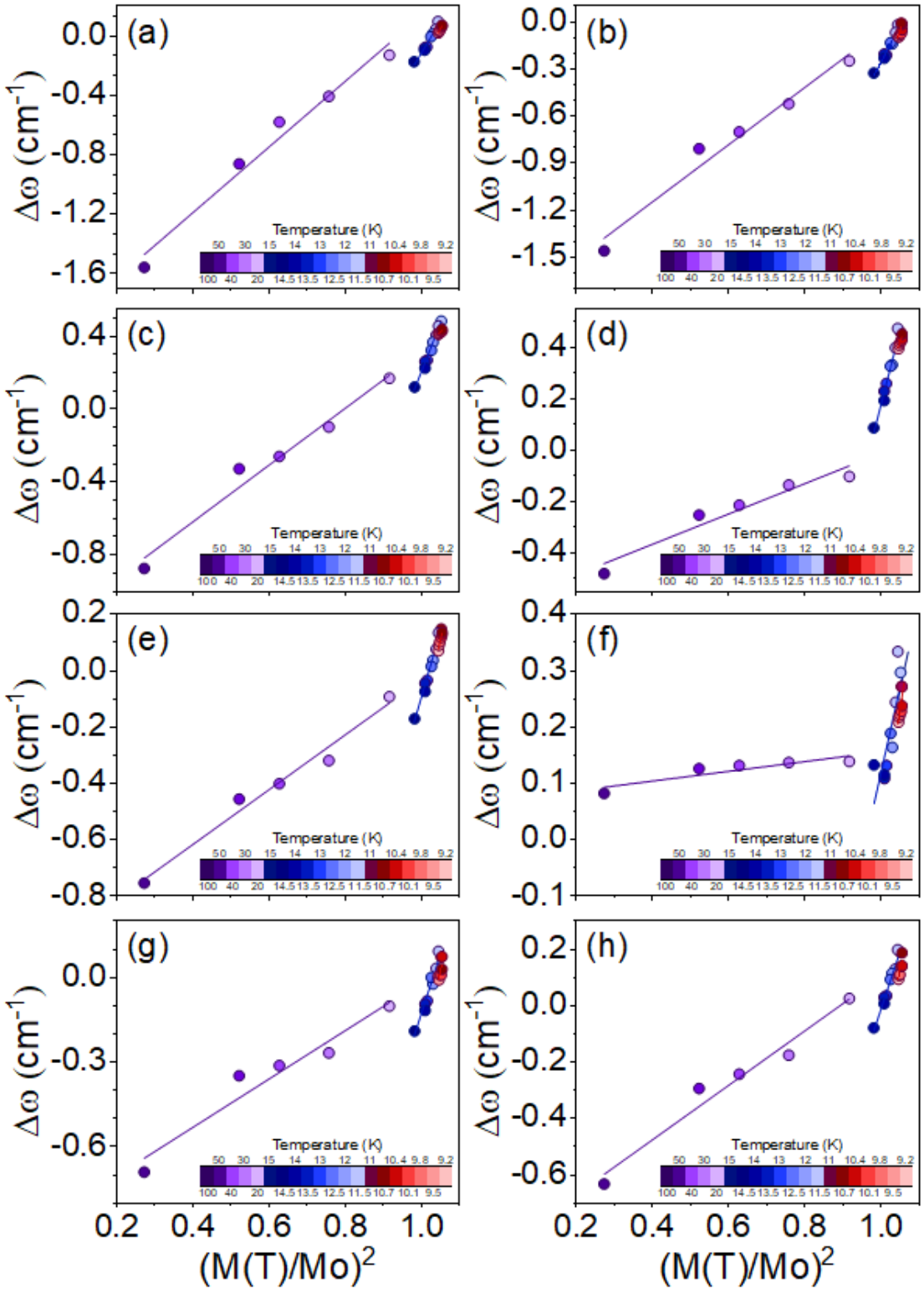

Source: Elaborated by the author.

5.3 Pressure-Induced structural phase transition on $CsCuCl_3$

As was previously described, the $CsCuCl_3$ exhibits under pressure-induced quantum phases, which enhances the neighboring spins in the sample and modifies the magnetic diagram by the enhanced Dzyaloshinskii-Moriya interaction (Hosoi, Matsuura e Ogata, 2018; Sera *et al.*, 2017). Although different authors have studied $CsCuCl_3$, the compound offers the possibilities of studies with high-pressure with Synchrotron powder X-Ray diffraction (SPXRD) and Raman spectroscopy. Interestingly, based on the results, the compound undergoes a first-order structural phase transition (SPT) at a critical pressure P_c = 3.69 GPa from the *LP-Phase*: $P6_522$ to the *HP-Phase*: $C2$. In the pressure range of 2.79-3.57 GPa has observed a coexisted phase between both *LP-* and *HP-phases*. The direct relation in the crystal axis enables natural slow crystal modification without significant dynamic instability. The investigation revealed that the SPT involves the reorganization of the internal $[CuCl_6]^{4-}$ octahedra, with Cl-Cu-Cl bending contributing more than Cl-Cu-Cl stretchings.

Figure 38 shows the pressure-dependence SPXRD pattern of $CsCuCl_3$. At room conditions, the crystal structure is consistent with the hexagonal $P6_522$, as reported by (Cui *et al.*, 2020) (ICSD: 120370). The diffraction patterns are well described by the same $P6_522$ up to 2.38 GPa. However, above the critical pressure P_c = 3.69 GPa, the diffractograms exhibit abrupt changes, indicating the presence of new angle reflections. Which can be attributed to a pressure-induced structural phase transition (SPT) in the sample. At around P_{ex} = 2.91 GPa, both the Low-Pressure Phase (*LP-phase*) and High-Pressure Phase (*HP-Phase*) coexist. Notably, the emergence of new diffraction peaks, such as the splitting of the 6.6° band and the appearance of the distribution of the peak around 10° (**Figure 38** (b)-(c)), are observed. The rise in displayed peaks indicates a decreased structural symmetry related to the *HP-phase*. No remarkable changes in the diffraction patterns were detected from P_c up to 9 GPa, indicating that the $CsCuCl_3$ does not undergo any other phase transformation within the maximum pressure range explored in this work.

All patterns of the *LP-phase* were refined within the Rietveld method using the EXPO2014 (Altomare *et al.*, 2013) software with the hexagonal $P6_522$ measurement obtained in our single-crystal X-ray diffraction technique. To investigate the crystal structure of the *HP-phase*, primarily was compared used the orthorhombic $CsCuBr_3$ ($C222_1$) structure reported in (Li e Stucky, 1973) (ICSD: 10184) as a possible solution. However, the reflection index of the simulated DRX patterns did not match the experimental data. Notably, our results differ from

the high-temperature SPT (C. J. Kroese, W. J. A. Maaskant e G.C. Verschoor, 1974; Kroese e Maaskant, 1974b; Wim J. A. Masskant, 1995), which involves a hexagonal to hexagonal $P6_122$ or $P6_522$ → $P6_3/mmc$ at 423 K, and the high-pressure hexagonal sub-cell ($P6_3/mmc$) encountered at 3.04 GPa by (Andrew G. Christy *et al.*, 1994) (ISCD:32503). A comparison of all diffractograms is provided in **Figure 39**.

Figure 38 – Variation of the SPXRD pattern of the $CsCuCl_3$ under pressure.

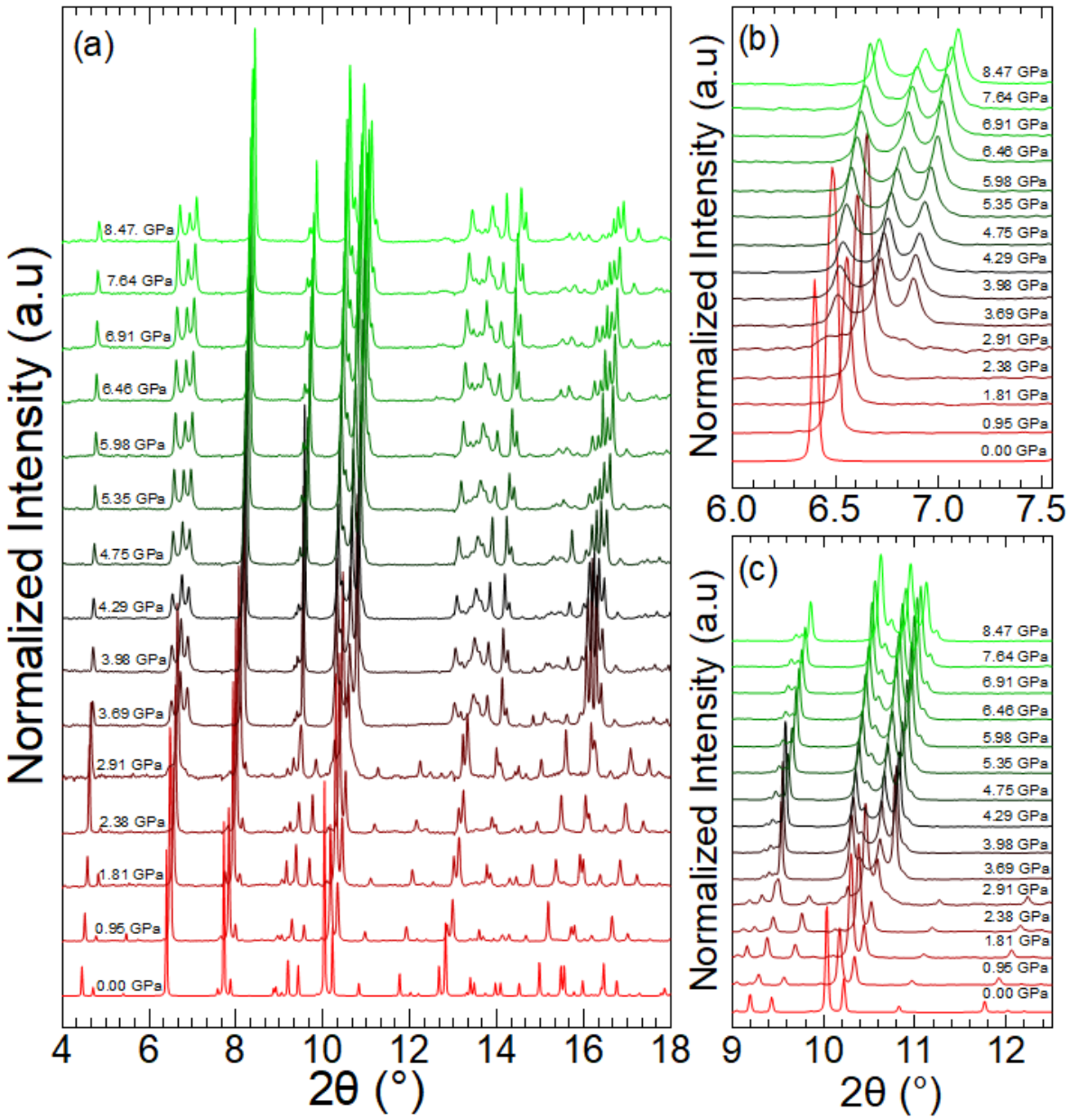

Source: Elaborated by the author

Figure 39 – Simulated patterns of the $CsCuCl_3$ ($P6_522$ - ICSD: 120370), $CsCuCl_3$ ($P6_3/mmc$ - ISCD:32503), $CsCuBr_3$ ($C222_1$ - ICSD: 10184) and the $CsCuCl_3$ synchrotron powder X-ray diffraction pattern obtained at 3.63 GPa.

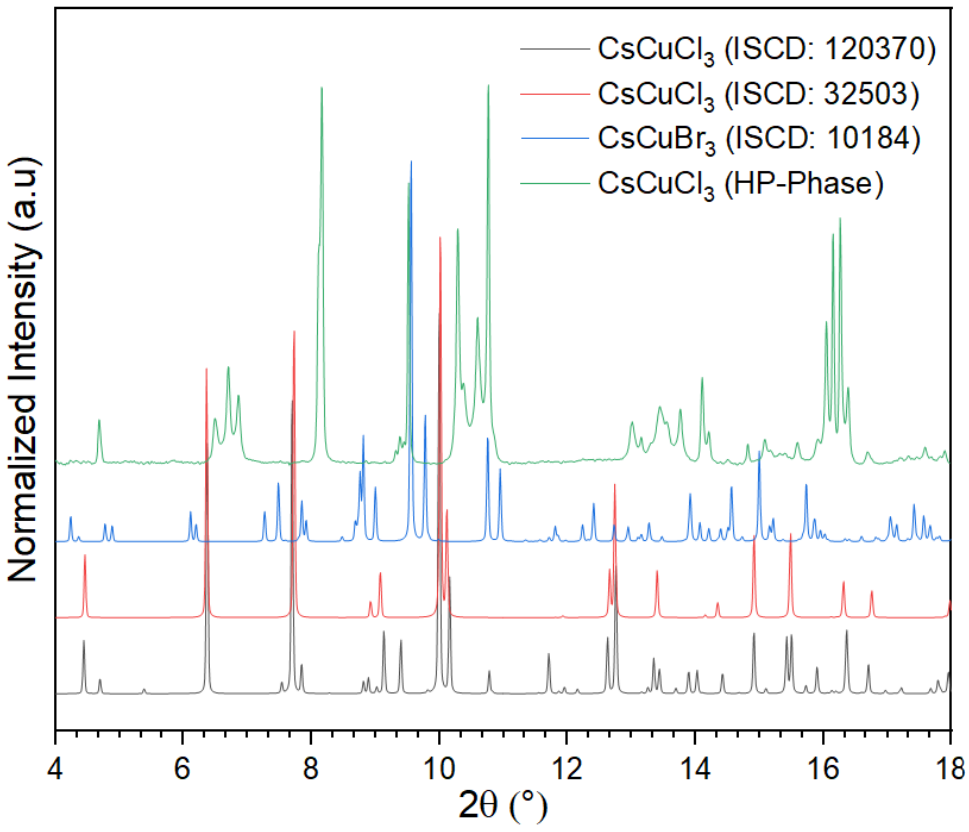

Source: Elaborated by the author.

Figure 40 – **(a)** Group-subgroup phases diagram from $P6_522$ to $C2$, and **(b)** the comparison between the *HP-phase* experimental data diffractograms and the monoclinic space group possibilities.

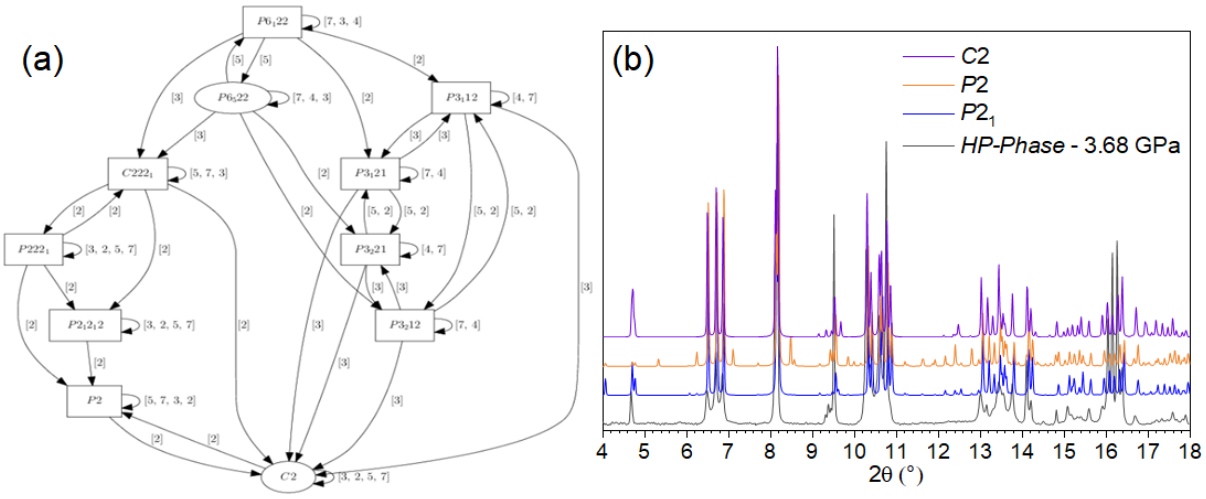

Source: Elaborated by the author.

The methodology for determining the high-pressure crystal structure involves a multi-step approach. Firstly, the phase was indexed by DICVOL06 (Boultif e Louër, 2004) to determine the lattice system. Secondly, a group-subgroup diagram was used to explore the crystal modification possibilities; subsequently, the symmetry of the structure was verified using the pseudosymmetry search tools provided and available at the Bilbao Crystallographic Server (La Flor, de *et al.*, 2016), and the PLATON software (Spek, 2003). Finally, the diffraction patterns obtained from the simulated crystallography models from the *HP-phase* were compared to the experimental data. The group-subgroup diagram from $P6_522$ to *C2*, and the diffraction patterns related to the simulated crystallographic modeling of the *HP-phase* are presented in **Figure 40**.

Figure 41 – The $P6_522$ crystal structure refinement by the Rietveld method at 0.95 GPa, and the *C*2 phase refinement by *Le-Bail* at 3.68 GPa.

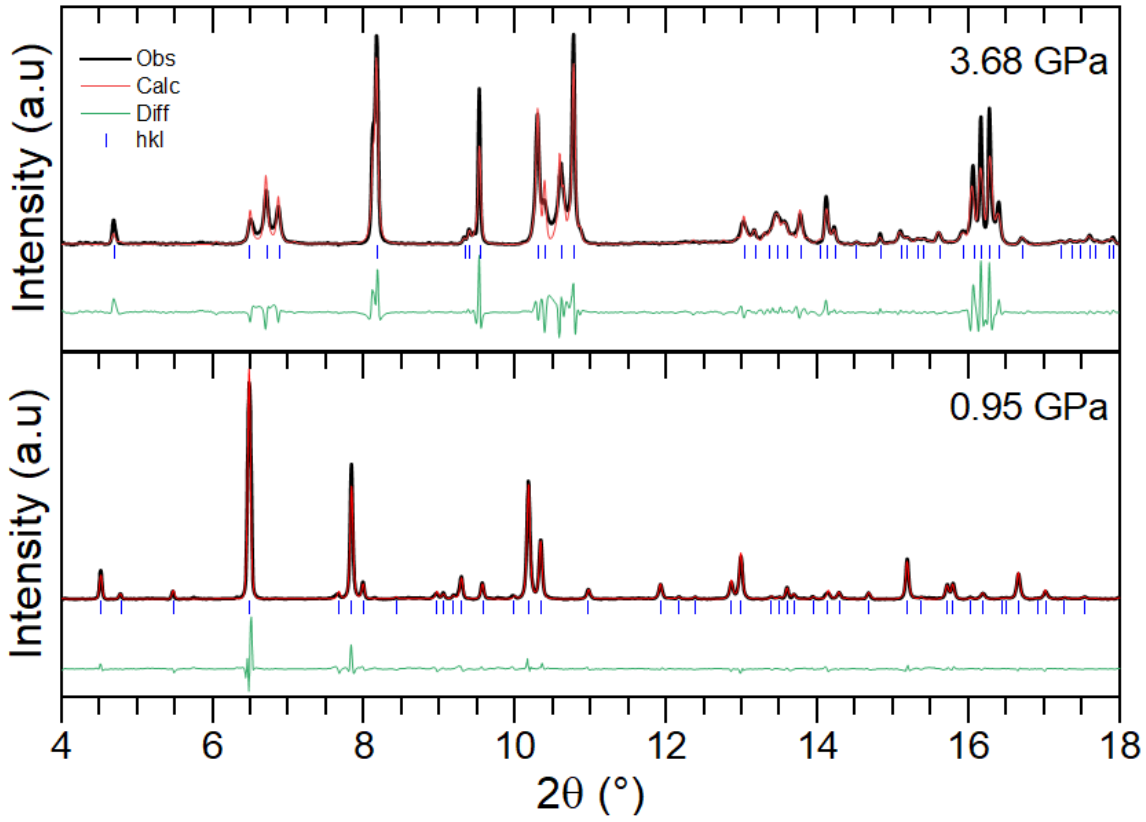

Source: Elaborated by the author.

The *HP-Phase* was refined by the Rietveld method using the EXPO2014 software. The crystallographic model used was the monoclinic crystal structure with *C*2 as a space group, which was found to have the simulated diffraction pattern with a more exact peak position than the experimental diffractogram. A correlation between phases was observed in the graphical

representation between the space groups $P6_522 \rightarrow C2$ generated using the group-subgroup program (Ivantchev et al., 2002), but a direct transformation was not described in the diagram. The low diffraction intensity due to the sample texture and preferential orientation does not permit a high-quality resolution. Nevertheless, our methodology allowed the determination of the crystal structure cell, the symmetry from SPXRD patterns, and the Crystal Information File (CIF) with the atomic position. The crystal structure refinement of both phases is described in **Figure 41**.

Figure 42 – The $CsCuCl_3$ crystal structure: **(a)** *LP-phase* ($P6_522$), and **(b)** *HP-phase* ($C2$). **(c)** The hexagonal (dashed black lines), orthorhombic base reduction (red lines) and monoclinic ($C2$ - dashed green lines), and **(d)** the crystal phases transformation basic-sets.

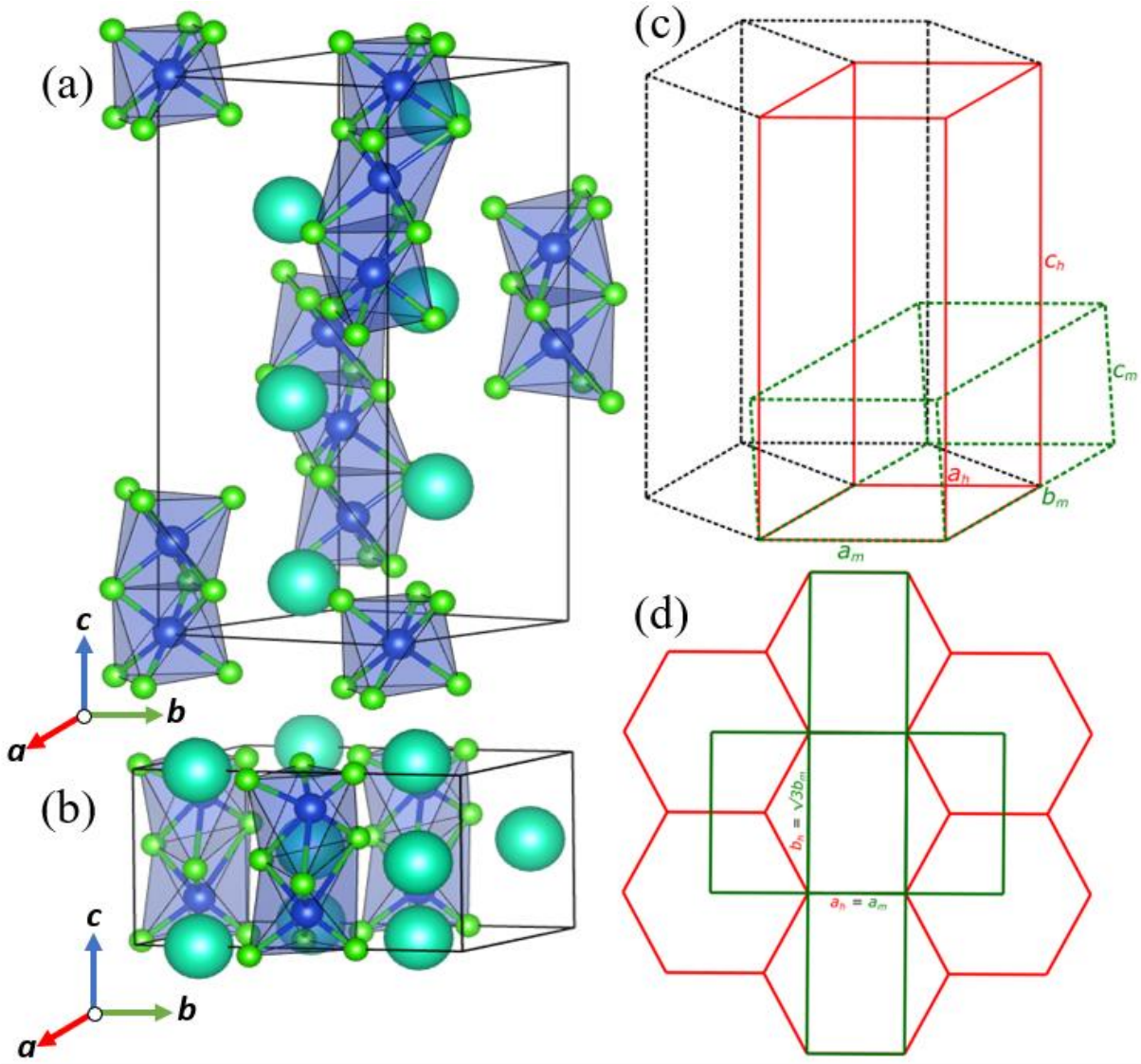

Source: Elaborated by the author.

Figure 43 – (**a)-(e)** The lattice parameters as a function of pressure. (**f)** Third-order Birch-Murnanghan fit for each pressure phase. The orange dashboard represents the coexists phases of both crystal structures.

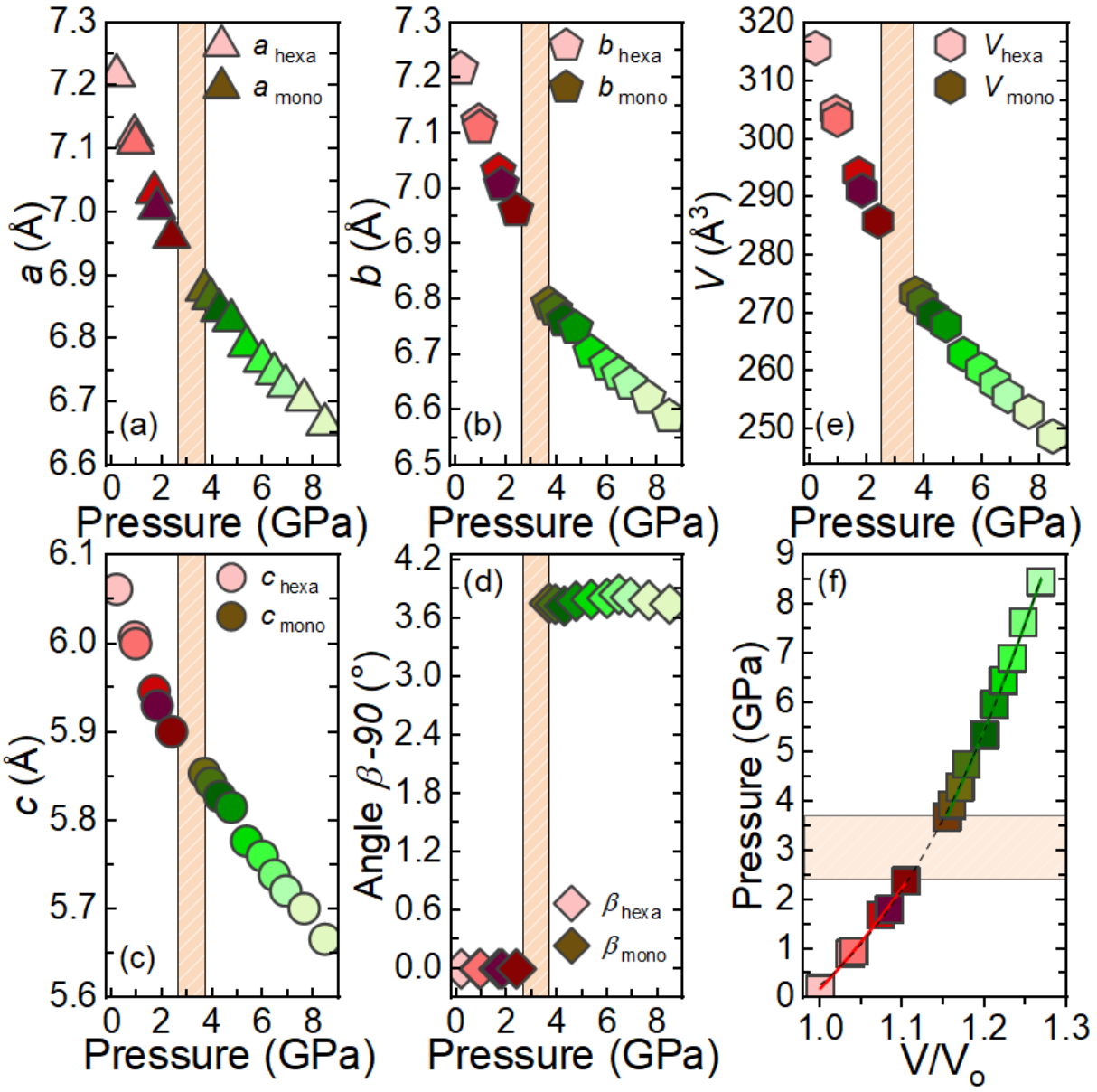

Source: Elaborated by the author.

At room-pressure, the $CsCuCl_3$ adopts the $P6_522$ ($a = b = 7.2168$ (10) Å, $c = 18.1853$ (5) Å) with a *3*-fold rotational symmetry along the principal *c*-axis. The cooper (located at the center) and chlorine (vertices of the octahedron) atoms form a distorted octahedron coordination geometry $[CuCl_6]^{4-}$. Each octahedron shares a common edge, forming a linear chain of octahedra that runs through the crystal structure along the principal axis. Cs^+ ions occupy the interstitial sites between the displayed chains. Under high-pressure, the crystal structure undergoes the structural phase transition to the *C*2 (a = 6.8875 (12) Å, b = 6.7918 (2) Å, c =

5.8539 (10) Å, β = 93.76 (4) °) system due to the compression of the crystal lattice. The *HP-phase* presents a lower degree of symmetry, but the octahedra chain continues to be displayed around the *c*-axis. To facilitate the discussion of the relationship between both phases, a transformation was made on the crystal cell parameters: $a_h = a_m$; $\sqrt{3}b_h = b_m$; $c_h = 3c_m$. (see **Figure 42**). **Figure 43** (a)-(e) shows the pressure dependence of the reduced unit-cell parameters; a shift over all lattice parameters was observed, indicating the crystal modification.

Although the pressure-induced structural phase transition in the material can be determined through the previous analysis of the diffractograms and lattice parameters, the resulting relative shift can generate uniaxial stress as a function of the compound elastic anisotropy, which can be predicted by the Equation of State (EOS) (Birch, 1947; Goodwin, Keen e Tucker, 2008; Sata *et al.*, 2002). The third-order Birch-Murnaghan EOS was used to fit the pressure-dependent of the unit cell volume (see **Figure 43**(f)). The equation was expressed in terms of the volume at zero pressure (V_0), the bulk modulus $B_0 = (-V\partial P/\partial V)_T$, and the dimensionless pressure derivative $B' = (\partial B/\partial P)_T$ (dimensionless), which describes how B_0 change with pressure (Katsura e Tange, 2019):

$$P = \frac{3}{2}B_0\left[\left(\frac{V_0}{V}\right)^{\frac{7}{3}} - \left(\frac{V_0}{V}\right)^{\frac{5}{3}}\right]\left[1 + \frac{3}{4}(B' - 4)\left\{\left(\frac{V_0}{V}\right)^{\frac{2}{3}} - 1\right\}\right] \qquad (16)$$

Table 10 displays the parameters obtained from fitting the pressure-dependent changes in the unit cell volume using the third-order Birch-Murnaghan EOS. The SPT $P6_522 \rightarrow C2$ was accompanied by increased unit-cell volume (V_0/V), which is consistent and expected for high-pressure phases with higher bulk moduli due to their denser and less compressible crystal structure (Svitlyk *et al.*, 2014). The B_0 values typically range from 10 to 70 GPa for hybrids/inorganic materials based on metal halide perovskites (Agbaoye, Adebambo e Adebayo, 2019; Chaves *et al.*, 2014; Tu *et al.*, 2021). The low bulk modulus of metal halide perovskites is thought to contribute to their unique properties, such as self-healing, ion migration, and low thermal conductivity, which suggest applications in the flexible electronics industry for their ductility (Rakita *et al.*, 2015; Sun *et al.*, 2015). The value of B' indicates a slow stiffening of the material, which can be attributed to the first-order structural phase transition, where both *LP*- and *HP*- phases can be related to a unique basic-set. The presence of dynamic instability in the sample was not observed, and the positive value of B' compensated for any instability.

Table 10 – Experimental coefficients of the Murnaghan equation of state for $CsCuCl_3$ in each structural phase.

Symmetry	P_{range} (GPa)	V_0 (Å^3)	B_0 (GPa)	B'
$P6_522$	0.1 – 2.38	319.42 ± 0.02	17 ± 3	4.39 ± 0.04
$C2$	3.69 – 8.47	304.62 ± 0.06	27 ± 9	4.26 ± 0.07

Source: Elaborated by the author.

Table 11 – Group factor analysis of the $CsCuCl_3$ crystal structure at room pressure (space group $P6_522$ (179))

HP-Phase – C2 (5)			
Atoms	**Wyckoff notation**	**Site symmetry**	**Irreducible representation**
Cs_{01}	*2a*	C_2	$A\oplus 2B$
Cs_{02}	*2b*	C_2	$A\oplus 2B$
Cu_{01}	*4c*	C_1	$3A\oplus 3B$
Cl_{01}	*4c*	C_1	$3A\oplus 3B$
Cl_{02}	*2a*	C_2	$A\oplus 2B$
Cl_{03}	*2b*	C_2	$A\oplus 2B$
Cl_{04}	*4c*	C_1	$3A\oplus 3B$
	Total	C_2^3	$13A\oplus 17B$
Modes Classifications			
			$\Gamma_{raman}=12A\oplus 15B$
			$\Gamma_{IR}= 12A\oplus 15B$
			$\Gamma_{acoustic}= A\oplus 2B$
			$\Gamma_{silent}= -$

Source: Elaborated by the author.

Since the Raman spectra are very sensible to the crystalline structure, Raman spectroscopy has been performed in $CsCuCl_3$, increasing hydrostatic pressure at room temperature to confirm the SPT. The group theory analysis (Kroumova *et al.*, 2003; Rousseau, Bauman e Porto, 1981) for both crystal phases are presented in **Table 7** and **Table 11**, which predicts that the $CsCuCl_3$ material exhibits 60 vibration modes in the *LP*-phase, and 30 vibration modes in the *HP*-phase. The Raman-active mode distributions are represented as $\Gamma_{raman}=6A_1\oplus 15E_2\oplus 14E_1$ for the point group D_6 ($P6_522$) in the *LP*-phase, and 27 Raman phonons with $12A\oplus 15B$ distribution for the point group C_2^3 ($C2$) in the *HP*-phase.

Figure 44 – **(a)** Raman spectra pressure-induced of the $CsCuCl_3$ powder. **(b)** Frequency center as a function of hydrostatic pressure. The orange dashboard represents the coexisting *LP-* and *HP- phases* region.

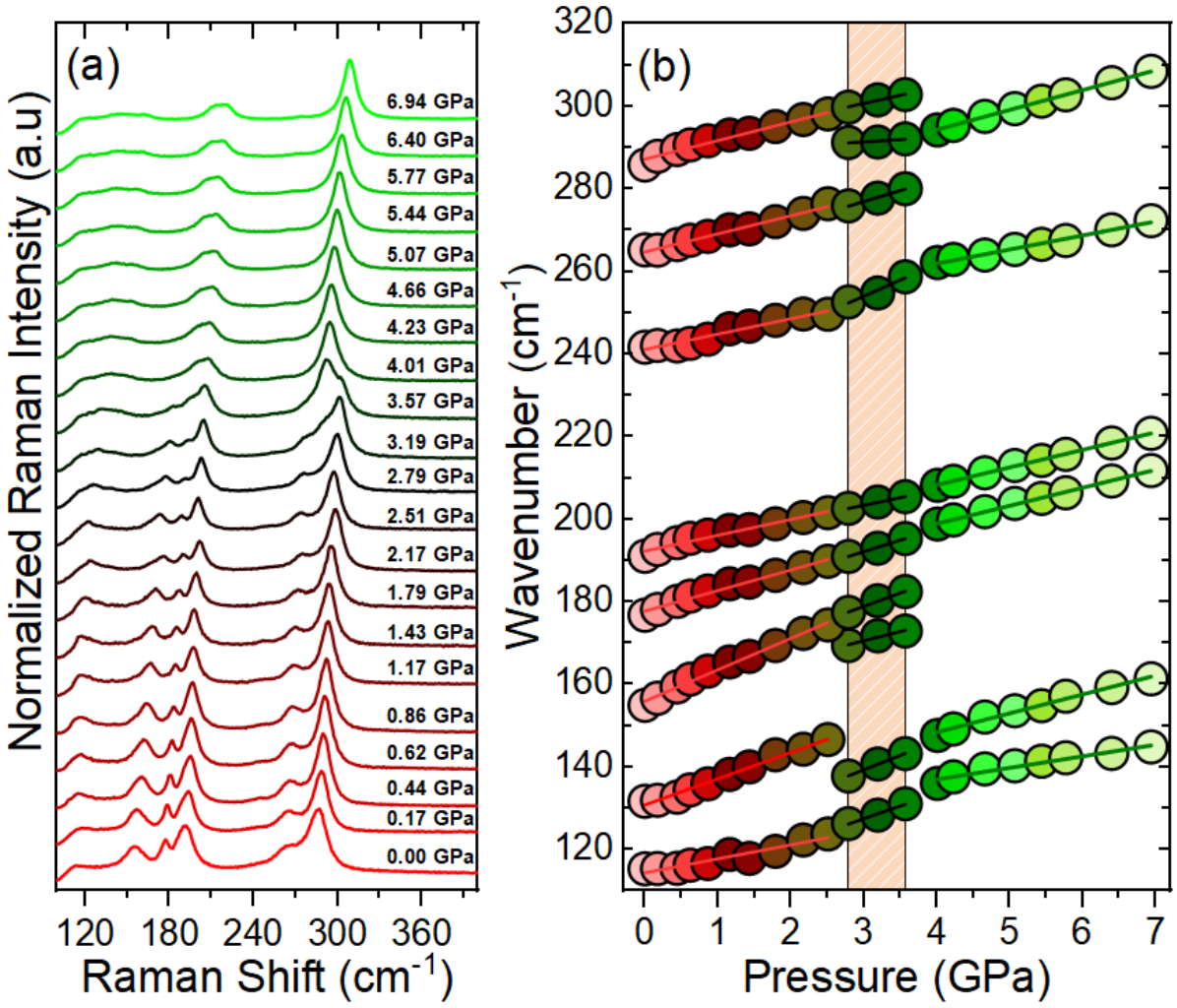

Source: Elaborated by the author

The Raman spectra pressure dependence is shown in **Figure 44**(a), in which all vibrational modes are characterized by a significant redshift. From room-pressure up to 2.51 GPa, the pressure-induced Raman spectrum maintains the same peaks profile as the *LP-phase*. Hence, a reorganization process involving the $[CuCl_6]^{4-}$ octahedra was observed in a 2.79-3.57 GPa range, where both *LP-* and *HP-* phases coexist, leading to the slow crystal modification base, which compensates for the not dynamic instability in the sample. Consistent with SPXRD, a sudden change in the Raman spectra pressure-dependence modification is observed at 4.01 GPa, where new peaks are displayed in the *HP-phase*. In general, the mode frequency in the sample increases linearly with pressure for all peaks and suffers dislocations at the limit point

of the coexistence phase and 4.01 GPa, which can be attributed to the hardening and broadening of the displayed vibrational bands, as shown in **Figure 44**(b).

Table 12 – Experimental Raman modes for $CsCuCl_3$ in each structural phase and their corresponding Grüneisen parameters. The material's bulk modulus was B_0 = 17 GPa and B_0 = 27 GPa for each phase, obtained from the fit of the SPXRD pattern by the third-order Birch-Murnaghan equation.

LP-Phase			Coexistence Phase			*HP-Phase*		
ω_i (cm^{-1})	$(\partial\omega_i/\partial P)_T$ (cm^{-1}/GPa)	γ_{iT}	ω_i (cm^{-1})	$(\partial\omega_i/\partial P)_T$ (cm^{-1}/GPa)	γ_{iT}	ω_i (cm^{-1})	$(\partial\omega_i/\partial P)_T$ (cm^{-1}/GPa)	γ_{iT}
–	–	–	109	6.2 ± 0.6	–	126	2.8 ± 0.2	0.600
114	3.4 ± 0.3	0.507	118	7.0 ± 0.2	–	130	4.6 ± 0.2	0.955
131	6.3 ± 0.2	0.818	157	4.5 ± 0.8	–	–	–	–
156	7.6 ± 0.2	0.828	160	6.5 ± 0.4	–	–	–	–
178	5.0 ± 0.2	0.478	176	5.5 ± 0.3	–	182	4.4 ± 0.1	0.653
192	3.8 ± 0.2	0.336	193	3.6 ± 0.1	–	191	4.2 ± 0.1	0.594
241	3.7 ± 0.3	0.261	231	7.8 ± 0.9	–	248	3.4 ± 0.1	0.370
265	4.4 ± 0.2	0.282	261	5.3 ± 0.4	–	–	–	–
–	–	–	288	1.1 ±0.5	–	275	4.8 ± 0.1	0.471
287	4.5 ± 0.3	0.267	289	3.9 ± 0.3	–	–	–	–

Source: Elaborated by the author.

Note that pressure dependence of the phonons progressively becomes less resolved, probably due to stress-induced along the structural phase transition, or could be a consequence of the increase in the sample bulk modulus. Furthermore, the Cl-Cu-Cl bendings under pressure contribute more to the reorganization around the structural phase transition for the number of displayed bands. However, the most intense band in the Raman spectra, the Cu-Cl stretching, is associated with the stronger distortion of $[CuCl_6]^{4-}$ for the significant redshift. The Grüneisen parameters ($\gamma_{iT} = (B_0/\omega_i)(\partial\omega_i/\partial P)_T$) of each mode are presented **Table 12**, reflecting this behavior. At the coexistence phase, the original *LP-phase* displayed Raman bands increased from 8 to 10. As was observed, the Cl-Cu-Cl bending peaks have higher values of γ_{iT} than the Cu-Cl stretching, contributing to the modification in $[CuCl_6]^{4-}$. Comparing the phonon frequencies, the Cu-Cl stretching exhibits more significant shifts, which is consistent with previous observations. This result establishes the structural correlations between bulk modulus and the corresponding local Grüneisen parameter.

Figure 45 – The decompression pressure cycle of the $CsCuCl_3$, until 2.55 GPa the sample did not return to the original or even to the coexisting phases, displaying a P_c hysteresis value but the release shown the reversible cycle.

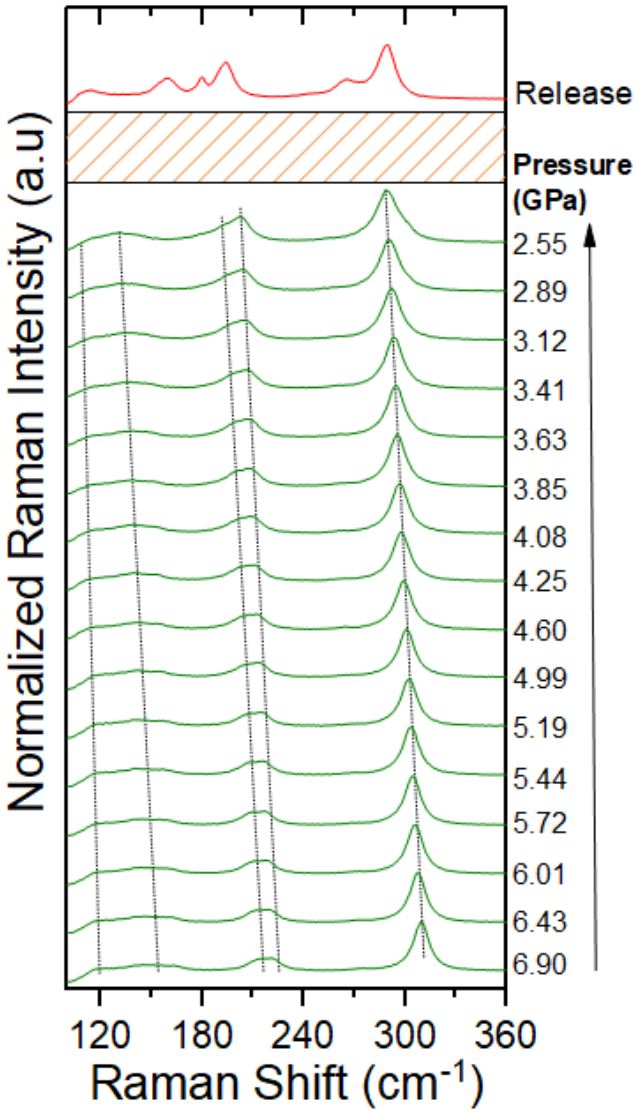

Source: Elaborated by the author.

Until 9 GPa, the $CsCuCl_3$ material does not suffer amorphization under pressure. In fact, the steady decrease of the hydrostatic pressure until the full release of pressure is shown in **Figure *45***. The decompression cycle modified the P_c value, indicating a small degree of residual strain in the compound. The reversible first-order phase transition was observed until the total pressure release; the coexisting region could be responsible for the slow liberation of pressure and the readjustment to the original crystal structure. However, the recovery of the low-pressure phase suggests that this system is well preserved.

Ultimately, the structural phase transition (SPT) of $CsCuCl_3$ under pressure was studied using synchrotron powder X-ray diffraction and Raman spectroscopy. Our results suggest that the compound undergoes a first-order SPT at a critical pressure P_c = 3.69 GPa from the *LP-Phase*: $P6_522$ to the *HP-Phase*: $C2$. In the pressure range of 2.79-3.57 GPa has observed a coexisted phase between both *LP*- and *HP-phases*. Interestingly, the direct relation in the crystal axis enables natural slow crystal modification without significant dynamic instability, suggesting that $CsCuCl_3$ has a certain level of flexibility. The bulk modulus calculations of the sample for each phase obtained $B_0^{LP} = 17 \pm 3$, and $B_0^{HP} = 27 \pm 9$ indicates that $CsCuCl_3$ may have potential applications in the flexible electronics industry due to its structural *"softness."* The investigation revealed that the SPT involves the reorganization of the internal $[CuCl_6]^{4-}$ octahedra, with Cl-Cu-Cl bending contributing more than Cl-Cu-Cl stretchings. It was found that the displayed band ω_2 is associated with a stronger distortion, as evidenced by the significant shift presence and the highest γ_{iT} value. Furthermore, our study demonstrated that the SPT is reversible, but residual strain pressure influences the modification of the P_c value upon pressure decrease. These studies funding provided additional information about modifying the $[CuCl_6]^{4-}$ under pressure and enhanced our understanding of the lattice distortion at external pressure. This may contribute to developing new applications for $CsCuCl_3$ in flexible electronics.

6 CONCLUSIONS

Metal halide-like-perovskites exhibit promising properties in various fields, such as multiferroics and optoelectronics, making them attractive candidates for investigation and development. Investigating these materials under extreme conditions, such as hydrostatic pressure or low temperatures, can provide valuable insights into their fundamental structural-property relationship and help to develop new applications. In this work has been investigated $Cs_2FeCl_5.H_2O$, $DMAPbBr_3$, $DMAPbI_3$ and $CsCuCl_3$ perovskite-like compounds under extreme conditions, and the main conclusions were:

i) $Cs_2FeCl_5.H_2O$ exhibits a SPT from the orthorhombic *Cmcm* to the monoclinic *C2/c* at low temperatures (T = 156K). Such SPT in the compound is well-suggested as a full ferroelastic phase of weakly first-order (or nearly second-order) nature, where the displacive mechanism drives a slight tilt of about $\varphi = 1°$ around the low-temperature *c*-axis. An inclination of a water molecule by $\theta = 71°$, the Cs···H interactions to be highly responsive to the movement between Cs^+ ion and $[FeCl_5.H_2O]^{2-}$, which are oriented to each other. However, H ···H interactions increase the contribution of the electronic bonds after the SPT (by approximately 2%), which is attributed to the hardening of these ligands, compensating for the weakening H···Cl contact. The structural change can be described as the ferroelastic species *mmmF2/m*. A steady low-temperature cell parameter dependence described by strain matrix theory explains the structural order in the sample, where the strain-adapted symmetry component e_5 exhibits second-order behavior consistent with Landau theory, and the elastic constant of the compound doubles at low temperatures. Hard-modes described by Raman spectroscopy validate the ferroelastic nature of the phase transition. These results provide valuable insights into the novel complex multiferroic behavior in $Cs_2FeCl_5.H_2O$ and propose potential applications for this material in multifunctional devices that harness the coupling between their different ferroic orders.

ii) The SPT undergone by $DMAPbBr_3$ was characterized using synchrotron powder X-ray diffraction and Raman spectroscopy. The compound undergoes a first-order structural phase transition through an order-disorder mechanism at 250 K, related to the unique structural arrangement of the *4H*-hexagonal type perovskite. Interestingly, the compound exhibits positive thermal expansion parallel to the *ab* plane and negative thermal expansion in the *c*-axis, which is attributed to the coupling between anisotropic lattice distortion and the reorientation of the DMA cations. Raman spectroscopy measurements reveal a weakening of the intermolecular interactions (*H*-bond) upon heating, indicating a correlation with the DMA^+

cation dynamics in the high-temperature phase related to the frameworks. The combined use of synchrotron powder X-ray diffraction and Raman spectroscopy provides a comprehensive understanding of the structural and lattice dynamics of $DMAPbBr_3$ and sheds light on the importance of the cation-framework interaction in organic-inorganic hybrid perovskites.

iii) The investigation at low temperatures has provided valuable insights into the thermo-chromatic and luminescent properties of like-perovskite $DMAPbI_3$. The observed SPT, which exhibits an order-disorder mechanism, leads to the emergence of novel self-trapped exciton (STEs) contributions in the photoluminescence spectra at *Tc*. These STEs modify the intensity of the emitted light, resulting in different chromaticity coordinates. The observed changes in color and brightness are attributed to the relaxation of the crystal structure, which enables the appearance of previously inaccessible states. The significant contribution of STEs and their dependence on electron-phonon coupling has been discussed, revealing the dominant contribution of this interaction to the PL temperature dependence. This study deepens our understanding of the electron-phonon coupling strength. Overall, this work provides important insights into the tunable optical properties of low-dimensional hybrid halide perovskites, which could have significant applications in developing advanced optoelectronic devices.

iv) The low-temperature Raman spectroscopy in $CsCuCl_3$ describes a spin-phonon coupling in the sample by indicating a renormalization process in the frequency and FWHM parameters for selected phonons associated with Cl-Cu-Cl bendings and stretchings. This spin-phonon coupling generates an anticipated contribution to the phonon frequencies, which was observed at T^* = 15 K due to the significant magnetic frustration in the sample. A hardening of the phonon temperature dependence was observed around the expected renormalization temperature value T_N = 10.7 K related to the AFM effect in the sample. The magnetic frustration is supported based on the description of $\Delta\omega$ as a function of $(M(T)/M_0)^2$. This consideration suggests the modification around the spin-phonon coupling renormalization process at T^*.

v) On the other hand, an SPT of $CsCuCl_3$ was studied at high-pressure using synchrotron powder X-ray diffraction and Raman spectroscopy. These results suggest that the compound undergoes a first-order SPT at a critical pressure P_c = 3.69 GPa from the *LP-Phase*: $P6_522$ to the *HP-Phase: C*2. Interestingly, a coexisted phase between *LP*- and *HP-phases* was observed in the pressure range of 2.79-3.57 GPa. The direct relation in the crystal axis enables natural slow crystal modification without significant dynamic instability, suggesting that $CsCuCl_3$ has a certain level of flexibility. Our bulk modulus calculations for each phase obtained $B_0^{LP} = 17 \pm 3$, and $B_0^{HP} = 27 \pm 9$. Furthermore, SPT involves the reorganization of the internal $[CuCl_6]^{4-}$ octahedra, with Cl-Cu-Cl bending contributing more than Cl-Cu-Cl

stretchings, enhancing the understanding of the lattice distortion at external pressure, contributing to the development of new applications for $CsCuCl_3$ in flexible electronics.

In conclusion, studying structural phase transitions and related physical phenomena in halide perovskites under extreme conditions is of great importance for understanding their fundamental properties and exploring their potential applications in various fields. Investigations into the behavior of these materials under high pressure or low temperature have revealed significant modifications in their structural, electronic, and optical properties. The changes in lattice parameters, phonon frequencies, and electron-phonon coupling strengths observed during the phase transitions can be utilized to design new functional materials for applications in optoelectronics, flexible electronics, and smart windows. Furthermore, the reversibility of the phase transitions and the effect of residual strain pressure on the critical pressure values provide valuable insights into the behavior of halide perovskites under external stimuli. Overall, halide perovskites under extreme conditions offer an opportunity to deepen our understanding of the fundamental physics of these materials and their potential for various technological applications.

REFERENCES

ACKERMANN, M.; BRÜNING, D.; LORENZ, T.; BECKER, P.; BOHATÝ, L. Thermodynamic properties of the new multiferroic material $(NH_4)_2[FeCl_5(H_2O)]$. **New Journal of Physics**, v. 15, 2013.

ACKERMANN, M.; LORENZ, T.; BECKER, P.; BOHATÝ, L. Magnetoelectric properties of $A_2[FeCl_5(H_2O)]$ with A = K, Rb, Cs. **Journal of Physics Condensed Matter**, v. 26, n. 50, 17 dez. 2014.

ADAMS, D. M.; D. C. NEWTON. Single-crystal Raman Study of Some Aquo-pentachloro-salts $[MCI_5\text{-}(H_2O)]^{2-}$ (M= In or Fe). **Journal of the Chemical Society, Dalton Transactions**, n. 5, p. 681–686, 1972.

ADAMS, M.; LOCK, P. J. A Survey Study of the Vibrational Spectra of Some Aquo-halogeno- complexes. **Journal of the Chemical Society A: Inorganic, Physical, Theoretical**, p. 2801–2806, 1971.

AGBAOYE, R. O.; ADEBAMBO, P. O.; ADEBAYO, G. A. First principles comparative studies of thermoelectric and other properties in the cubic and hexagonal structure of $CsCdCl_3$ halide perovskites. **Computational Condensed Matter**, v. 21, 1 dez. 2019.

AHN, J.; LEE, E.; TAN, J.; YANG, W.; KIM, B.; MOON, J. A new class of chiral semiconductors: chiral-organic-molecule-incorporating organic–inorganic hybrid perovskites. **Materials Horizons**, v. 4, n. 5, p. 851–856, 1 set. 2017.

AIZU, K. Determination of the State Parameters and Formulation of Spontaneous Strain for Ferroelastics. **Journal of the Physical Society of Japan**, v. 28, n. 3, p. 706–716, 15 mar. 1970a.

AIZU, K. Possible Species of Ferromagnetic, Ferroelectric, and Ferroelastic Crystals. **Physical Review B**, v. 2, n. 3, p. 754–772, 1 ago. 1970b.

AIZU, K. Presentation and Discussion of Examples of Ferroelectrics and Ferroelastics Having the Index of Faintness Unequal to the Cell Multiplicity. **Journal of the Physical Society of Japan**, v. 33, n. 5, p. 1390–1395, nov. 1972.

AKKERMAN, Q. A.; MANNA, L. What Defines a Halide Perovskite? **ACS Energy Letters**, v. 5, n. 2, p. 604–610, 14 fev. 2020.

ALAEI, A.; CIRCELLI, A.; YUAN, Y.; YANG, Y.; LEE, S. S. Polymorphism in metal halide perovskites. **Materials Advances**, v. 2, n. 1, p. 47–63, 2021.

ALBERTO RODRÍGUEZ-VELAMAZÁN, J.; FABELO, Ó.; MILLÁN, Á.; CAMPO, J.; JOHNSON, R. D.; CHAPON, L. Magnetically-induced ferroelectricity in the $(ND_4)_2[FeCl_5(D_2O)]$ molecular compound. **Scientific Reports**, v. 5, 29 set. 2015.

ALLARDO, M. C. G.; OMERO, F. J. R.; AYWARD, S. A. H.; ALJE, E. K. H. S. Phase transitions in perovskites near the tricritical point : an experimental study of $KMn_{1-x}Ca_xF_3$ and $SrTiO_3$. v. 64, n. December, p. 971–982, 2000.

ALTOMARE, A.; CUOCCI, C.; GIACOVAZZO, C.; MOLITERNI, A.; RIZZI, R.; CORRIERO, N.; FALCICCHIO, A. *EXPO2013* : a kit of tools for phasing crystal structures

from powder data. **Journal of Applied Crystallography**, v. 46, n. 4, p. 1231–1235, 1 ago. 2013.

ANDREW G. CHRISTY; ROSS J. ANGEL; JULIAN HAINEST; SIMON M. CLARK. Crystal structural variation and phase transition in caesium trichlorocuprate at high pressure. **Journal of Physics: Condensed Matter**, v. 6, p. 3125–3136, 1994.

ANELLI, C.; CHIEROTTI, M. R.; BORDIGNON, S.; QUADRELLI, P.; MARONGIU, D.; BONGIOVANNI, G.; MALAVASI, L. Investigation of Dimethylammonium Solubility in $MAPbBr_3$ Hybrid Perovskite: Synthesis, Crystal Structure, and Optical Properties. **Inorganic Chemistry**, v. 58, n. 1, p. 944–949, 7 jan. 2019.

ANGEL, R. J.; GONZALEZ-PLATAS, J.; ALVARO, M. EosFit7c and a Fortran module (library) for the equation of state calculations. **Zeitschrift fur Kristallographie**, v. 229, n. 5, p. 405–419, 2014.

ARAÚJO, B.; ARÉVALO-LÓPEZ, A. M.; SANTOS, C.; ATTFIELD, J.; PASCHOAL, C.; AYALA, A.; ARAÚJO, B. S.; SANTOS, C. C.; ATTFIELD, J. P.; PASCHOAL, C. W. A.; AYALA, A. P. Spin-phonon coupling in monoclinic $BiCrO_3$. **Journal of Applied Physics**, v. 2020, n. 11, p. 114102, 2020.

ARAÚJO, B. S.; ARÉVALO-LÓPEZ, A. M.; ATTFIELD, J. P.; PASCHOAL, C. W. A.; AYALA, A. P. Spin-phonon coupling in melanothallite Cu_2OCl_2. **Applied Physics Letters**, v. 113, n. 22, 26 nov. 2018.

ARDIT, M.; MARTUCCI, A.; CRUCIANI, G. Monoclinic-Orthorhombic Phase Transition in ZSM-5 Zeolite: Spontaneous Strain Variation and Thermodynamic Properties. **Journal of Physical Chemistry C**, v. 119, n. 13, p. 7351–7359, 2015.

ARUNAN, E. *et al.* Defining the hydrogen bond: An account (IUPAC Technical Report). **Pure and Applied Chemistry**, v. 83, n. 8, p. 1619–1636, 2011.

ARUNAN, E.; MANI, D. Dynamics of the chemical bond: Inter- and intra-molecular hydrogen bond. **Faraday Discussions**, v. 177, p. 51–64, 1 abr. 2015.

AYTAN, E.; DEBNATH, B.; KARGAR, F.; BARLAS, Y.; LACERDA, M. M.; LI, J. X.; LAKE, R. K.; SHI, J.; BALANDIN, A. A. Spin-phonon coupling in antiferromagnetic nickel oxide. **Applied Physics Letters**, v. 111, n. 25, 18 dez. 2017.

BALENTS, L. Spin liquids in frustrated magnets. **Nature**, v. 464, p. 199–208, 11 mar. 2010.

BALKANSKI, M.; WALLIS, R. F.; HARO, E. Anharmonic effects in light scattering due to optical phonons in silicon. **Physical Review B**, v. 28, n. 4, p. 1928–1934, 15 ago. 1983.

BARTEL, C. J.; SUTTON, C.; GOLDSMITH, B. R.; OUYANG, R.; MUSGRAVE, C. B.; GHIRINGHELLI, L. M.; SCHEFFLER, M. New tolerance factor to predict the stability of perovskite oxides and halides. **Science Advances**, v. 5, n. 2, 8 fev. 2019.

BECERRA, C. C.; PADUAN-FILHO, A.; FRIES, T.; SHAPIRA, Y.; GABAS, M.; CAMPO, J.; PALACIO, F. Low-field remanent magnetization in site-diluted easy-axis

antiferromagnets. A universal behavior. **Journal of Magnetism and Magnetic Materials**, v. 140–144, p. 1475–1476, fev. 1995.

BECHIR, M. BEN; DHAOU, M. H. Study of Charge Transfer Mechanism and Dielectric Relaxation of $CsCuCl_3$ Perovskite Nanoparticles. **Materials Research Bulletin**, v. 144, 1 dez. 2021.

BELLA, F.; GRIFFINI, G.; CORREA-BAENA, J.-P.; SARACCO, G.; GRÄTZEL, M.; HAGFELDT, A.; TURRI, S.; GERBALDI, C. Improving efficiency and stability of perovskite solar cells with photocurable fluoropolymers. **Science**, v. 354, n. 6309, p. 203–206, 14 out. 2016.

BERLIE, A.; CAVAYE, H.; LE, M. D. Short-range magnetic order within the multiferroic erythrosiderite mineral $(NH_4)_2FeCl_5.H_2O$. **Physical Review B**, v. 106, n. 10, p. 104433, 30 set. 2022.

BIAN, H.; WANG, H.; LI, Z.; ZHOU, F.; XU, Y.; ZHANG, H.; WANG, Q.; DING, L.; LIU, S.; JIN, Z. Unveiling the Effects of Hydrolysis-Derived DMAI/$DMAPbI_x$ Intermediate Compound on the Performance of $CsPbI_3$ Solar Cells. **Advanced Science**, v. 7, n. 9, 1 maio 2020.

BICHURIN, M.; PETROV, R.; TATARENKO, A. Magnetoelectric Composites: Modeling and Application. **Advances in Materials**, v. 9, n. 2, p. 15, 2020.

BIRCH, F. Finite Elastic Strain of Cubic Crystals*. **Physical Review**, v. 71, n. 11, p. 809–824, 1947.

BORDALLO, H. N.; KOLESOV, B. A.; BOLDYREVA, E. V.; JURANYI, F. Different dynamics of chiral and racemic (L- and DL-) serine crystals: Evidenced by incoherent inelastic neutron and Raman scattering. **Journal of the American Chemical Society**, v. 129, n. 36, p. 10984–10985, 12 set. 2007.

BOULTIF, A.; LOUËR, D. Powder pattern indexing with the dichotomy method. **Journal of Applied Crystallography**, v. 37, n. 5, p. 724–731, out. 2004.

BRENNER, T. M.; EGGER, D. A.; KRONIK, L.; HODES, G.; CAHEN, D. Hybrid organic - Inorganic perovskites: Low-cost semiconductors with intriguing charge-transport properties. **Nature Reviews Materials**, v. 1, n. 1, 11 jan. 2016.

BRUKER (2018). **SAINT Bruker AXS Inc**, 2012.

BRUKER (2018). **APEX3 Bruker AXS Inc,** 2018.

BURGER, S.; GROVER, S.; BUTLER, K. T.; BOSTRÖM, H. L. B.; GRAU-CRESPO, R.; KIESLICH, G. Tilt and shift polymorphism in molecular perovskites. **Materials Horizons**, v. 8, n. 9, p. 2444–2450, 1 set. 2021.

C. J. KROESE; W. J. A. MAASKANT; G.C. VERSCHOOR. The High-Temperature Structure of CsCuCI3. **Acta Crystallographica Section B**, v. 30, p. 1053–1056, 1974.

C. W. TOMBLIN; G. D. JONES; R. W. G. SYME. Raman scattering and infrared absorption spectra of Co^{2+} ions in $CsMgBr_3$ and $CsCdBr_3$. **J. Phys. C: Solid State Phys**, v. 17, p. 4345–4368, 1984.

CAMPO, J.; LUZÓN, J.; PALACIO, F.; MCINTYRE, G. J.; MILLÁN, A.; WILDES, A. R. Understanding magnetic interactions in the series $A_2FeX_5{\cdot}H_2O$ A=K, Rb; X=Cl, Br). II. Inelastic neutron scattering and DFT studies. **Physical Review B**, v. 78, n. 5, p. 054415, 11 ago. 2008.

CAO, F.; LI, L. Progress of Lead-Free Halide Perovskites: From Material Synthesis to Photodetector Application. **Advanced Functional Materials**, v. 31, n. 11, 1 mar. 2021.

CARLIN, R. L.; PALACIO, F. The $A_2[FeX_5(H_2O)]$ series of antiferromagnets. **Coordination Chemistry Reviews**, v. 65, p. 141–165, jul. 1985.

CARPENTER, M. A.; SALJE, E. K. H. Elastic anomalies in minerals due to structural phase transitions. **European Journal of Mineralogy**, v. 10, n. 4, p. 693–812, 1998.

CARPENTER, M. A.; SALJE, E. K. H.; GRAEME-BARBER, A. Spontaneous strain as a determinant of thermodynamic properties for phase transitions in minerals. **European Journal of Mineralogy**, v. 10, n. 4, p. 621–691, 1998.

CHAN, T. H.; TAYLOR, N. T.; SUNDARAM, S.; HEPPLESTONE, S. P. Phase Stability and Electronic Properties of Hybrid Organic–Inorganic Perovskite Solid Solution $(CH(NH_2)_2)_x(CH_3NH_{3\ 1-x}Pb(Br_yI_{1-y})_3$ as a Function of Composition. **The Journal of Physical Chemistry C**, v. 126, n. 32, p. 13640–13648, 18 ago. 2022.

CHATTERJEE, S.; PAL, A. J. Influence of metal substitution on hybrid halide perovskites: Towards lead-free perovskite solar cells. **Journal of Materials Chemistry A**, v. 6, n. 9, p. 3793–3823, 2018.

CHAVES, J. M.; FLORÊNCIO, O.; SILVA, P. S.; MARQUES, P. W. B.; SCHNEIDER, S. G. Anelastic relaxation associated to phase transformations and interstitial atoms in the Ti-35Nb-7Zr alloy. **Journal of Alloys and Compounds**, v. 616, p. 420–425, 15 dez. 2014.

CHEN, H. *et al.* Efficient and Stable Inverted Perovskite Solar Cells Incorporating Secondary Amines. **Advanced Materials**, v. 31, n. 46, 1 nov. 2019.

CHEN, XIAO-XIAN; LIU, D.; GONG, Y.; WANG, S.; ZHANG, W.; CHEN, XIAO-MING. Above-Room-Temperature Ferroelastic Phase Transitions in Two Tetrafluoroborate-Based Hexagonal Molecular Perovskites. **Inorganic Chemistry,** v. 61, n. 4, p. 20 Jan. 2219–2226 2022.

CHEN, X.-X.; ZHANG, X.-Y.; LIU, D.-X.; HUANG, R.-K.; WANG, S.-S.; XIONG, L.-Q.; ZHANG, W.-X.; CHEN, X.-M. Room-temperature ferroelectric and ferroelastic orders coexisting in a new tetrafluoroborate-based perovskite. **Chemical Science**, v. 12, n. 25, p. 8713–8721, 2021.

CLIFFE, M. J.; GOODWIN, A. L.; ROAD, S. P. PASCal: A principal-axis strain calculator for thermal expansion and compressibility determination. **Journal of a**, v. 45, p. 1321–1329, 2012.

CLUNE, A. J.; NAM, J.; LEE, M.; HUGHEY, K. D.; TIAN, W.; FERNANDEZ-BACA, J. A.; FISHMAN, R. S.; SINGLETON, J.; LEE, J. H.; MUSFELDT, J. L. Magnetic field-temperature phase diagram of multiferroic $(NH_4)_2FeCl_5{\cdot}H_2O$. **npj Quantum Materials**, v. 4, n. 1, p. 44, 12 ago. 2019a.

COCHRAN, W. Crystal stability and the theory of ferroelectricity. **Advances in Physics**, v. 9, n. 36, p. 387–423, out. 1960.

COLLOCOTT, J.; RAYNE, J. A. Low-temperature heat capacity of linear-chain magnetic compounds $CsNiCl_3$, $RbNiCl_3$, and $CsCuCl_3$. **Journal of Applied Physics**, v. 61, n. 8, p. 4404–4406, 1987.

CUI, S.; CHEN, Y.; TAO, S.; CUI, J.; YUAN, C.; YU, N.; ZHOU, H.; YIN, J.; ZHANG, X. Synthesis, Crystal Structure and Photoelectric Response of All-Inorganic Copper Halide Salts $CsCuCl_3$. **European Journal of Inorganic Chemistry**, v. 2020, n. 22, p. 2165–2169, 16 jun. 2020.

DAR, M. I.; JACOPIN, G.; MELONI, S.; MATTONI, A.; ARORA, N.; BOZIKI, A.; ZAKEERUDDIN, S. M.; ROTHLISBERGER, U.; GRÄTZEL, M. Origin of unusual bandgap shift and dual emission in organic-inorganic lead halide perovskites. **Science Advances**, v. 2, n. 10, 7 out. 2016.

DJURIŠIĆ, A. B.; LIU, F. Z.; TAM, H. W.; WONG, M. K.; NG, A.; SURYA, C.; CHEN, W.; HE, Z. B. Perovskite solar cells - An overview of critical issues. **Progress in Quantum Electronics**, v. 53, p. 1–37, 1 maio 2017.

DOLOMANOV, O. V; BOURHIS, L. J.; GILDEA, R. J.; HOWARD, J. A. K.; PUSCHMANN, H. OLEX2: A complete structure solution, refinement and analysis program. **Journal of Applied Crystallography**, p. 2008–2010, 2009.

DONG, H.; RAN, C.; GAO, W.; LI, M.; XIA, Y.; HUANG, W. Metal Halide Perovskite for next-generation optoelectronics: progress and prospects. **eLight**, v. 3, n. 1, p. 3, 4 jan. 2023.

DONG, S.; LIU, J. M.; CHEONG, S. W.; REN, Z. Multiferroic materials and magnetoelectric physics: Symmetry, entanglement, excitation, and topology. **Advances in Physics**, v. 64, n. 5–6, p. 519–626, 2 nov. 2015.

DU, L. *et al.* Lattice Dynamics, Phonon Chirality, and Spin–Phonon Coupling in 2D Itinerant Ferromagnet Fe_3GeTe_2. **Advanced Functional Materials**, v. 29, n. 48, 1 nov. 2019.

DU, Z. Y.; SUN, Y. Z.; CHEN, S. L.; HUANG, B.; SU, Y. J.; XU, T. T.; ZHANG, W. X.; CHEN, X. M. Insight into the molecular dynamics of guest cations confined in deformable azido coordination frameworks. **Chemical Communications**, v. 51, n. 86, p. 15641–15644, 1 set. 2015.

DU, Z. Y.; XU, T. T.; HUANG, B.; SU, Y. J.; XUE, W.; HE, C. T.; ZHANG, W. X.; CHEN, X. M. Switchable guest molecular dynamics in a perovskite-like coordination polymer toward sensitive thermoresponsive dielectric materials. **Angewandte Chemie - International Edition**, v. 54, n. 3, p. 914–918, 12 jan. 2015.

DUAN, L.; ZHANG, H.; LIU, M.; GRÄTZEL, M.; LUO, J. Phase-Pure γ-$CsPbI_3$ for Efficient Inorganic Perovskite Solar Cells. **ACS Energy Letters**, v. 7, n. 9, p. 2911–2918, 9 set. 2022.

EL-MELLOUHI, F.; MARZOUK, A.; BENTRIA, E. T.; RASHKEEV, S. N.; KAIS, S.; ALHARBI, F. H. Hydrogen Bonding and Stability of Hybrid Organic–Inorganic Perovskites. **ChemSusChem**, v. 9, n. 18, p. 2648–2655, 22 set. 2016.

EPERON, G. E.; STONE, K. H.; MUNDT, L. E.; SCHLOEMER, T. H.; HABISREUTINGER, S. N.; DUNFIELD, S. P.; SCHELHAS, L. T.; BERRY, J. J.; MOORE, D. T.; EPERON, G. E.; MOORE, D. T. The Role of Dimethylammonium in Bandgap Modulation for Stable Halide Perovskites. **ACS Energy Letters**, v. 5, n. 6, p. 1856–1864, 12 jun. 2020.

FABELO, O.; RODRÍGUEZ-VELAMAZÁN, J. A.; CANADILLAS-DELGADO, L.; MAZZUCA, L.; CAMPO, J.; MILLÁN, Á.; CHAPON, L. C.; RODRÍGUEZ-CARVAJAL, J.; MILLÁN, Á.; CHAPON, L. C.; RODRÍGUEZ-CARVAJAL, J. Origin of the magnetoelectric effect in the $Cs_2FeCl_5.D_2O$ compound. **Physical Review B**, v. 96, n. 104428, p. 1–9, 2017.

FAGHIHNASIRI, M.; IZADIFARD, M.; GHAZI, M. E. DFT Study of Mechanical Properties and Stability of Cubic Methylammonium Lead Halide Perovskites ($CH_3NH_3PbX_3$, X = I, Br, Cl). **Journal of Physical Chemistry C**, v. 121, n. 48, p. 27059–27070, 7 dez. 2017.

FIEBIG, M. Revival of the magnetoelectric effect. **Journal of Physics D: Applied Physics**, v. 38, n. 8, 21 abr. 2005.

FOP, S.; MCCOMBIE, K. S.; WILDMAN, E. J.; SKAKLE, J. M. S.; MCLAUGHLIN, A. C. Hexagonal perovskite derivatives: a new direction in the design of oxide ion conducting materials. **Chemical Communications**, v. 55, n. 15, p. 2127–2137, 2019.

FRANSSEN, W. M. J.; BRUIJNAERS, B. J.; PORTENGEN, V. H. L.; KENTGENS, A. P. M. Dimethylammonium Incorporation in Lead Acetate Based $MAPbI_3$ Perovskite Solar Cells. **ChemPhysChem**, v. 19, n. 22, p. 3107–3115, 19 nov. 2018.

FRANSSEN, W. M. J.; HEUMEN, C. M. M. VAN; KENTGENS, A. P. M. Structural Investigations of $MA_{1-x}DMA_xPbI_3$ Mixed-Cation Perovskites. **Inorganic Chemistry**, v. 59, n. 6, p. 3730–3739, 16 mar. 2020.

FREITAS, R. S.; PADUAN-FILHO, A.; BECERRA, C. C. Magnetic phase diagram of the low-anisotropy antiferromagnet $Cs_2FeCl_5.H_2O$. **Journal of Magnetism and Magnetic Materials**, v. 374, p. 307–310, 15 jan. 2015.

FRÖHLICH, T.; STEIN, J.; BOHATÝ, L.; BECKER, P.; GUKASOV, A.; BRADEN, M. Structural and magnetic phase transitions in $Cs_2[FeCl_5(H_2O)]$. **Journal of Physics: Condensed Matter**, v. 30, n. 29, p. 295403, 25 jul. 2018.

G. MATTNEY COLE; JR. CHARLES F. PUTNIK; SMITH L. HOLT. Physical Properties of Linear-Chain Systems. II. Optical Spectrum of $CsMnBr_3$. **Inorganic Chemistry**, v. 14, n. 9, p. 2219–2223, 1975.

GABAS, M.; PALACIO, F.; RODRIGUEZ-CARVAJAL, J.; VISSER, D. Magnetic structures of the three-dimensional Heisenberg antiferromagnets $K_2FeCl_5.D_2O$ and $Rb_2FeCl_5.D_2O$. **Journal of Physics: Condensed Matter**, v. 7, n. 24, p. 4725–4738, 12 jun. 1995.

GAO, W.; CHEN, C.; RAN, C.; ZHENG, H.; DONG, H.; XIA, Y.; CHEN, Y.; HUANG, W. A-Site Cation Engineering of Metal Halide Perovskites: Version 3.0 of Efficient Tin-Based Lead-Free Perovskite Solar Cells. **Advanced Functional Materials**, v. 30, n. 34, 1 ago. 2020.

GAO, Y. *et al.* Molecular engineering of organic–inorganic hybrid perovskites quantum wells. **Nature Chemistry**, v. 11, n. 12, p. 1151–1157, 11 dez. 2019.

GARCÍA-FERNÁNDEZ, A.; BERMÚDEZ-GARCÍA, J. M.; CASTRO-GARCÍA, S.; LLAMAS-SAIZ, A. L.; ARTIAGA, R.; LÓPEZ-BECEIRO, J.; HU, S.; REN, W.; STROPPA, A.; SÁNCHEZ-ANDÚJAR, M.; SEÑARÍS-RODRÍGUEZ, M. A. Phase Transition, Dielectric Properties, and Ionic Transport in the $[(CH_3)_2NH_2]PbI_3$ Organic-Inorganic Hybrid with 2H-Hexagonal Perovskite Structure. **Inorganic Chemistry**, v. 56, n. 9, p. 4918–4927, 1 maio 2017.

GARCÍA-FERNÁNDEZ, A.; BERMÚDEZ-GARCÍA, J. M.; CASTRO-GARCÍA, S.; LLAMAS-SAIZ, A. L.; ARTIAGA, R.; LÓPEZ-BECEIRO, J. J.; SÁNCHEZ-ANDÚJAR, M.; SEÑARÍS-RODRÍGUEZ, M. A. $[(CH_3)_2NH_2]_7Pb_4X_{15}$ (X = Cl^- and Br^-), 2D-Perovskite Related Hybrids with Dielectric Transitions and Broadband Photoluminiscent Emission. **Inorganic Chemistry**, v. 57, n. 6, p. 3215–3222, 19 mar. 2018.

GARCÍA-FERNÁNDEZ, A.; JUAREZ-PEREZ, E. J.; BERMÚDEZ-GARCÍA, J. M.; LLAMAS-SAIZ, A. L.; ARTIAGA, R.; LÓPEZ-BECEIRO, J. J.; SEÑARÍS-RODRÍGUEZ, M. A.; SÁNCHEZ-ANDÚJAR, M.; CASTRO-GARCÍA, S. Hybrid lead halide $[(CH_3)_2NH_2]PbX_3$ (X = Cl^- and Br^-) hexagonal perovskites with multiple functional properties. **Journal of Materials Chemistry C**, v. 7, n. 32, p. 10008–10018, 2019.

GARCÍA-FLORES, A. F.; GRANADO, E.; MARTINHO, H.; RETTORI, C.; GOLOVENCHITS, E. I.; SANINA, V. A.; OSEROFF, S. B.; PARK, S.; CHEONG, S. W. Magnetically frustrated behavior in multiferroics RMn_2O_5 (R=Bi, Eu, and Dy): A Raman scattering study. **Journal of Applied Physics**, v. 101, n. 9, 2007.

GARCÍA-FLORES, A. F.; GRANADO, E.; MARTINHO, H.; URBANO, R. R.; RETTORI, C.; GOLOVENCHITS, E. I.; SANINA, V. A.; OSEROFF, S. B.; PARK, S.; CHEONG, S. W. Anomalous phonon shifts in the paramagnetic phase of multiferroic RMn_2O_5 (R=Bi, Eu, Dy): Possible manifestations of unconventional magnetic correlations. **Physical Review B**, v. 73, n. 10, 2006.

GESELLE, M.; FUESS, H. Crystal structure of dimethylammonium tribromoplumbate(II), $(CH_3)_2NH_2PbBr_3$. **Zeitschrift für Kristallographie - New Crystal Structures**, v. 212, n. 1, p. 234, 1 dez. 1997.

GHOSH, R.; SPANO, F. C. Excitons and Polarons in Organic Materials. **Accounts of Chemical Research**, v. 53, n. 10, p. 2201–2211, 20 out. 2020.

GHOSH, S.; RANA, D.; PRADHAN, B.; DONFACK, P.; HOFKENS, J.; MATERNY, A. Vibrational study of lead bromide perovskite materials with variable cations based on Raman spectroscopy and density functional theory. **Journal of Raman Spectroscopy**, v. 52, n. 12, p. 2338–2347, 1 dez. 2021.

GIANNOZZI, P. *et al.* QUANTUM ESPRESSO: A modular and open-source software project for quantum simulations of materials. **Journal of Physics Condensed Matter**, v. 21, n. 39, 2009.

GIANNOZZI, P. *et al.* Advanced capabilities for materials modelling with Quantum ESPRESSO. **Journal of Physics Condensed Matter**, v. 29, n. 46, 24 out. 2017.

GOODWIN, A. L.; KEEN, D. A.; TUCKER, M. G. Large negative linear compressibility of $Ag_3[Co(CN)_6]$. **PNAS**, v. 105, n. 48, p. 18708–18713, 2008.

GRANADO, E.; GARCÍ, A.; SANJURJO, J. A.; RETTORI, C.; TORRIANI, I.; PRADO, F.; SÁ NCHEZ, R. D.; CANEIRO, A.; OSEROFF, S. B. Magnetic ordering effects in the Raman spectra of $La_{1-x}Mn_{1-x}O_3$. **Physical Review B**, v. 60, n. 17, p. 11879–11882, 1999.

GRANCINI, G.; NAZEERUDDIN, M. K. Dimensional tailoring of hybrid perovskites for photovoltaics. **Nature Reviews Materials**, v. 4, n. 1, p. 4–22, 28 nov. 2018.

GRECHKO, M.; BRETSCHNEIDER, S. A.; VIETZE, L.; KIM, H.; BONN, M. Vibrational Coupling between Organic and Inorganic Sublattices of Hybrid Perovskites. **Angewandte Chemie**, v. 130, n. 41, p. 13845–13849, 8 out. 2018.

GREEDAN, J. E.; HEWITT, D. C.; FAGGIANI, R.; BROWN, I. D. Structure of and hydrogen bonding in dicaesium aquapentachloroferrate(III). **Acta Crystallographica Section B Structural Crystallography and Crystal Chemistry**, v. 36, n. 8, p. 1927–1929, 1 ago. 1980.

GREEN, M. A.; DUNLOP, E. D.; HOHL-EBINGER, J.; YOSHITA, M.; KOPIDAKIS, N.; BOTHE, K.; HINKEN, D.; RAUER, M.; HAO, X. Solar cell efficiency tables (Version 60). **Progress in Photovoltaics: Research and Applications**, v. 30, n. 7, p. 687–701, 1 jul. 2022.

HAMANN, D. R. Optimized norm-conserving Vanderbilt pseudopotentials. **Physical Review B - Condensed Matter and Materials Physics**, v. 88, n. 8, 19 ago. 2013.

HAN, J. H.; SAMANTA, T.; PARK, Y. M.; CHO, H. BIN; MIN, J. W.; HWANG, S. J.; JANG, S. W.; IM, W. BIN. Effect of self-trapped excitons in the optical properties of manganese-alloyed hexagonal-phased metal halide perovskite. **Chemical Engineering Journal**, v. 450, 15 dez. 2022.

HAN, Y.; CHENG, X.; CUI, B. BIN. Factors influencing self-trapped exciton emission of low-dimensional metal halides. **Materials Advances**, v. 4 p. 355-372, 18 nov. 2022.

HARTER, J. W.; ZHAO, Z. Y.; YAN, J.-Q.; MANDRUS, D. G.; HSIEH, D. A parity-breaking electronic nematic phase transition in the spin-orbit coupled metal $Cd_2Re_2O_7$. **Science**, v. 356, n. 6335, p. 295–299, 21 abr. 2017.

HAUGHEY, D. P.; BEVERIDGE, G. S. G. Structural properties of packed beds - A review. **The Canadian Journal of Chemical Engineering**, v. 47, n. 2, p. 130–140, abr. 1969.

HE, L.; SHI, P. P.; ZHAO, M. M.; LIU, C. M.; ZHANG, W.; YE, Q. Emergent Chirality and Nonlinear Optical Switching in a Ferroelastic Molecular Perovskite Solid Solution. **Chemistry of Materials**, v. 33, n. 2, p. 799–805, 2021.

HOSOI, M.; MATSUURA, H.; OGATA, M. New magnetic phases in the chiral magnet $CsCuCl_3$ under high pressures. **Journal of the Physical Society of Japan**, v. 87, n. 7, 2018.

HOWARD, C. J.; STOKES, H. T. Group-Theoretical Analysis of Octahedral Tilting in Perovskites. **Acta Crystallographica Section B Structural Science**, v. 54, n. 6, p. 782–789, 1 dez. 1998.

HUANG, J.; YUAN, Y.; SHAO, Y.; YAN, Y. Understanding the physical properties of hybrid perovskites for photovoltaic applications. **Nature Reviews Materials**, v. 2, 4 jul. 2017.

HUGHEY, K. D.; LEE, M.; NAM, J.; CLUNE, A. J.; O'NEAL, K. R.; TIAN, W.; FISHMAN, R. S.; OZEROV, M.; LEE, J. H.; ZAPF, V. S.; MUSFELDT, J. L. High-Field Magnetoelectric and Spin-Phonon Coupling in Multiferroic $(NH_4)_2[FeCl_5{\cdot}(H_2O)]$. **Inorganic Chemistry**, v. 61, n. 8, p. 3434–3442, 28 fev. 2022.

IBACETA-JAÑA, J. *et al.* Vibrational dynamics in lead halide hybrid perovskites investigated by Raman spectroscopy. **Physical Chemistry Chemical Physics**, v. 22, n. 10, p. 5604–5614, 2020.

IVANTCHEV, S.; KROUMOVA, E.; AROYO, M. I.; PEREZ-MATO, J. M.; IGARTUA, J. M.; MADARIAGA, G.; WONDRATSCHEK, H. SUPERGROUPS - a computer program for the determination of the supergroups of the space groups. **J. Appl. Cryst**, v. 35, p. 511–512, 2002.

IVANTCHEV, S.; KROUMOVA, E.; MADARIAGA, G.; PÉREZ-MATO, J. M.; AROYO, M. I. SUBGROUPGRAPH: A computer program for analysis of group-subgroup relations between space groups. **Journal of Applied Crystallography**, v. 33, n. 4, p. 1190–1191, 2000.

JARA, E.; BARREDA-ARGÜESO, J. A.; GONZÁLEZ, J.; RODRÍGUEZ, F.; VALIENTE, R. Origin of the piezochromism in Cs_2CuCl_4: Electron-phonon and crystal-structure correlations. **Physical Review B**, v. 99, n. 13, 18 abr. 2019.

JEON, N. J.; NOH, J. H.; KIM, Y. C.; YANG, W. S.; RYU, S.; SEOK, S. IL. Solvent engineering for high-performance inorganic-organic hybrid perovskite solar cells. **Nature Materials**, v. 13, n. 9, p. 897–903, 2014.

JIN, S. Can We Find the Perfect A-Cations for Halide Perovskites? **ACS Energy Letters**, v. 6, n. 9, p. 3386–3389, 10 set. 2021.

JU, D.; ZHAO, T.; YANGYANG, D.; ZHANG, G.; HU, X.; CUI, D.; TAO, X. Gas induced conversion of hybrid perovskite single crystal to single crystal for great enhancement of their photoelectric properties. **Journal of Materials Chemistry A**, v. 5, n. 41, p. 21919–21925, 2017.

KAMBLI, U.; GIIDEL, H. U. Optical absorption and luminescence studies of antiferromagnetic $RbMnCl_3$ and $CsMnCl_3$. **Journal of Physics C: Solid State Physics**, v. 17, p. 4041–4054, 1984.

KATSURA, T.; TANGE, Y. A simple derivation of the Birch–Murnaghan equations of state (EOSs) and comparison with EOSs derived from other definitions of finite strain. **Minerals**, v. 9, n. 12, 1 dez. 2019.

KE, W.; SPANOPOULOS, I.; STOUMPOS, C. C.; KANATZIDIS, M. G. Myths and reality of $HPbI_3$ in halide perovskite solar cells. **Nature Communications**, v. 9, n. 1, 1 dez. 2018.

KIESLICH, G.; SKELTON, J. M.; ARMSTRONG, J.; WU, Y.; WEI, F.; SVANE, K. L.; WALSH, A.; BUTLER, K. T. Hydrogen Bonding versus Entropy: Revealing the Underlying Thermodynamics of the Hybrid Organic–Inorganic Perovskite $[CH_3NH_3]PbBr_3$. **Chemistry of Materials**, v. 30, n. 24, p. 8782–8788, 26 dez. 2018.

KIM, B.; KIM, M.; KIM, H.; JEONG, S.; YANG, J.; JEONG, M. S. Improved Stability of $MAPbI_3$ Perovskite Solar Cells Using Two-Dimensional Transition-Metal Dichalcogenide Interlayers. **ACS Applied Materials & Interfaces**, v. 14, n. 31, p. 35726–35733, 10 ago. 2022.

KLEMENT, P.; DEHNHARDT, N.; DONG, C. D.; DOBENER, F.; BAYLIFF, S.; WINKLER, J.; HOFMANN, D. M.; KLAR, P. J.; SCHUMACHER, S.; CHATTERJEE, S.; HEINE, J. Atomically Thin Sheets of Lead-Free 1D Hybrid Perovskites Feature Tunable White-Light Emission from Self-Trapped Excitons. **Advanced Materials**, v. 33, n. 23, 1 jun. 2021.

KONTOS, A. G.; MANOLIS, G. K.; KALTZOGLOU, A.; PALLES, D.; KAMITSOS, E. I.; KANATZIDIS, M. G.; FALARAS, P. Halogen–NH_2^+ Interaction, Temperature-Induced Phase Transition, and Ordering in $(NH_2CHNH_2)PbX_3$ (X = Cl, Br, I) Hybrid Perovskites. **The Journal of Physical Chemistry C**, v. 124, n. 16, p. 8479–8487, 23 abr. 2020.

KOTHANDARAMAN, R. K.; JIANG, Y.; FEURER, T.; TIWARI, A. N.; FU, F. Near-Infrared-Transparent Perovskite Solar Cells and Perovskite-Based Tandem Photovoltaics. **Small Methods**, v. 4, n. 10, 1 out. 2020.

KROESE, C. J.; MAASKANT, W. J. A. The relation between the high-temperature and room-temperature structure of $CsCuCl_3$. **Chemical Physics**, v. 5, n. 2, p. 224–233, ago. 1974.

KROUMOVA, E.; AROYO, M. L.; PEREZ-MATO, J. M.; KIROV, A.; CAPILLAS, C.; IVANTCHEV, S.; WONDRATSCHEK, H. Bilbao Crystallographic Server: Useful databases and tools for phase-transition studies. **Phase Transitions**, v. 76, n. 1–2, p. 155–170, 1 jan. 2003.

LA FLOR, G. DE; OROBENGOA, D.; TASCI, E.; PEREZ-MATO, J. M.; AROYO, M. I. Comparison of structures applying the tools available at the Bilbao Crystallographic Server. **Journal of Applied Crystallography**, v. 49, p. 653–664, 2016.

LAVAN, S. N.; SANNI, A. M.; RURY, A. S.; LIU, Z. F. Characterization of the Ammonium Bending Vibrations in Two-Dimensional Hybrid Lead-Halide Perovskites from Raman Spectroscopy and First-Principles Calculations. **Journal of Physical Chemistry C**, v. 125, n. 1, p. 223–236, 14 jan. 2021.

LEE, M. Magnetic phase diagram of $A_2[FeCl_5(H_2O)]$ (A = K, Rb, NH_4). **Journal of Magnetism and Magnetic Materials**, v. 555, p. 169302, 1 ago. 2022.

LEE, M. V.; RAGA, S. R.; KATO, Y.; LEYDEN, M. R.; ONO, L. K.; WANG, S.; QI, Y. Transamidation of dimethylformamide during alkylammonium lead triiodide film formation for perovskite solar cells. **Journal of Materials Research**, v. 32, n. 1, p. 45–55, 13 jan. 2017.

LEE, S. J.; CHOI, M. Y.; LIM, A. R. Effect of Methylene Chain Length on the Thermodynamic Properties, Ferroelastic Properties, and Molecular Dynamics of the Perovskite-type Layer Crystal $[NH_3(CH_2)_n NH_3]MnCl_4$ (n = 2, 3, and 4). **ACS Omega**, v. 6, n. 23, p. 15392–15399, 15 jun. 2021.

LEGUY, A. M. A. *et al.* Dynamic disorder, phonon lifetimes, and the assignment of modes to the vibrational spectra of methylammonium lead halide perovskites. **Physical Chemistry Chemical Physics**, v. 18, n. 39, p. 27051–27066, 2016.

LI, Q.; CHEN, Z.; YANG, B.; TAN, L.; XU, B.; HAN, J.; ZHAO, Y.; TANG, J.; QUAN, Z. Pressure-Induced Remarkable Enhancement of Self-Trapped Exciton Emission in One-Dimensional $CsCu_2I_3$ with Tetrahedral Units. **Journal of the American Chemical Society**, v. 142, n. 4, p. 1786–1791, 29 jan. 2020.

LI, S.; LUO, J.; LIU, J.; TANG, J. Self-Trapped Excitons in All-Inorganic Halide Perovskites: Fundamentals, Status, and Potential Applications. **Journal of Physical Chemistry Letters**,v. 10, n. 8, p. 1999-2007, 18 abr. 2019.

LI, T.-I.; STUCKY, G. D. Exchange Interactions in Polynuclear Transition Metal Complexes. Structural Properties of Cesium Tribromocuprate(II), $CsCuBr_3$, a Strongly Coupled Copper(I1) System. **Inorganic Chemistry**, v. 12, n. 2, p. 441–445, 1973.

LIANG, T. *et al.* Experimental study on thermal expansion coefficient of composite multi-layered flaky gun propellants. **Composites Part B: Engineering**, v. 166, p. 428–435, 1 jun. 2019.

LIN, J. *et al.* Thermochromic halide perovskite solar cells. **Nature Materials**, v. 17, n. 3, p. 261–267, 1 mar. 2018.

LINABURG, M. R.; MCCLURE, E. T.; MAJHER, J. D.; WOODWARD, P. M. $Cs_{1-x}Rb_xPbCl_3$ and $Cs_{1-x}Rb_xPbBr_3$ Solid Solutions: Understanding Octahedral Tilting in Lead Halide Perovskites. **Chemistry of Materials**, v. 29, n. 8, p. 3507–3514, 25 abr. 2017.

LIU, S.; DU, Y. W.; TSO, C. Y.; LEE, H. H.; CHENG, R.; FENG, S. P.; YU, K. M. Organic Hybrid Perovskite ($MAPbI_{3-x}Cl_x$) for Thermochromic Smart Window with Strong Optical Regulation Ability, Low Transition Temperature, and Narrow Hysteresis Width. **Advanced Functional Materials**, v. 31, n. 26, 1 jun. 2021.

LIU, Y.; LIU, Q.; LIU, YING; JIANG, X.; ZHANG, X.; ZHAO, J. Effects of spin-phonon coupling on two-dimensional ferromagnetic semiconductors: A case study of iron and ruthenium trihalides. **Nanoscale**, v. 13, n. 16, p. 7714–7722, 28 abr. 2021.

LU, Y.; LI, G.; FU, S.; FANG, S.; LI, L. $CsCu_2I_3$ Nanocrystals: Growth and Structural Evolution for Tunable Light Emission. **ACS Omega**, v. 6, n. 1, p. 544–552, 12 jan. 2021.

LU, Y.; QU, K.; ZHANG, T.; HE, Q.; PAN, J. Metal Halide Perovskite Nanowires: Controllable Synthesis, Mechanism, and Application in Optoelectronic Devices. **Nanomaterials**, v. 13, n. 3, p. 419, 19 jan. 2023.

LUZÓN, J.; CAMPO, J.; PALACIO, F.; MCINTYRE, G. J.; MILLÁN, A. Understanding magnetic interactions in the series $A_2FeX_5.H_2O$ (A=K, Rb; X=Cl, Br). I. Spin densities by polarized neutron diffraction and DFT calculations. **Physical Review B - Condensed Matter and Materials Physics**, v. 78, n. 5, 11 ago. 2008.

MACRAE, C. F.; SOVAGO, I.; COTTRELL, S. J.; GALEK, P. T. A.; PIDCOCK, E.; PLATINGS, M.; SHIELDS, G. P.; STEVENS, J. S.; TOWLER, M.; WOOD, P. A. Mercury 4.0: from visualization to analysis , design and prediction. **Journal of Applied Crystallography**, p. 226–235, 2020.

MĄCZKA, MIROSŁAW; GĄGOR, A.; MACALIK, B.; PIKUL, A.; PTAK, M.; HANUZA, J. Order-disorder transition and weak ferromagnetism in the perovskite metal formate frameworks of $[(CH_3)_2NH_2][M(HCOO)_3]$ and $[(CH_3)_2ND_2][M(HCOO)_3]$ (M = Ni, Mn). **Inorganic Chemistry**, v. 53, n. 1, p. 457–467, 6 jan. 2014.

MĄCZKA, M.; PTAK, M. Temperature-Dependent Raman Studies of $FAPbBr_3$ and $MAPbBr_3$ Perovskites: Effect of Phase Transitions on Molecular Dynamics and Lattice Distortion. **Solids**, v. 3, n. 1, p. 111–121, 19 fev. 2022.

MĄCZKA, M.; PTAK, M.; VASCONCELOS, D. L. M.; GIRIUNAS, L.; FREIRE, P. T. C.; BERTMER, M.; BANYS, J.; SIMENAS, M. NMR and Raman Scattering Studies of Temperature- and Pressure-Driven Phase Transitions in $CH_3NH_2NH_2PbCl_3$ Perovskite. **The Journal of Physical Chemistry C**, v. 124, n. 49, p. 26999–27008, 10 dez. 2020.

MĄCZKA, M.; ZIERKIEWICZ, W.; MICHALSKA, D.; HANUZA, J. Vibrational properties and DFT calculations of the perovskite metal formate framework of $[(CH_3)_2NH_2][Ni(HCOO_3)]$ system. **Spectrochimica Acta - Part A: Molecular and Biomolecular Spectroscopy**, v. 128, p. 674–680, 15 jul. 2014.

MAJZLAN, J.; TANGEMAN, J. A.; DACHS, E. Heat capacity, entropy, configurational entropy, and viscosity of magnesium silicate glasses and liquids. **Physics and Chemistry of Minerals**, v. 48, n. 8, p. 28, 19 ago. 2021.

MANCINI, A.; QUADRELLI, P.; AMOROSO, G.; MILANESE, C.; BOIOCCHI, M.; SIRONI, A.; PATRINI, M.; GUIZZETTI, G.; MALAVASI, L. Synthesis, structural and optical characterization of $APbX_3$ (A=methylammonium, dimethylammonium, trimethylammonium; X=I, Br, Cl) hybrid organic-inorganic materials. **Journal of Solid State Chemistry**, v. 240, p. 55–60, 1 ago. 2016.

MAO, L.; STOUMPOS, C. C.; KANATZIDIS, M. G. Two-Dimensional Hybrid Halide Perovskites: Principles and Promises. **Journal of the American Chemical Society**, v. 141, n. 3, p. 1171–1190, 23 jan. 2019.

MCCALL, K. M.; STOUMPOS, C. C.; KOSTINA, S. S.; KANATZIDIS, M. G.; WESSELS, B. W. Strong Electron-Phonon Coupling and Self-Trapped Excitons in the Defect Halide Perovskites $A_3M_2I_9$ (A = Cs, Rb; M = Bi, Sb). **Chemistry of Materials**, v. 29, n. 9, p. 4129–4145, 9 maio 2017.

MCCARTHY, P. J.; WALKER, I. M. Water overtone and combination bands in the near-infrared spectrum of $M_2FeCl_5.H_2O$ (M = Cs, K) at cryogenic temperatures. **Spectrochimica Acta Part A: Molecular Spectroscopy**, v. 39, n. 9, p. 827–834, 1983.

MCKINNON, J. J.; JAYATILAKA, D.; SPACKMAN, M. A. Towards quantitative analysis of intermolecular interactions with Hirshfeld surfaces. **Chemical Communications**, n. 37, p. 3814–3816, 2007.

MCMEEKIN, D. P. *et al.* Intermediate-phase engineering via dimethylammonium cation additive for stable perovskite solar cells. **Nature Materials**, v. 22, n. 1, p. 73–83, 1 jan. 2023.

MENAHEM, M.; DAI, Z.; AHARON, S.; SHARMA, R.; ASHER, M.; DISKIN-POSNER, Y.; KOROBKO, R.; RAPPE, A. M.; YAFFE, O. Strongly Anharmonic Octahedral Tilting in Two-Dimensional Hybrid Halide Perovskites. **ACS Nano**, v. 15, n. 6, p. 10153–10162, 22 jun. 2021.

MENG, H.; SHAO, Z.; WANG, L.; LI, Z.; LIU, R.; FAN, Y.; CUI, G.; PANG, S. Chemical Composition and Phase Evolution in DMAI-Derived Inorganic Perovskite Solar Cells. **ACS Energy Letters**, v. 5, n. 1, p. 263–270, 10 jan. 2020.

MIROSŁAW MĄCZKA; PIETRASZKO, A.; MACALIK, B.; HERMANOWICZ, K. Structure, phonon properties, and order-disorder transition in the metal formate framework of $[NH_4][Mg(HCOO)_3]$. **Inorganic Chemistry**, v. 53, n. 2, p. 787–794, 21 jan. 2014.

MIYAKE, A.; SHIBUYA, J.; AKAKI, M.; TANAKA, H.; TOKUNAGA, M. Magnetic field induced polar phase in the chiral magnet $CsCuCl_3$. **Physical Review B**, v. 92, n. 10, 17 set. 2015.

MOMMA, K.; IZUMI, F. VESTA3 for three-dimensional visualization of crystal , volumetric and morphology data. **Journal of Applied Crystallography**, p. 1272–1276, 2011.

MOONEY, J.; KAMBHAMPATI, P. Get the basics right: Jacobian conversion of wavelength and energy scales for quantitative analysis of emission spectra. **Journal of Physical Chemistry Letters**, v. 4, n. 19, p. 3316–3318, 2013.

MUNSON, K. T.; KENNEHAN, E. R.; DOUCETTE, G. S.; ASBURY, J. B. Dynamic Disorder Dominates Delocalization, Transport, and Recombination in Halide Perovskites. **Chem**, v. 4, n. 12, p. 2826–2843, 13 dez. 2018.

NAKADA, K.; MATSUMOTO, Y.; SHIMOI, Y.; YAMADA, K.; FURUKAWA, Y. Temperature-dependent evolution of Raman spectra of methylammonium lead halide perovskites, $CH_3NH_3PbX_3$ (X = I, Br). **Molecules**, v. 24, n. 3, 11 fev. 2019.

NAM-GYU PARK; MICHAEL GRÄTZEL; TSUTOMU MIYASAKA. **Organic-Inorganic Halide Perovskite Photovoltaics**. Springer ed. Cham: Springer International Publishing, 2016.

NATAF, L.; AGUADO, F.; HERNÁNDEZ, I.; VALIENTE, R.; GONZÁLEZ, J.; SANZ-ORTIZ, M. N.; WILHELM, H.; JEPHCOAT, A. P.; BAUDELET, F.; RODRÍGUEZ, F. Volume and pressure dependences of the electronic, vibrational, and crystal structures of Cs_2CoCl_4: Identification of a pressure-induced piezochromic phase at high pressure. **Physical Review B**, v. 95, n. 1, 24 jan. 2017.

NGUYEN, L. T.; CAVA, R. J. Hexagonal Perovskites as Quantum Materials. **Chemical Reviews**, v. 121, n. 5, p. 2935–2965, 10 mar. 2021.

NIEMANN, R. G.; KONTOS, A. G.; PALLES, D.; KAMITSOS, E. I.; KALTZOGLOU, A.; BRIVIO, F.; FALARAS, P.; CAMERON, P. J. Halogen Effects on Ordering and Bonding of $CH_3NH_3^+$ in $CH_3NH_3PbX_3$ (X = Cl, Br, I) Hybrid Perovskites: A Vibrational Spectroscopic Study. **The Journal of Physical Chemistry C**, v. 120, n. 5, p. 2509–2519, 11 fev. 2016.

NIHONGI, K.; KIDA, T.; NARUMI, Y.; ZACCARO, J.; KOUSAKA, Y.; INOUE, K.; KINDO, K.; UWATOKO, Y.; HAGIWARA, M. Magnetic field and pressure phase diagrams of the triangular-lattice antiferromagnet $CsCuCl_3$ explored via magnetic susceptibility measurements with a proximity-detector oscillator. **Physical Review B**, v. 105, n. 18, 1 maio 2022.

OCTAVIO DE ARAUJO, L.; RÊGO, C. R. C.; WENZEL, W.; SABINO, F. P.; GUEDES-SOBRINHO, D. Impact of the Polymorphism and Relativistic Effects on the Electronic Properties of Inorganic Metal Halide Perovskites. **The Journal of Physical Chemistry C**, v. 126, n. 4, p. 2131–2140, 3 fev. 2022.

PALMER, DAVIDC.; BISMAYER, U.; SALJE, EKHARDK. H. Phase transitions in leucite: Order parameter behaviour and the Landau potential deduced from Raman spectroscopy and birefringence studies. **Physics and Chemistry of Minerals**, v. 17, n. 3, p. 259–265, jun. 1990.

PAN, F.; LI, J.; MA, X.; NIE, Y.; LIU, B.; YE, H. Free and self-trapped exciton emission in perovskite $CsPbBr_3$ microcrystals. **RSC Advances**, v. 12, n. 2, p. 1035–1042, 5 jan. 2022.

PARK, N. G. Organometal perovskite light absorbers toward a 20% efficiency low-cost solid-state mesoscopic solar cell. **Journal of Physical Chemistry Letters**, v. 4, n. 15, p. 2423–2429, 1 ago. 2013.

PARKER, S. F.; SHANKLAND, K.; SPURNT, J. C.; JAYASOORIYA, U. A. The nine modes of complexed water. **Spectrochimica Acta - Part A: Molecular and Biomolecular Spectroscopy**, v. 53, n. 13, p. 2333–2339, 1997.

PEI, Y.; LIU, Y.; LI, F.; BAI, S.; JIAN, X.; LIU, M. Unveiling Property of Hydrolysis-Derived $DMAPbI_3$ for Perovskite Devices: Composition Engineering, Defect Mitigation, and Stability Optimization. **iScience**, v. 15, p. 165–172, 31 maio 2019.

PERDEW, J. P.; BURKE, K.; ERNZERHOF, M. Generalized Gradient Approximation Made Simple. **Physical Review Letters**, v. 77, n. 18, 1996.

PÉREZ-OSORIO, M. A.; LIN, Q.; PHILLIPS, R. T.; MILOT, R. L.; HERZ, L. M.; JOHNSTON, M. B.; GIUSTINO, F. Raman Spectrum of the Organic-Inorganic Halide Perovskite $CH_3NH_3PbI_3$ from First Principles and High-Resolution Low-Temperature Raman Measurements. **Journal of Physical Chemistry C**, v. 122, n. 38, p. 21703–21717, 27 set. 2018.

PÉREZ-OSORIO, M. A.; MILOT, R. L.; FILIP, M. R.; PATEL, J. B.; HERZ, L. M.; JOHNSTON, M. B.; GIUSTINO, F. Vibrational Properties of the Organic–Inorganic Halide Perovskite $CH_3NH_3PbI_3$ from Theory and Experiment: Factor Group Analysis, First-

Principles Calculations, and Low-Temperature Infrared Spectra. **The Journal of Physical Chemistry C**, v. 119, n. 46, p. 25703–25718, 19 nov. 2015.

PESIN, D.; BALENTS, L. Mott physics and band topology in materials with strong spin-orbit interaction. **Nature Physics**, v. 6, n. 5, p. 376–381, 2010.

PETZELT, J.; GREGORA, I.; VORLIIIEK, V.; FOUSEK, J.; BIEZINA, B.; KOZLOV, G. V.; VOLKOV, A. A. Far-infrared and Raman Spectroscopy of the Phase Transition in $CsCuCl_3$. **Journal of Raman Spectroscopy**, v. 10, p. 187–193, 1981.

PISZCZEK, P.; GRODZICKI, A.; ENGELEN, B. Infrared and Raman studies of water molecule normal vibrations in crystalline hydrates which form the chain structures. **Journal of Molecular Structure**, v. 646, p. 45–54, 2003.

PLAKHTY, V. P.; WOSNITZA, J.; MARTIN, N.; MARCHI, Y.; SMIRNOV, O. P.; GRENIER, B.; GAVRILOV, S. V. Isostructural transition coupled with spin ordering in CsCuCl3: A spatially frustrated spiral crystal lattice. **Physical Review B**, v. 79, n. 1, 5 jan. 2009.

PRESCHER, C.; PRAKAPENKA, V. B. DIOPTAS: A program for reduction of two-dimensional X-ray diffraction data and data exploration. **High Pressure Research**, v. 35, n. 3, p. 223–230, 3 jul. 2015.

PROSNIKOV, M. A.; SMIRNOV, A. N.; DAVYDOV, V. Y.; PISAREV, R. V.; LYUBOCHKO, N. A.; BARILO, S. N. Magnetic dynamics and spin-phonon coupling in the antiferromagnet Ni_2NbBO_6. **Physical Review B**, v. 98, n. 10, 4 set. 2018.

PROTESESCU, L.; YAKUNIN, S.; BODNARCHUK, M. I.; KRIEG, F.; CAPUTO, R.; HENDON, C. H.; YANG, R. X.; WALSH, A.; KOVALENKO, M. V. Nanocrystals of Cesium Lead Halide Perovskites ($CsPbX_3$, X = Cl, Br, and I): Novel Optoelectronic Materials Showing Bright Emission with Wide Color Gamut. **Nano Letters**, v. 15, n. 6, p. 3692–3696, 10 jun. 2015.

QIN, G.; WANG, H.; ZHANG, L.; QIN, Z.; HU, M. Giant effect of spin-lattice coupling on the thermal transport in two-dimensional ferromagnetic CrI_3. **Journal of Materials Chemistry C**, v. 8, n. 10, p. 3520–3526, 14 mar. 2020.

QUARTI, C.; GRANCINI, G.; MOSCONI, E.; BRUNO, P.; BALL, J. M.; LEE, M. M.; SNAITH, H. J.; PETROZZA, A.; ANGELIS, F. DE. The raman spectrum of the $CH_3NH_3PbI_3$ hybrid perovskite: Interplay of theory and experiment. **Journal of Physical Chemistry Letters**, v. 5, n. 2, p. 279–284, 16 jan. 2014.

RAKITA, Y.; COHEN, S. R.; KEDEM, N. K.; HODES, G.; CAHEN, D. Mechanical properties of $APbX_3$ (A = Cs or CH_3NH_3; X = i or Br) perovskite single crystals. **MRS Communications**, v. 5, n. 4, p. 623–629, 16 set. 2015.

ROCCANOVA, R.; YANGUI, A.; SEO, G.; CREASON, T. D.; WU, Y.; KIM, D. Y.; DU, M. H.; SAPAROV, B. Bright Luminescence from Nontoxic $CsCu_2X_3$ (X = Cl, Br, I). **ACS Materials Letters**, v. 1, n. 4, p. 459–465, 7 out. 2019.

RODRÍGUEZ-HERNÁNDEZ, J. S.; MAYRA, M. A.; ABREU, D. S.; NONATO, A.; SILVA, R. X. DA; GARCÍA-FERNÁNDEZ, A.; SEÑARÍS-RODRÍGUEZ, M. A.;

SÁNCHEZ-ANDÚJAR, M.; AYALA, A. P.; PASCHOAL, C. W. A. Uniaxial negative thermal expansion in the $[(CH_3)_2NH_2]PbBr_3$ hybrid perovskite. **Journal of Materials Chemistry C**, v. 10, n. 46, p. 17567–17576, 17 out. 2022.

RODRÍGUEZ-LAZCANO, Y.; NATAF, L.; RODRÍGUEZ, F. Electronic structure and luminescence of $[(CH_3)_4N]_2MnX_4$ (X=Cl,Br) crystals at high pressures by time-resolved spectroscopy: Pressure effects on the Mn-Mn exchange coupling. **Physical Review B**, v. 085115, n. 8, p. 1–11, 24 ago. 2009.

RODRÍGUEZ-VELAMAZÁN, J. A.; FABELO, O.; CAMPO, J.; MILLÁN, Á.; RODRÍGUEZ-CARVAJAL, J.; CHAPON, L. C. Magnetic-field-induced change of magnetoelectric coupling in the hybrid multiferroic $(ND_4)_2[FeCl_5 \cdot D_2O]$. **Physical Review B**, v. 95, n. 17, p. 174439, 26 maio 2017.

RODRÍGUEZ-VELAMAZÁN, J. A.; FABELO, O.; CAMPO, J.; RODRÍGUEZ-CARVAJAL, J.; QURESHI, N.; CHAPON, L. C. Switching of the Chiral Magnetic Domains in the Hybrid Molecular/Inorganic Multiferroic $(ND_4)_2[FeCl_5(D_2O)]$. **Scientific Reports**, v. 8, n. 1, 1 dez. 2018.

ROK, M.; BATOR, G.; ZARYCHTA, B.; DZIUK, B.; REPEĆ, J.; MEDYCKI, W.; ZAMPONI, M.; USEVIČIUS, G.; ŠIMENAS, M.; BANYS, J. Isostructural phase transition, quasielastic neutron scattering and magnetic resonance studies of a bistable dielectric ion-pair crystal $[(CH_3)_2NH_2]_2KCr(CN)_6$. **Dalton Transactions**, v. 48, n. 13, p. 4190–4202, 2019.

ROUSSEAU, D. L.; BAUMAN, R. P.; PORTO, S. P. S. Normal Mode Determination in Crystals. **Journal of Raman Spectroscopy**, v. 10, p. 253–290, 1981.

ROY, A.; ULLAH, H.; GHOSH, A.; BAIG, H.; SUNDARAM, S.; TAHIR, A. A.; MALLICK, T. K. Understanding the Semi-Switchable Thermochromic Behavior of Mixed Halide Hybrid Perovskite Nanorods. **Journal of Physical Chemistry C**, v. 125, n. 32, p. 18058–18070, 19 ago. 2021.

SALJE, E. K. **Phase Transitions in Ferroelastic and Co-elastic Crystals: An introduction for mineralogists, Material scientists and physicists**. v.2, 22 abr. 1993

SALJE, E. K. H.; BISMAYER, U. Hard mode spectroscopy: The concept and applications. **Phase Transitions**, v. 63, n. 1–4, p. 1–75, 19 nov. 1997.

SALJE, E. K. H.; HAYWARD, S. A.; LEE, W. T. Ferroelastic phase transitions: Structure and microstructure. **Acta Crystallographica Section A: Foundations of Crystallography**, v. 61, n. 1, p. 3–18, 2005.

SAMANTARAY, R.; CLARK, R. J.; CHOI, E. S.; DALAL, N. S. Elucidating the mechanism of multiferroicity in $(NH_4)_3Cr(O_2)_4$ and its tailoring by alkali metal substitution. **Journal of the American Chemical Society**, v. 134, n. 38, p. 15953–15962, 26 set. 2012.

SAPRIEL, J. Domain-wall orientations in ferroelastics. **Physical Review B**, v. 12, n. 11, p. 5128–5140, 1975.

SATA, N.; SHEN, G.; RIVERS, M. L.; SUTTON, S. R. Pressure-volume equation of state of the high-pressure (formula presented) phase of NaCl. **Physical Review B**, v. 65, n. 10, p. 1–7, 2002.

SCHLAAK, M.; COUZI, M.; HUONG, P. V. Reorientational Motions in Crystalline $(CH_3)_3NHCl$, Studied by Raman Spectroscopy. **Berichte der Bunsengesellschaft für physikalische Chemie**, v. 80, n. 9, p. 881–886, set. 1976.

SCHMIDT-MENDE, L. *et al.* Roadmap on organic–inorganic hybrid perovskite semiconductors and devices. **APL Materials**, v. 9, n. 10, p. 109202, 1 out. 2021.

SCOTT, J. F. Soft-mode spectroscopy: Experimental studies of structural phase transitions. **Reviews of Modern Physics**, v. 46, n. 1, p. 83–128, 1 jan. 1974.

SERA, A.; KOUSAKA, Y.; AKIMITSU, J.; SERA, M.; INOUE, K. Pressure-induced quantum phase transitions in the S = 1/2 triangular lattice antiferromagnet $CsCuCl_3$. **Physical Review B**, v. 96, n. 1, 14 jul. 2017.

SHARMA, S. K.; PANDYA, D. K. Laser-Raman spectra of crystalline $(NH_4)_2FeCl_5.H_2O$, $K_2FeCl_5.H_2O$ and $K_2FeCl_5.D_2O$. **Journal of Inorganic and Nuclear Chemistry**, v. 36, n. 5, p. 1165–1166, 1974.

SHELDRICK, G. M. SHELXT. Integrated space-group and crystal- structure determination research papers. **Acta Crystallographica Section A Foundations and Advances**, p. 3–8, 2015a.

SHELDRICK, G. M. SHELXT. Crystal structure refinement with SHELXL. **Acta Crystallographica Section C Structural Chemistry**, n. Md, p. 3–8, 2015b.

SHEN, G. *et al.* Toward an international practical pressure scale: A proposal for an IPPS ruby gauge (IPPS-Ruby2020). **High Pressure Research**, p. 299–314, 2020.

SHI, B.; DUAN, L.; ZHAO, Y.; LUO, J.; ZHANG, X. Semitransparent Perovskite Solar Cells: From Materials and Devices to Applications. **Advanced Materials**, v.32, n. 3, p. 1806474, 1 jan. 2020.

SHI, Y.; MA, Z.; ZHAO, DI.; CHEN, Y.; CAO, Y.; WANG, K.; XIAO, G.; ZOU, B. Pressure-Induced Emission (PIE) of One-Dimensional Organic Tin Bromide Perovskites. **Journal of the American Chemical Society**, v. 141, n. 16, p. 6504–6508, 24 abr. 2019.

SHI, Y.; ZHAO, W.; MA, Z.; XIAO, G.; ZOU, B. Self-trapped exciton emission and piezochromism in conventional 3D lead bromide perovskite nanocrystals under high pressure. **Chemical Science**, v. 12, n. 44, p. 14711–14717, 28 nov. 2021.

SHI, Z.; FANG, Z.; WU, J.; CHEN, Y.; MI, Q. Order–disorder transition of a rigid cage cation embedded in a cubic perovskite. **Nature Communications**, v. 12, n. 1, 1 dez. 2021.

SHI, ZEJIAO; GUO, J.; CHEN, Y.; LI, Q.; PAN, Y.; ZHANG, H.; XIA, Y.; HUANG, W. Lead-Free Organic-Inorganic Hybrid Perovskites for Photovoltaic Applications: Recent Advances and Perspectives. **Advanced Materials**, v. 29, n. 16, p. 1605005, 25 abr. 2017.

SHI, ZHIFANG; ZHANG, Y.; CUI, C.; LI, B.; ZHOU, W.; NING, Z.; MI, Q. Symmetrization of the Crystal Lattice of $MAPbI_3$ Boosts the Performance and Stability of Metal–Perovskite Photodiodes. **Advanced Materials**, v. 29, n. 30, 11 ago. 2017.

SILVA, R. X. DA; PASCHOAL, C. W. DE A.; SANTOS, C. C. DOS; GARCÍA-FERNÁNDEZ, A.; SALGADO-BECEIRO, J.; SEÑARÍS-RODRÍGUEZ, M. A.; SANCHEZ-

ANDUJAR, M.; SILVA, A. N. A. DE A. Raman spectroscopy studies on the barocaloric hybrid perovskite $[(CH_3)_4N][Cd(N_3)_3]$. **Molecules**, v. 25, n. 20, 1 out. 2020.

SILVA, R. X.; REICHLOVA, H.; MARTI, X.; BARBOSA, D. A. B.; LUFASO, M. W.; ARAUJO, B. S.; AYALA, A. P.; PASCHOAL, C. W. A. Spin-phonon coupling in $Gd(Co_{1/2}Mn_{1/2})O_3$ perovskite. **Journal of Applied Physics**, v. 114, n. 19, 21 nov. 2013.

SIMENAS, M. *et al.* Suppression of phase transitions and glass phase signatures in mixed cation halide perovskites. **Nature Communications**, v. 11, n. 1, 1 dez. 2020.

SMIRNOV, L. S.; NATKANIEC, I.; BELUSHKIN, A. B.; SMITH, D.; PRAGER, M. Features of the structure and dynamics of $Me_{1-x}(NH4)_xSCN$ (Me = K, Rb) mixed crystals. **Journal of Surface Investigation. X-ray, Synchrotron and Neutron Techniques**, v. 3, n. 6, p. 847–856, 16 dez. 2009.

SOHN, C. H.; KIM, C. H.; SANDILANDS, L. J.; HIEN, N. T. M.; KIM, S. Y.; PARK, H. J.; KIM, K. W.; MOON, S. J.; YAMAURA, J.; HIROI, Z.; NOH, T. W. Strong Spin-Phonon Coupling Mediated by Single Ion Anisotropy in the All-In-All-Out Pyrochlore Magnet $Cd_2Os_2O_7$. **Physical Review Letters**, v. 118, n. 11, 13 mar. 2017.

SON, J.; PARK, B. C.; KIM, C. H.; CHO, H.; KIM, S. Y.; SANDILANDS, L. J.; SOHN, C.; PARK, J. G.; MOON, S. J.; NOH, T. W. Unconventional spin-phonon coupling via the Dzyaloshinskii–Moriya interaction. **npj Quantum Materials**, v. 4, n. 1, 1 dez. 2019.

SPALDIN, N. A.; FIEBIG, M. The Renaissance of Magnetoelectric Multiferroics. **Science**, v. 309, n. July, p. 391–392, 2005.

SPALDIN, N. A.; RAMESH, R. Advances in magnetoelectric multiferroics. **Nature Materials**, v. 18, n. 3, p. 203–212, 1 mar. 2019.

SPEK, A. L. Single-crystal structure validation with the program PLATON. **J. Appl. Cryst**, v. 36, p. 7–13, 2003.

SPIRITO, D.; ASENSIO, Y.; HUESO, L. E.; MARTÍN-GARCÍA, B. Raman spectroscopy in layered hybrid organic-inorganic metal halide perovskites. **JPhys Materials**, v. 5, n. 3, 1 jul. 2022.

STEELE, J. A.; LAI, M.; ZHANG, Y.; LIN, Z.; HOFKENS, J.; ROEFFAERS, M. B. J.; YANG, P. Phase Transitions and Anion Exchange in All-Inorganic Halide Perovskites. **Accounts of Materials Research**, v. 1, n. 1, p. 3–15, 23 out. 2020.

STIRLING, D. R.; SWAIN-BOWDEN, M. J.; LUCAS, A. M.; CARPENTER, A. E.; CIMINI, B. A.; GOODMAN, A. CellProfiler 4: improvements in speed, utility and usability. **BMC Bioinformatics**, v. 22, n. 1, 1 dez. 2021.

STOUMPOS, C. C.; MALLIAKAS, C. D.; KANATZIDIS, M. G. Semiconducting tin and lead iodide perovskites with organic cations: Phase transitions, high mobilities, and near-infrared photoluminescent properties. **Inorganic Chemistry**, v. 52, n. 15, p. 9019–9038, 5 ago. 2013.

SUN, S.; FANG, Y.; KIESLICH, G.; WHITE, T. J.; CHEETHAM, A. K. Mechanical properties of organic-inorganic halide perovskites, $CH_3NH_3PbX_3$ (X = I, Br and Cl), by nanoindentation. **Journal of Materials Chemistry A**, v. 3, n. 36, p. 18450–18455, 5 ago. 2015.

SVANE, K. L.; FORSE, A. C.; GREY, C. P.; KIESLICH, G.; CHEETHAM, A. K.; WALSH, A.; BUTLER, K. T. How Strong Is the Hydrogen Bond in Hybrid Perovskites? **Journal of Physical Chemistry Letters**, v. 8, n. 24, p. 6154–6159, 21 dez. 2017.

SVITLYK, V.; CHERNYSHOV, D.; BOSAK, A.; POMJAKUSHINA, E.; KRZTON-MAZIOPA, A.; CONDER, K.; POMJAKUSHIN, V.; DMITRIEV, V.; GARBARINO, G.; MEZOUAR, M. Compressibility and pressure-induced disorder in superconducting phase-separated $Cs_{0.72}Fe_{1.57}Se_2$. **Physical Review B**, v. 89, n. 144106, p. 1–7, 14 abr. 2014.

TANG, X.; CHEN, M.; JIANG, L.; LI, M.; TANG, G.; LIU, H. Improvements in Efficiency and Stability of Perovskite Solar Cells Using a Cesium Chloride Additive. **ACS Applied Materials & Interfaces**, v. 14, n. 23, p. 26866–26872, 15 jun. 2022.

TIAN, W. *et al.* Electronic phase separation and magnetic-field-induced phenomena in molecular multiferroic $(ND_4)_2FeCl_5 \cdot D_2O$. **Physical Review B**, v. 98, n. 5, p. 054407, 8 ago. 2018.

TOLÉDANO, J.-C.; TOLÉDANO, P. Order parameter symmetries and free-energy expansions for purely ferroelastic transitions. **Physical Review B**, v. 21, n. 3, p. 1139–1172, fev. 1980.

TRZEBIATOWSKA, M.; MACZKA, M.; PTAK, M.; GIRIUNAS, L.; BALCIUNAS, S.; SIMENAS, M.; KLOSE, D.; BANYS, J. Spectroscopic Study of Structural Phase Transition and Dynamic Effects in a $[(CH_3)_2NH_2][Cd(N_3)_3]$ Hybrid Perovskite Framework. **Journal of Physical Chemistry C**, v. 123, n. 18, p. 11840–11849, 9 maio 2019.

TU, Q.; KIM, D.; SHYIKH, M.; KANATZIDIS, M. G. Mechanics-coupled stability of metal-halide perovskites. **Matter**, v. 4, n. 9, p. 2765–2809, 1 set. 2021.

TU, Q.; SPANOPOULOS, I.; HAO, S.; WOLVERTON, C.; KANATZIDIS, M. G.; SHEKHAWAT, G. S.; DRAVID, V. P. Out-of-Plane Mechanical Properties of 2D Hybrid Organic–Inorganic Perovskites by Nanoindentation. **ACS Applied Materials & Interfaces**, v. 10, n. 26, p. 22167–22173, 5 jul. 2018.

UEDA, H.; SKOROPATA, E.; BURIAN, M.; UKLEEV, V.; PERREN, G. S.; LEROY, L.; ZACCARO, J.; STAUB, U. Conical spin order with chiral quadrupole helix in $CsCuCl_3$. **Physical Review B**, v. 105, n. 14, 1 abr. 2022.

UNRUH, H. G. Soft modes at ferroelastic phase transitions. **Phase Transitions**, v. 55, n. 1–4, p. 155–168, 19 dez. 1995.

WANG, K. F.; LIU, J. M.; REN, Z. F. Multiferroicity: The coupling between magnetic and polarization orders. **Advances in Physics**, v. 58, n. 4, p. 321–448, jul. 2009.

WANG, S.; XIAO, W. B.; WANG, F. Structural, electronic, and optical properties of cubic formamidinium lead iodide perovskite: a first-principles investigation. **RSC Advances**, v. 10, n. 54, p. 32364–32369, 1 set. 2020.

WANG, Y.; LIU, X.; ZHANG, T.; WANG, X.; KAN, M.; SHI, J.; ZHAO, Y. The Role of Dimethylammonium Iodide in $CsPbI_3$ Perovskite Fabrication: Additive or Dopant? **Angewandte Chemie**, v. 131, n. 46, p. 16844–16849, 11 nov. 2019.

WANG, Y.; TANG, Z.; LIU, C.; JIANG, J.; LIU, W.; ZHANG, B.; GAO, K.; CAI, H. L.; WU, X. Room temperature ferroelectricity and blue photoluminescence in zero dimensional organic lead iodine perovskites. **Journal of Materials Chemistry C**, v. 9, n. 1, p. 223–227, 7 jan. 2021.

WHALLEY, L. D.; GERWEN, P. VAN; FROST, J. M.; KIM, S.; HOOD, S. N.; WALSH, A. Giant Huang-Rhys Factor for Electron Capture by the Iodine Intersitial in Perovskite Solar Cells. **Journal of the American Chemical Society**, v. 143, n. 24, p. 9123–9128, 23 jun. 2021.

WIM J. A. MASSKANT. On Helices Resulting from a Cooperative Jahn-Teller Effect in Hexagonal Perovskites. *Em*: **Structure and Bonding**. [s.l: s.n.]. v. 83p. 55–87.

WOJDYR, M. Fityk: A general-purpose peak fitting program. **Journal of Applied Crystallography**, v. 43, n. 5 PART 1, p. 1126–1128, 2010.

WU, R.; BAI, Z.; JIANG, J.; YAO, H.; QIN, S. Research on the photoluminescence properties of Cu^{2+}-doped perovskite $CsPbCl_3$ quantum dots. **RSC Advances**, v. 11, n. 15, p. 8430–8436, 12 jan. 2021.

XIAO, Z.; SONG, Z.; YAN, Y. From Lead Halide Perovskites to Lead-Free Metal Halide Perovskites and Perovskite Derivatives. **Advanced Materials**, v. 31, n. 47, p. 1803792, 24 nov. 2019.

XU, F.; ZHANG, T.; LI, G.; ZHAO, Y. Mixed cation hybrid lead halide perovskites with enhanced performance and stability. **Journal of Materials Chemistry A**, v. 5, n. 23, p. 11450–11461, 2017.

XU, H.; ZHANG, Z.; DONG, X.; HUANG, L.; ZENG, H.; LIN, Z.; ZOU, G. Corrugated 1D Hybrid Metal Halide $[C_6H_7ClN]CdCl_3$ Exhibiting Broadband White-Light Emission. **Inorganic Chemistry**, v. 61, n. 11, p. 4752–4759, 21 mar. 2022.

XU, Q.; HUANG, J.; LIU, J.; WANG, J.; ZHOU, S.; WANG, X.; NIE, J.; GUO, Y.; OUYANG, X. Lead halide perovskite quantum dots based liquid scintillator for x-ray detection. **Nanotechnology**, v. 32, n. 20, 14 maio 2021.

XUE, Q.; XIA, R.; BRABEC, C. J.; YIP, H. L. Recent advances in semi-transparent polymer and perovskite solar cells for power generating window applications. **Energy and Environmental Science**, v. 11, p. 1688-1709, 1 jul. 2018.

YAKUNIN, S.; PROTESESCU, L.; KRIEG, F.; BODNARCHUK, M. I.; NEDELCU, G.; HUMER, M.; LUCA, G. DE; FIEBIG, M.; HEISS, W.; KOVALENKO, M. V. Low-threshold amplified spontaneous emission and lasing from colloidal nanocrystals of caesium lead halide perovskites. **Nature Communications**, v. 6, 20 ago. 2015.

YAMAMOTO, D.; SAKURAI, T.; OKUTO, R.; OKUBO, S.; OHTA, H.; TANAKA, H.; UWATOKO, Y. Continuous control of classical-quantum crossover by external high pressure in the coupled chain compound $CsCuCl_3$. **Nature Communications**, v. 12, n. 1, 1 dez. 2021.

YAN, J.; LI, H.; ALDAMASY, M. H.; FRASCA, C.; ABATE, A.; ZHAO, K.; HU, Y. Advances in the Synthesis of Halide Perovskite Single Crystals for Optoelectronic Applications. **Chemistry of Materials**, 24 mar. 2023.

YAO, Z.; ZHAO, W.; LIU, S. (FRANK). Stability of the $CsPbI_3$ perovskite: from fundamentals to improvements. **Journal of Materials Chemistry A**, v. 9, n. 18, p. 11124–11144, 14 maio 2021.

YASHIMA, M.; ALI, R. Structural phase transition and octahedral tilting in the calcium titanate perovskite $CaTiO_3$. **Solid State Ionics**, v. 180, n. 2–3, p. 120–126, 9 mar. 2009.

YUAN, W.; ZENG, Y.; TAN, Y. Y.; ZHOU, J. H.; XU, W. J.; ZHANG, W. X.; CHEN, X. M. A new ferroelastic hybrid material with a large spontaneous strain: $(Me_3NOH)_2[ZnCl_4]$. **Chemical Communications**, v. 55, n. 61, p. 8983–8986, 2019.

ZHANG, B. H.; HOU, Y. S.; WANG, Z.; WU, R. Q. First-principles studies of spin-phonon coupling in monolayer $Cr_2Ge_2Te_6$. **Physical Review B**, v. 100, n. 22, 30 dez. 2019.

ZHANG, H.; HU, C.; HU, Z.; MAO, J.; SONG, Y.; XIONG, R. Narrow Band Gap Observed in a Molecular Ferroelastic: Ferrocenium Tetrachloroferrate. 2020.

ZHANG, X.; ZHOU, B.; CHEN, X.; YU, W. W. Reversible Transformation between $Cs_3Cu_2I_5$ and $CsCu_2I_3$ Perovskite Derivatives and Its Anticounterfeiting Application. **Inorganic Chemistry**, v. 61, n. 1, p. 399–405, 10 jan. 2022.

ZHANG, Y.; LIU, X.; SUN, H.; ZHANG, J.; GAO, X.; YANG, C.; LI, Q.; JIANG, H.; WANG, J.; XU, D. Strong Self-Trapped Exciton Emissions in Two-Dimensional Na-In Halide Perovskites Triggered by Antimony Doping. **Angewandte Chemie - International Edition**, v. 60, n. 14, p. 7587–7592, 29 mar. 2021.

ZHENG, Y.; YUAN, X.; YANG, J.; LI, Q.; YANG, X.; FAN, Y.; LI, H.; LIU, H.; ZHAO, J. Cu doping-enhanced emission efficiency of Mn^{2+} in cesium lead halide perovskite nanocrystals for efficient white light-emitting diodes. **Journal of Luminescence**, v. 227, 1 nov. 2020.

ZHOU, C.; LIN, H.; HE, Q.; XU, L.; WORKU, M.; CHAABAN, M.; LEE, S.; SHI, X.; DU, M.-H.; MA, B. Low dimensional metal halide perovskites and hybrids. **Materials Science and Engineering: R: Reports**, v. 137, p. 38–65, 1 jul. 2019.

ZHOU, Y.; CHEN, J.; BAKR, O. M.; SUN, H. T. Metal-Doped Lead Halide Perovskites: Synthesis, Properties, and Optoelectronic Applications. **Chemistry of Materials**, v. 30, n. 19, p. 6589–6613, 9 out. 2018.

ZHU, P.; ZHU, H.; ADHIKARI, G. C.; THAPA, S. Spectral optimization of white light from hybrid metal halide perovskites. **OSA Continuum**, v. 2, n. 6, p. 1880, 15 jun. 2019.

ZHU, P.; ZHU, J. Low-dimensional metal halide perovskites and related optoelectronic applications. **InfoMat**, v. 2, n. 2, p. 341–378, 6 mar. 2020.

APENDIX A – PUBLICATIONS AND CONFERENCE CONTRIBUTIONS

Publications:

- **J. S. Rodríguez-Hernández**, M. A. Mayra, D. S. Abreu, A. Nonato, R. X. da Silva, A. García-Fernández, M. A. Señarís-Rodríguez, M. Sánchez-Andújar, A. P. Ayala, and C. W. A. Paschoal, Uniaxial Negative Thermal Expansion in the $[(CH_3)_2NH_2]PbBr_3$ Hybrid Perovskite, J. Mater Chem C Mater 10, 17567 (**2022**). (DOI: 10.1039/D2TC02708A)

Conference Contributions:

- ***VI Encontro Brasileiro de Espectroscopia Raman (EnBraER) –*** *Panel Presentation Section* **–** Raman Spectroscopy Investigations on $Cs_2FeCl_5.H_2O$ Single-Cyrstals (2019).
- ***VI Encontro Brasileiro de Espectroscopia Raman (EnBraER) –*** *Oral Presentation* **–** Temperature-Induced structural phase transition in $DMAPbBr_3$ metal-halide perovskite (2019) (**Premio Melhor Apresentação e Trabalho do Congresso**)
- ***Escola Ricardo Rodrigues de Luz Síncrotron (ER2LS) –*** *Panel Presentation Section* **–** Synchrotron X-Ray Diffraction and Raman Spectroscopy Characterization of the Structural Phase Transition of $[(CH_3)_2NH_2]PbBr_3$ Hybrid Perovskite (2021).
- ***32nd LNLS Annual Users Meeting (RAU) –*** *Postel Presentation Section* **–** Pressure-induced structural phase transition of $CsCuCl_3$ like-perovskite compound (2022).
- ***XXXVI Encontro de Física do Norte e Nordeste (EFNNE) –*** *Oral Presentation Section* **–** Pressure-induced structural phase transition of $CsCuCl_3$ like-perovskite compound (2022).
- ***VII Encontro Brasileiro de Espectroscopia Raman (EnBraER) –*** *Panel Presentation Section Section* **–** Pressure-induced structural phase transition of $CsCuCl_3$ like-perovskite compound (2022).
- ***VII Encontro Brasileiro de Espectroscopia Raman (EnBraER)*** *– Panel Presentation Section Section* – The electron-phonon coupling to produce photoluminescence excitonic states in the 2D $CsPb_2Br_5$ related-perovskite (2022).